The role of waves in the autumn Arctic Ocean

Madison Smith

A dissertation
submitted in partial fulfillment of the
requirements for the degree of

Doctor of Philosophy

University of Washington

2019

Reading Committee:

Jim Thomson, Chair

Nirnimesh Kumar

Sharon Stammerjohn

Program Authorized to Offer Degree:
Civil & Environmental Engineering

University of Washington

Abstract

The role of waves in the autumn Arctic Ocean

Madison Smith

Chair of the Supervisory Committee:
Associate Professor Jim Thomson
Civil & Environmental Engineering

Recent decline of sea ice coverage in the Arctic Ocean has resulted in a substantial seasonal wave climate. Waves generated in the open water are attenuated far into the sea ice, but are a defining feature of the marginal ice zone (MIZ). In autumn, waves in the MIZ can be large due to the significant open water area following the minimum ice extent. Waves are expected to affect ice cover development through both kinematic and thermodynamic processes. In this research, I use observations from 2015 in the Beaufort Sea region to improve understanding of key feedbacks between waves and sea ice, and describe implications for autumn ice formation.

In the MIZ, where surface waves are often present, much of the ice forms through the 'pancake cycle'. Gradients in wave orbital velocities across the surface cause small ice crystals to be herded into increasingly larger, rounded floes. Modeling the relative motion between ice floes is the basis for describing pancake ice growth, as well as the attenuation of wave energy associated with their motion. Here, existing models for ice motion and growth are evaluated using coincident measurements of waves and pancake sea ice made using shipboard stereo video. The observations are well captured by existing models, and relative velocities of floes are typically small compared to the mean orbital velocities. The models for relative motion of pancake sea ice due to waves can be subsequently used to estimate attenuation of wave energy due to floe motion. Under the conditions observed, estimates of wave energy loss from ice-ocean turbulence are much larger than those from pancake collisions, and can

account for most of the observed wave attenuation.

In addition to the general trends of sea ice growth in the Arctic in autumn, ice edge advance can be temporarily reversed as a result of upper ocean mixing by wind and waves. Observations during a high wind and wave event demonstrate how heat released from the upper ocean can melt significant amounts of newly formed pancake sea ice. Measurements from drifting buoys and ship-based platforms are used to construct heat and salt budgets, which give a consistent picture of the air-ice-ocean evolution. Following the event, there was less heat remaining in the upper ocean and sea ice formation quickly resumed.

The young ice cover formed throughout the autumn significantly changes the way in which momentum is transferred from the wind to the waves, and into the ocean below. Using coincident measurements of sea ice, wind, surface waves, and near-surface turbulence across a range of conditions, I quantify the relationship between new sea ice formation, attenuation of waves, and suppression of near-surface turbulence. Sea ice formation reduces the wind input transfer velocity by attenuating the short waves, which simultaneously suppresses the wave-driven near-surface turbulence. As ice thickens and grows, the ice provides the dominant roughness for wind input. Based on the observations, I suggest parameters for estimating near-surface turbulence in thin pancake and frazil ice, which are ubiquitous in autumn marginal ice zones.

The results of this research provide validation and parameterization for a new class of sea ice models that include dynamic and thermodynamic floe processes. Constraining rates of pancake ice growth is important as it occurs at a much faster rate than simple thermodynamic ice growth, and it is believed to be more common in the Arctic Ocean in recent years. Yet, as the timing of the ice-edge advance shifts later into stormier autumn months, waves from storm events may play an increasing role in delaying ice advance. Thus, the coupled wave-ice interactions examined are likely to become increasingly important in determining the state of the autumn Arctic Ocean with the growing wave climate.

TABLE OF CONTENTS

LIST OF FIGURES

LIST OF TABLES

ACKNOWLEDGMENTS

First and foremost, I am incredibly grateful to my advisor, Jim Thomson, for his mentorship and unwavering support. I can't imagine having worked anyone else. He teaches by example in how to be a great scientist - enthusiastic, hard-working, and always willing to learn new things. He is proof that you do not have to choose between being kind and successful. Thank you for putting your trust, your time, and your patience into me.

The Environmental Fluid Mechanics group was my family at UW. Thank you for all the feedback and friendship over the years, and for making every Thursday a highlight of my week. I am especially grateful to Roxanne, Maricarmen, Seth, Mike, and Sam for being the best office-mates, travel-buddies, and friends I could have hoped to find.

Thank you to my committee members (past and present) - Nirnimesh Kumar, Sharon Stammerjohn, Eric D'Asaro, CC Bitz, and Jodi Young - for thoughtful feedback and encouragement throughout my degree. I would also like to thank my co-authors for their collaboration and keen insight.

I would like to acknowledge the Office of Naval Research for providing funding for this research, and I am grateful to the entire 'Sea State' group for giving me incredible support. The Valle Scholarship funded my first year at the University of Washington. The PIPERS program was supported by the National Science Foundation. Field observations were made possible by the tireless dedication of Alex de Klerk and Joe Talbert, as well as the crews of the R/V *Sikuliaq* and R/V *Palmer*. I owe much to Britt Raubenheimer and Steve Elgar for advising me as a Summer Student Fellow at WHOI. It was as a result of their mentorship that I had the opportunity to fall in love with research and decided to pursue a PhD. Thank you also to the Bowdoin EOS community for igniting my passion for earth science.

I am grateful to the wide and wonderful community of scientists that has welcomed me, and I feel I have become a part of over the past 5 years. Particularly, to all of those who I spent countless hours with while at sea - especially Lettie Roach, Jeffrey Mei, and Alison Kohout. I appreciate your friendship, and look forward to many more years of collaboration.

My deepest gratitude goes to my family (natural and chosen), who have been my greatest supporters - my parents; my partner, Ryan; my sister, Bryn; Louise. Thank you for supporting me, without hesitation, in everything I choose to do. Ryan, I am especially grateful for your daily encouragement, your graciousness in making my dreams a priority, and your love. I eagerly look forward to the new adventures in our future.

Chapter 1

INTRODUCTION

1.1 Motivation

Sea ice forms from frozen seawater in the cold, polar oceans. At its maximum extent, it can cover as much as 10% of the earths ocean. Although the remote locations where sea ice forms means that most people will never encounter it, sea ice affects our daily lives through its role in the earth's climate. The high albedo of sea ice cover on the ocean results in the reflection of much of the incoming solar energy. This property leads to the albedo feedback, in which high albedo helps to maintain cold polar temperatures and allows seasonal sea ice to persist. The global temperature gradient maintained by this feedback is key to ocean circulation and global weather patterns. Additionally, the drift of sea ice feeds ocean overturning cells by transporting freshwater from polar ice-covered oceans to lower latitudes [*Pellichero et al.*, 2018]. For those species who inhabit the Arctic, sea ice plays many fundamental roles from serving as critical habitat, to buffering and protecting the coast on which communities are built.

As sea ice forms at the thin interface between the atmosphere and ocean, it is constantly evolving in response to forcings from the atmosphere above and the ocean below. As the world's air and ocean temperatures increase, the Arctic has been losing sea ice - the extent at the end of summer is about half what it was 30 years ago. This decline means there is less 'protection' for the Arctic Ocean from solar inputs, and has direct and indirect effects on the northern hemisphere and globe [*Vihma*, 2014; *Moon et al.*, 2019]. The resulting Arctic amplification may accelerate Greenland ice sheet loss due to increased heat transfer from the ocean [*Stroeve et al.*, 2017]. Additionally, the loss of coastal sea ice has resulted in accelerated erosion of Arctic coasts and built environments [*Overeem et al.*, 2011]. Overall, the loss of Arctic ice is expected to have substantial implications for and costs to society [*Euskirchen et al.*, 2013].

As a result, there has been significant scientific and media focus recently on the declining trend in minimum annual sea ice coverage (red line in Fig. 1.1), which occurs in September. However, the extent of sea ice throughout the entire seasonal cycle has been on the decline.

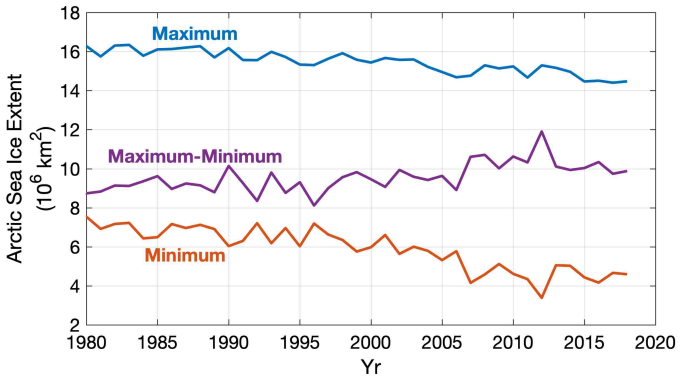

Figure 1.1: Sea ice extent in the Arctic Ocean since 1980. Blue and red lines show extent at maximum and minimum respectively, and purple line is the difference between the two (also known as the seasonal ice cover). Data courtesy of the National Snow and Ice Data Center (nsidc.org/arcticseaicenews/charctic-interactive- sea-ice-graph/).

The maximum extent of Arctic sea ice typically occurs in March, and has decreased nearly 2 million square kilometers since 1980. This decline is less extreme than that of the summer minimum, resulting in a statistically significant increase in the difference between the two (purple line in Fig. 1.1; $0.37 \pm 0.08 \times 10^6$ km^2/decade). The difference between the annual minimum and maximum represents the portion of the sea ice that forms in the autumn and winter and melts in the spring each year, and is referred to as the Seasonal Ice Zone (SIZ). The factors controlling autumn ice growth are an important part of understanding the full seasonal cycle.

A consequence of the dramatic reduction in ice coverage at the beginning of autumn is that there is greater area for production of waves. Waves in open water are often limited by the distance of open water from land, referred to as the fetch. The dependence of wave energy on fetch has been empirically described as a logarithmic fit between the nondimensional parameters [*Young*, 1999]: nondimensional energy and fetch are defined as $\mathcal{E} = \frac{g^2 H_s^2}{16U^4}$ and $\mathcal{X} = \frac{gx}{U^2}$, respectively, where H_s is significant wave height, g is gravitational acceleration, U is

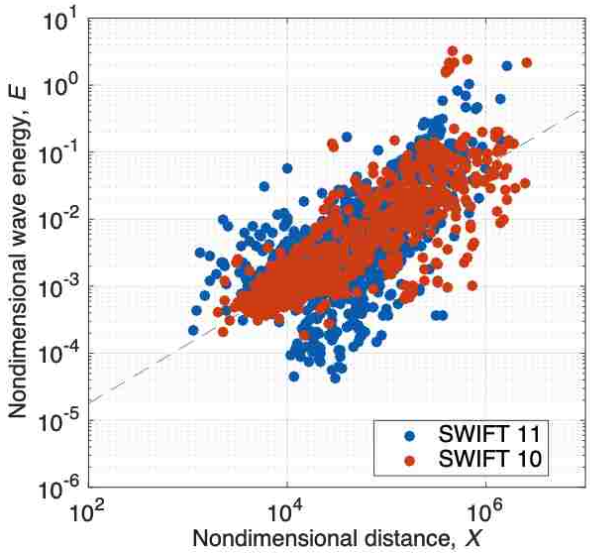

Figure 1.2: Nondimensional fetch versus nondimensional wave energy in the Beaufort Sea, estimated for two different platforms. [Reproduced from *Smith and Thomson*, 2016].

wind speed and x is dimensional fetch distance. While the near-complete ice coverage of the Arctic basin historically prevented substantial wave growth, ice edge retreat increases the typical distance between land and ice pack. *Thomson and Rogers* [2014a] used a combination of in situ observations and a numerical wave model to show that the traditional definition for fetch can be altered to include the distance from the sea ice edge. Empirical open water fetch relationships hold for observations in the Beaufort Sea region. However, these simple nondimensional fetch scalings did not work under all wind conditions and did not hold in areas with local ice cover.

Additional observations of waves throughout open water and the marginal ice zone of the Beaufort Sea in 2014 were used to further explore controls on wave growth in *Smith and Thomson* [2016]. (Further details on this work can be found in the author's master's thesis: *Smith* [2016].) The approach from *Thomson and Rogers* [2014b] was applied to all observations in open water by defining the fetch as the distance from ice and land. Although

the waves observed in 2014 generally appear to follow classic fetch scalings (Fig. 1.2), only 26% were purely fetch-limited. The rest were limited by the duration that the wind has been blowing. Such duration limitation on wave growth is common throughout open oceans, as fetch increases. The transition towards waves limited primarily by wind duration, rather than fetch, is likely indicative of more total wave energy. The resulting swell is less limited by ice extent and carries more energy into the ice cover. Although these observations are specific to the Beaufort Sea region, model hindcasts suggest that the fraction of swell to wind sea is increasing in nearly all basins of the Arctic Ocean [*Li et al.*, 2019a].

While we treat the ice similar to land for the purpose of predicting wave energy in open water, in reality, wind in the marginal ice zone is capable of generating short, fetch limited waves in the open water distance between distinct pieces of ice, known as floes [*Smith and Thomson*, 2016]. The distance between floes acts as a 'effective fetch' which is a function of the fractional ice cover (Fig. 1.3). The resulting exponential relationship for ice cover and fetch can be used to cumulatively estimate wave evolution over a range of ice covers [*Gemmrich et al.*, 2018].

With increasing open water area in the emerging Arctic Ocean, waves are likely to have a larger role to play. Average wave energy is increasing across all basins, both outside and in the ice [*Li et al.*, 2019a]. The growth of waves outside and within the marginal ice zone is expected to have a variety of implications for the air-sea-ice system. This thesis will use observations from autumn to address the question: what are the effects of storms and waves when the ice begins to regrow and advance southward? The aim of this work is to provide descriptions and parameterizations of key processes that may play an increasing role as the Arctic Ocean continues to evolve.

The remainder of this chapter will introduce the basic ocean and sea ice properties that provide the foundation for the subsequent chapters, then give an overview of field observations and outline the remaining chapters. The processes that will be described therein are shown schematically in Fig. 1.4.

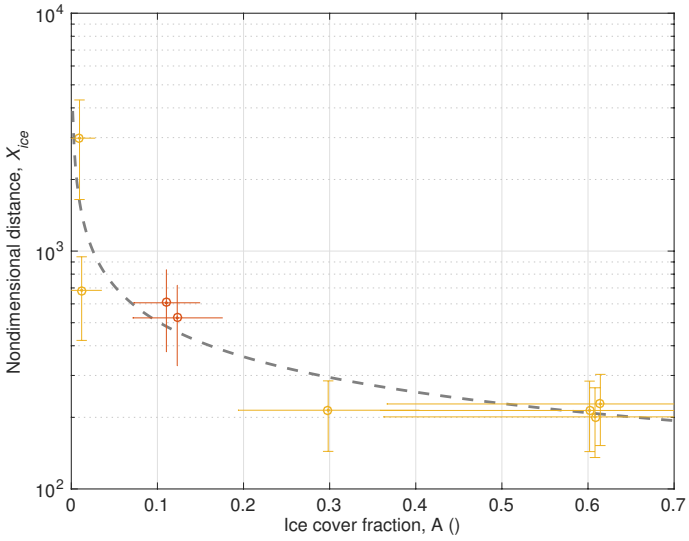

Figure 1.3: Exponential relationship of local fraction ice cover and nondimensional effective fetch distance, $\mathcal{X}_{ice}$. [Reproduced from *Smith and Thomson*, 2016].

1.2 Background

1.2.1 Ocean wave basics

Ocean surface waves are a form of gravity waves generated by wind stress. Linear wave theory describes waves as simple, sinusoidal fluctuations, which can be described by the height, length, and frequency. The height is the distance from trough to crest, and the length is simply the distance between each crest or trough. The wave frequency is the inverse of the wave period, which is the time that it takes for a complete wave cycle to pass a point.

In reality, the ocean wave field is composed of irregular waves with a variety of heights, directions, and frequencies. Using Fourier analysis, wave fields can be decomposed into a combination of linear waves of different frequencies. The result is summarized in a wave spectrum, which gives the energy (proportional to the wave height squared) at each frequency.

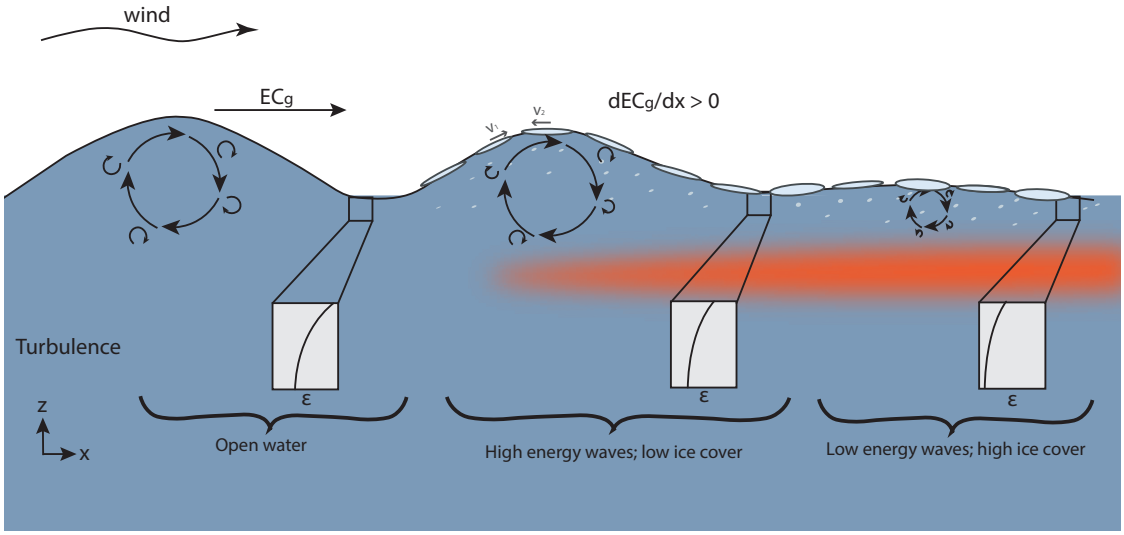

Figure 1.4: Schematic showing how the propagation of wave energy flux (EC_g) into sea ice drives a number of small-scale processes. Relative velocities of ice floes due to waves result in collisions and formation of pancake sea ice. Waves enhance the mixing from wind over the upper ocean, increasing the potential to entrain warm sub-surface water.

It is most common to use the 1D wave spectrum, which gives the scalar wave energy at each frequency, $E(f)$. A 2D wave spectrum is necessary to represent the directionality of the wave field, $E(f, \theta)$.

Bulk parameters calculated from wave spectra are useful for describing the characteristic waves in a wave field. The significant wave height describes the characteristic height as:

$$H_s = 4\sqrt{\int E(f)df} \tag{1.1}$$

or four times the area under the wave spectrum. The characteristic frequency is typically either defined as the frequency at the peak of the spectrum f_p, or as an energy weighted frequency

$$f_e = \frac{\int fE(f)df}{\int E(f)df} \tag{1.2}$$

The peak and energy weighted periods (T_p, T_e) are the inverses of these, respectively.

An important property of ocean waves is that they exhibit frequency dispersion (often referred to simply as dispersion), in which waves of different wavelengths travel at different speeds. Longer waves travel faster than short waves, which explains why the swell are often the first waves to arrive from a storm. The dispersion relation connects the wave period and wavelength (L)

$$L = \frac{g}{2\pi}T^2 \tanh\left(2\pi\frac{h}{L}\right) \tag{1.3}$$

where h is the water depth. A result of this relationship is the phase speed or velocity (c_p), which is a function of the wave period in deep water

$$c_p = gT/(2\pi) \tag{1.4}$$

Returning to the idealized picture of a linear wave as a sinusoidal motion, we can imagine that a fluid parcel at the surface moves back and forth with each wave following the wave orbits. The orbital motion is in the direction of wave propagation at the crest of the wave, and opposite to the direction of propagation in the trough. The particle trajectories make approximately a round path in deep water, and the diameter of this path decreases with distance below the surface.

In reality, the trajectories associated with orbital velocities are not perfectly circular, as the forward velocities are slightly larger. A water particle near the surface moves slightly forwards with the passage of each wave. This results in a net velocity in the direction of wave propagation, known as the Stokes drift. As with the orbital velocity, the magnitude of the Stokes drift decays with depth below the surface.

1.2.2 Sea ice formation basics

Formation of new sea ice typically begins in the autumn in the Arctic, and continues throughout the winter. After the top few meters of the ocean have been cooled to the freezing point, sea ice begins growing [*Weeks and Ackley*, 1986]. In quiescent conditions, the ice forms as a thin crust at the surface called nilas (Fig. 1.5e), and thickens through the subsequent freezing of water molecules at the interface of ice and water, called congelation. In contrast, sea ice formation in turbulent water begins with individual ice crystals called frazil (Fig. 1.5a). Accumulation of ice crystals near the ocean surface forms a layer of grease ice (Fig. 1.5b), which may form into pancake sea ice (Fig. 1.5c) if surface waves are present.

While there has been a large amount of research focused on understanding ice growth beginning in quiescent conditions [i.e. *Anderson*, 1961; *Maykut*, 1986], there has been relatively little work to understand grease and pancake ice formation in the presence of surface waves. Grease ice forms when the surface turbulence is insufficient to keep frazil crystals suspended. The subsequent rate of thickening has been found to be directly proportional to the fraction of open water, which allows for rapid heat flux from the ocean to the air [*Naumann et al.*, 2012]. Generally, the grease ice layer will be thicker under higher wind speeds [*Winsor and Björk*, 2000]. Recent modeling has shown that the net sea ice growth is much higher under turbulent conditions, when frazil forms rather than nilas [*Matsumura and Ohshima*, 2015].

Pancake sea ice floes begin to form from grease ice when the fraction of solid ice is sufficiently high (about 30%) [*Maus and De La Rosa*, 2012]. Pancakes are rounded discs, typically with slightly upturned edges as a result of wave motion and collisions between the pancakes. Using observations of pancakes from the Weddell Sea in 2000, *Doble et al.* [2003]

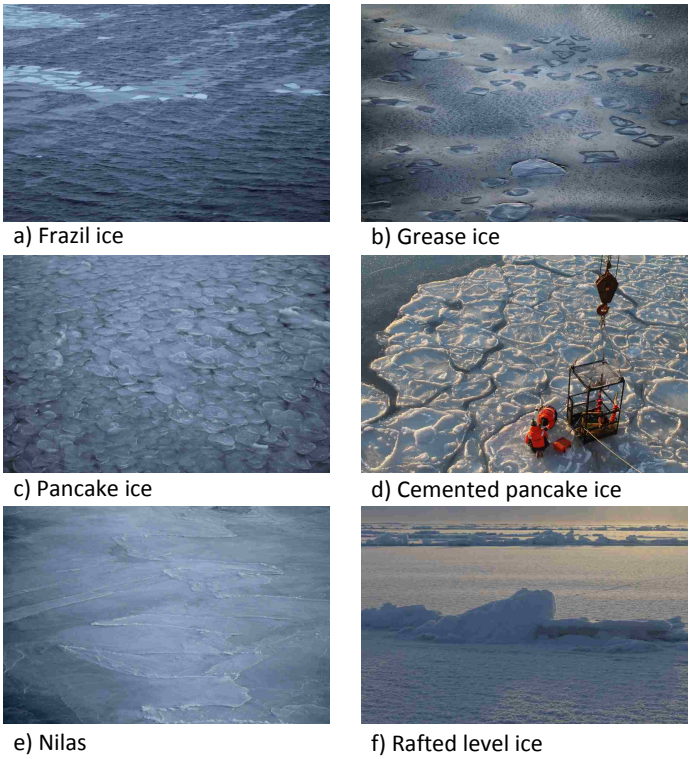

Figure 1.5: Photos of the sea ice types commonly observed throughout autumn ice formation.

found that most of their thickening occurs by deposition of frazil on top. Although the congelation growth at the bottom of the pancakes was similar to that under calm conditions, thickening by growth on the top results in 2-3 times faster growth rates [*Doble*, 2009]. As waves are further damped and heat loss continues, pancakes begin to weld to their neighbors (Fig. 1.5d) and further thicken through the congelation process.

Throughout the winter, ice pack that has formed from either nilas or cemented pancake floes continues to thicken. Ice that has grown through one winter season is called first-year ice. When this growth has begun as pancakes under wind and wave forcing, there will be a thicker layer of randomly oriented crystals, while ice that has growth from nilas will be primarily congelation or columnar.

1.2.3 Waves in sea ice

The effect of sea ice cover on a wave field can be clearly seen from ships and in imagery; sea ice damps wave energy such that the wave field is often noticeably less choppy inside the ice edge. Early field observations of waves in sea ice showed that decay was not constant across all frequencies, and that ice preferentially attenuates higher frequencies [*Wadhams et al.*, 1988]. These observations also suggested a roll-over in attenuation at the higher frequencies, but it has since been suggested that this is likely a result of wind input [*Li et al.*, 2017]. Additionally, wave attenuation rates are exponential with distance from the ice edge. As a result, long swell waves have been observed to penetrate hundreds of kilometers into the sea ice during storm conditions [*Kohout et al.*, 2014]. The change in wave energy with distance can be expressed as

$$E(f,x) = E(f,0)e^{-\alpha x} \tag{1.5}$$

where α is the frequency-dependent attenuation coefficient, and $E(f,0)$ and $E(f,x)$ are the wave energy incident and observed some distance x into the ice, respectively [e.g., *Wadhams*, 1975].

The two dominant mechanisms leading to wave attenuation are scattering and dissipative processes. Scattering is a conservative process, but reduces wave energy in the sea ice by redistributing incoming energy in all directions. Dissipative processes include turbulence due to friction, viscosity, inelastic floe-floe collisions, and floe flexure and breakup. The relative importance of scattering and dissipation is still an active area of research; dissipative processes are thought to dominate for most of the MIZ.

The basic approach for considering the attenuation of waves in ice in global wave models such as WaveWatch III (WW3) is to include an additional term in the radiative transfer equation. The radiative transfer (or Boltzmann) equation describes the evolution of wave energy as a balance of source and sink terms

$$\frac{\partial E(f)}{\partial t} + (c_g \cdot \nabla)E(f) = S_{in} - S_{ds} + S_{nl} - S_{ice} \tag{1.6}$$

The terms on the left represent the evolution of wave energy as a function of frequency,

where c_g is the wave group velocity (half of the phase velocity c_p in deep water). The source terms are on the right-hand side, where S_{in} is the wind input, S_{ds} is the dissipation of wave energy, and S_{nl} is the non-linear transfer between wave frequencies. Dissipation of wave energy typically occurs through wave breaking and generation of turbulence. The final term, S_{ice}, represents the damping of wave energy due to sea ice.

Approaches to modeling S_{ice} can be divided into conservative redistribution due to scattering, and non-conservative attenuation by dissipation. Scattering models are strongly dependent on the floe size distribution, as each floe contributes to isotropic redistribution of some of the wave energy. Dissipative attenuation has been quantified primarily in viscous and viscoelastic models. In viscous models, the entire sea ice layer is represented as a homogenous viscous medium, with a viscous parameter based on sea ice characteristics such as floe size and concentration. Inclusion of elasticity is necessary to describe possible changes in the dispersion relation in sea ice [*Shen*, 2019]. Although the mechanisms parameterized are different, both scattering and dissipation can result in a similar observed attenuation. It is likely that both are happening simultaneously to some degree throughout the MIZ. All of the current schemes for wave attenuation have been implemented in WW3 [*WaveWatch III Development Group*, 2016; *Rogers et al.*, 2018], allowing the user to decide which mechanisms they would like to consider.

1.2.4 Atmosphere-ice-ocean interactions

The wave-ice interactions described in the previous sections are part of the larger coupled atmosphere-ice-ocean system in which energy and momentum are exchanged. The wind transfers momentum from the atmosphere to the underlying ocean depending on the roughness of the surface. The atmosphere drives the flux of energy into or out of the ocean as a result of radiative, sensible, and latent heat fluxes. The presence of sea ice modifies both of these. Sea ice alters the transfer of momentum from the atmosphere to the ocean by reducing the surface roughness, which is often expressed using a drag coefficient (C_d). The drag coefficient is typically around 1.3×10^{-3} in the open ocean [*Smith*, 1988], but is reduced

in small pancake ice cover to $C_d = 0.9 - 1.5 \times 10^{-6}$ [*Guest and Davidson*, 1991]. Additionally, sea ice results in the reflection of up to 90% of incoming solar radiation. The resulting total heat flux between the surface and atmosphere, F_{atm}, is typically negative in the autumn Arctic (from the ocean to the atmosphere), with more heat loss over the ocean than in sea ice-covered areas [*Persson et al.*, 2018a].

The transfer of momentum and energy from the atmosphere to the ocean largely occurs within a shallow surface mixed layer, which has nearly homogenous physical properties. The depth of the mixed layer is a result of the balance between turbulent mixing (which destabilizes stratification) and buoyancy fluxes (which stabilize stratification). Turbulent mixing in the mixed layer is mostly generated by wind stress, but may also be enhanced by waves and convection [*D'Asaro*, 2014]. Buoyancy fluxes are generally a result of heat input or loss from the atmosphere, evaporation, precipitation, or sea ice melt, resulting in a change of the density gradient at the base of the mixed layer.

The mixed layer depth (MLD) is tens to hundreds of meters deep globally, but in the western Arctic is typically only around 8 m in summer and 30 m in winter [*Peralta-Ferriz and Woodgate*, 2015]. The Arctic MLD has been observed to be deepening in recent years. This appears to be more a result of decreases in buoyancy (due to less freshwater input) than increase in wind-driven turbulent mixing [*Peralta-Ferriz and Woodgate*, 2015].

Within the upper few meters of the mixed layer, the energy associated with turbulence (known as turbulent kinetic energy, or TKE) is elevated above values expected by law-of-the-wall scalings as a result of wave breaking (i.e., whitecaps). The production of turbulence from wave breaking at the surface is typically assumed to be in balance with the TKE dissipation rate (ϵ), and has been observed to be many orders of magnitude higher than background levels [*Gemmrich and Farmer*, 2004]. It is approximately in local equilibrium with the wind input [*Thomson et al.*, 2016a], which does work as a function of wind speed and the dynamic roughness elements. In the ocean, short waves are the primary surface roughness, and so the effective transfer velocity is related to phase speed of the waves [*Gemmrich and Farmer*, 2004]. The dissipation rate over the depth of a couple significant wave heights typically scales

as z^{-2} [*Terray et al.*, 1996], and is further elevated within one significant wave height of the surface due to wave energy dissipation of microbreakers [*Sutherland and Melville*, 2015].

In sea ice, it has been suggested that the equilibrium between the wind and waves should be maintained [*Zippel and Thomson*, 2016]. However, the dissipation rate of TKE is lower as a result of the damping of short waves. The reduction in the TKE production and dissipation is then likely a function of the fractional ice cover [*Zippel and Thomson*, 2016].

1.3 The 2015 'Sea State' observational campaign

The observed decline in sea ice extent has increased the interest of the U.S. Navy in understanding and predicting sea ice conditions in the Arctic Ocean. Safe and efficient operation in this region requires accurate forecasting of both the sea state and the sea ice edge and evolution. Motivated to improve predictive skill, the Office of Naval Research has funded a number of large collaborative research programs in recent years. The overarching goals of these programs are to characterize key processes in the Arctic Ocean, develop coupled ice-ocean-wave-atmosphere regional models, and advance technologies to allow for sustained Arctic observational capability. There have been four completed and ongoing Departmental Research Initiatives (DRIs) funded in support of these goals: 'Emerging Dynamics of the Marginal Ice Zone', 'Sea State and Boundary Layer Physics of the Emerging Arctic Ocean', 'Stratified Ocean Dynamics in the Arctic' (SODA), and 'Arctic Mobile Observing System' (AMOS).

The observations for the entirety of this dissertation were completed during the field campaign of 'Sea State and Boundary Layer Physics of the Emerging Arctic Ocean' (hereafter referred to as 'Sea State'), which took place in autumn 2015 in the Beaufort and Chukchi Seas [Fig. 1.6; *Thomson et al.*, 2015]. This program was specifically motivated by the observed increase in wave activity in the Western Arctic with declining sea ice cover [*Thomson et al.*, 2013b]. A primary goal of this program was to improve skill in forecasting sea state in the Arctic Ocean, both in open water and in sea ice. The observational campaign additionally aimed to improve understanding of heat and mass exchange between the ocean and

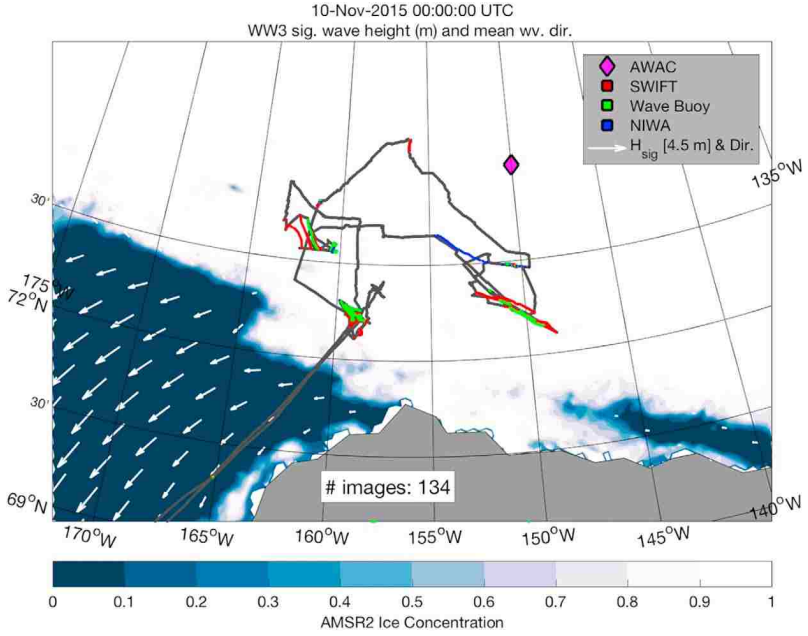

Figure 1.6: Map of cruise track from the Sea State field campaign in Beaufort and Chukchi Seas in the fall of 2015. Colored points show wave buoy deployments during all wave experiments. Shading shows the sea ice coverage and arrows depict wave height and direction at the end of the experiment (November 10). (Reproduced from *Thomson et al.* [2018])

atmosphere during autumn ice advance.

The in situ observations during the 42-day cruise, from late September to early November, were supplemented by remote sensing observations. The cruise was divided into different sampling modules, with the majority dedicated to event-based wave experiments in which large numbers of wave buoys were deployed for periods of hours to days. *Thomson et al.* [2018] describes the other sampling modules and the key findings of the program. In total, there were eight wave experiments spanning a range of wave conditions, with a key finding being the prevalence of pancake sea ice formation in the emerging Arctic Ocean.

1.4 Outline

This dissertation will use observational data from the wave experiments during the 'Sea State' program to improve understanding of the role of waves in autumn ice formation. The processes that are explored are shown schematically in Fig. 1.4, and are organized into chapters as outlined here:

In Chapter 2, stereo video observations are used to measure the relative velocities of pancakes floes, and evaluate existing models for ice motion. The results provide insight into pancake growth rates and rates of wave energy loss, both of which can result from floe-floe collisions. This chapter has been submitted to the *Annals of Glaciology* as:

> Smith, M, and J. Thomson. Submitted. Pancake ice kinematics and dynamics using shipboard stereo video. *Annals of Glaciology.*

Chapter 3 describes an event in which a large amount of ocean heat release melted thin, new sea ice in the Beaufort Sea. Heat and salt budgets for the event are presented, and discussed in the context of heat fluxes from prior observations under thicker ice in the region. The role of waves are explored by comparing the evolution under different wave forcing. This chapter is reproduced, with only minor changes, from:

> Smith, M., S. Stammerjohn, O. Persson, L. Rainville, G. Liu, W. Perrie, R. Robertson, J. Jackson, and J. Thomson. 2018. Episodic Reversal of Autumn Ice Advance Caused by Release of Ocean Heat in the Beaufort Sea. *Journal of Geophysical Research: Ocean*, 123. doi:10.1002/2018JC013764

Chapter 4 aims to parameterize near-surface turbulence in new marginal ice zones. Measurements from SWIFT buoys deployed in pancake and frazil ice cover are used to describe different regimes controlling how energy is transferred into the upper ocean. This chapter has been reproduced from:

Smith, M, and J. Thomson. 2019. Ocean Surface Turbulence in Newly Formed Marginal Ice Zones. *Journal of Geophysical Research: Oceans*, 124. doi:10.1029/2018JC014405

Finally, Chapter 5 summarizes the dissertation and implications, and suggests directions for future research.

Chapter 2

PANCAKE SEA ICE KINEMATICS AND DYNAMICS USING SHIPBOARD STEREO VIDEO

2.1 Introduction

Pancake ice is a type of sea ice that is often found in areas where new ice formation is coincident with large surface waves. This ice type has been commonly observed in the Southern Ocean [*Treshnikov*, 1967; *Lange et al.*, 1989] as well as the Arctic Ocean, but previously observations in the Arctic were limited to areas open to other oceans such as the Okhotsk Sea and Bering Sea. Observations of pancake ice in the Central Arctic basin have become more commonplace with seasonal sea ice retreat in recent years [*Thomson et al.*, 2018]. Pancake ice has also been observed in large bodies of freshwater, including a number of northern lakes and rivers [e.g., *Rumer et al.*, 1979; *Campbell et al.*, 2014].

Conceptually, pancake ice formation and growth can be divided into three sequential stages: the formation of a grease or frazil ice layer, formation and growth of pancake floes, and the formation of composite pancakes by welding together of individual floes [*Shen et al.*, 2001]. Both the growth and welding of pancake floes depend strongly on the presence of dynamic wave motion. The gradient of wave orbital velocities across each wave drive relative motion of floes towards (and away from) each other (Fig. 2.1). This motion can result in the floe-floe collisions that are critical to pancake formation and subsequent growth. *Doble et al.* [2003] and *Doble* [2009] found that growth due to collisions is primarily a result of the 'scavenging' of frazil ice from the water onto the tops of pancake floes. *Doble* [2009] suggested that scavenging occurs because of the reduction in frazil area as floes converge with wave motion.

There has been substantial observational and theoretical progress to understand the transformation of waves propagating into sea ice [*Shen*, 2019]. Although many mechanisms have been proposed and examined to account for the attenuation of wave energy in sea ice, it is still not clear which mechanisms dominate [*Squire*, 2019]. Part of the challenge is that the dynamics are sensitive to ice type. The collisions of sea ice floes are one proposed mechanism that can dissipate wave energy [*Shen and Squire*, 1998]. This may be relatively important in pancake sea ice, where the energy associated with the impact is observed to accelerate the ice

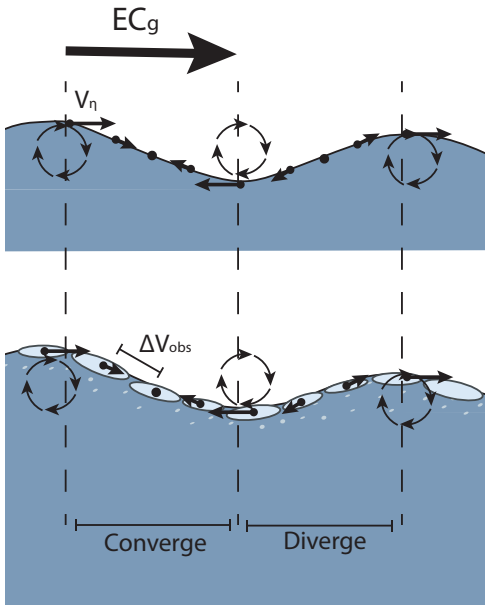

Figure 2.1: Schematic of motion induced by wave orbital motion at surface without ice (top) and with ice (bottom). The gradient in orbital velocity (V_η) results in relative velocity of ice floes (ΔV_{obs}) which causes floes to converge on the front face of the wave and diverge on the back face of the wave. Direction of wave energy flux (EC_g) is from left to right.

growth. Another proposed mechanism for energy dissipation is the generation of turbulence by shear between the rough ice and the ocean below [*Kohout et al.*, 2011]. Quantification of each proposed attenuation mechanism based on wave and ice conditions is needed for accurate prediction of wave conditions throughout sea ice-covered areas. The field observations for such quantification are rare, but efforts to model floe motion due to waves have advanced our understanding of these processes.

Modeling efforts to describe ice floe motion in periodic wave fields have utilized simple physical models to predict the kinematics and dynamics. The simplest model that can be thought of is that ice will simply follow wave orbital velocities (Fig. 2.1). A 2D model of a sea ice field was able to produce physically reasonable results of floe motion and collisions by simply assuming that floes follow orbital motions at the free surface [*Rottier*, 1992]. Many models for sea ice motion have been based on the slope-sliding model [*Rumer et al.*, 1979] in which there is an additional force on floes as a result of gravity pulling them down the sloped surface of each wave [*Grotmaack and Meylan*, 2006]. This theory has been utilized to describe expected frequency and magnitude of floe collisions [e.g., *Shen and Ackley*, 1991] and the associated attenuation of wave energy [*Shen and Squire*, 1998]. Another model using linear-potential flow theory has been suggested to be applicable where floe diameters are approximately equal to or greater than the wavelength [*Meylan et al.*, 2015].

Recent work has developed a numerical model for ice floe motion [*Herman*, 2011, 2013]. This model framework was adapted in *Herman* [2018] to describe surge motions, similar to those predicted by the slope-sliding model, and the resulting collisions. A crucial difference between the model by *Herman* [2018] and prior models is the method for computing the forces. While previous models assumed that the floes are infinitely small and forces were computed at the center of mass, the Herman model integrates forces over the surface of each floe.

A number of laboratory studies in recent years have examined the accuracy of models and theory describing ice floe motion and collisions. Experiments testing the response of a single floe to a wave field have found that floe motion can largely be predicted by simple

models when the radius is small compared to the wavelength [e.g., *Meylan et al.*, 2015; *Yiew et al.*, 2016]. Investigations of collisions have mostly used two floating disks representing ice floes to show that collisions can similarly be predicted by these simple models for floe motion [e.g., *Yiew et al.*, 2017; *Li et al.*, 2018]. There have, to our knowledge, not been any phase-resolved field observations of floe motion within natural sea ice or realistic wave fields (i.e., directional and irregular seas). The lack of measurements of pancake sea ice motion in the field stems largely from the difficulty of measuring them. Not only are ice-covered areas with substantial surface waves challenging to work in, but capturing lateral ice motion requires both spatial and temporal coverage.

Stereo camera systems have been gaining popularity as a method for measuring three-dimensional ocean wave fields from both stationary and mobile platforms. A number of recent studies have demonstrated the utility of this method in capturing phase-resolved wave processes, such as wave slope and breaking [*Schwendeman and Thomson*, 2017; *Benetazzo et al.*, 2017]. Additionally, shipboard stereo cameras are useful for measuring properties of ice-covered areas. Prior studies utilized stereo cameras to provide consistent and continuous estimates of sea ice characteristics, including thickness, texture, and floe size distribution [*Rohith et al.*, 2009; *Niioka and Kohei*, 2010; *Alberello et al.*, 2019]. To our knowledge, only one study has utilized stereo imagery to capture waves in ice [*Campbell et al.*, 2014]. They used a shore-based stereo imaging system on a lake to measure changes in wave spectra and energy flux through three different ice types. Their results indicated the potential of stereo systems for capturing the complex dynamics of waves in sea ice with both spatial and temporal characterization of the surface.

Here, a shipboard stereo video system is used to provide unique phase-resolved measurements of pancake sea ice floe velocities relative to each other. Measurements of relative velocities under a variety of wave conditions are compared to two models for pancake motion, with the goal of determining which model best describes in situ observations. We resolve the convergence (and collision) of ice floes at the crests of individual waves, as well as the divergence in the troughs of waves. We determine a characteristic relative velocity of the

ice floes for each set of conditions, and we relate these to bulk wave parameters. We then discuss the implications of the results for growth and development of pancake floes, and for wave energy loss in pancake ice. The relative velocity between floes is the primary variable controlling whether floes collide and the turbulence produced by their motion, so is thus applied as the key kinematic parameter for describing these dynamics.

2.2 Methods

2.2.1 Shipboard stereo camera setup

Measurements were made from shipboard stereo systems mounted on the rails of 04 deck of the R/V *Sikuliaq* during the 'Sea State and Boundary Layer Physics of the Emerging Arctic Ocean' experiment that took place October - November, 2015. All observations were made in newly formed ice in the Beaufort Sea marginal ice zone. A full map of the cruise track and description of conditions can be found in *Thomson et al.* [2018].

Two stereo systems [*Schwendeman and Thomson*, 2017] were mounted on the starboard and port rails aft of the bridge, 16.5 m above mean sea level. Each system consists of two Point Grey Flea2 cameras separated by 2 meters, as shown in Fig. 2.2a. Each of these cameras has a 9-mm fixed focal length lens, giving an approximately 30° horizontal field of view, and was mounted with a look angle 18° below horizontal. An additional Point Grey Flea2G camera was mounted centered between the Flea2 cameras, with a 2.8-mm fixed focal length lens. This camera had a wider field of view in order to capture the horizon in most images and allow the calculation of pitch and roll following *Schwendeman and Thomson* [2015]. All cameras record at 5 Hz.

A Novatel combined inertial motion unit (IMU) and global navigation satellite system (GNSS) was mounted with the cameras on the port side. The antennas can be seen in the photo in Fig. 2.2a. This IMU system is used to measure the position of the cameras, as well as the pitch and roll of the ship.

This study utilizes stereo observations made during five periods. Table 2.1 shows the

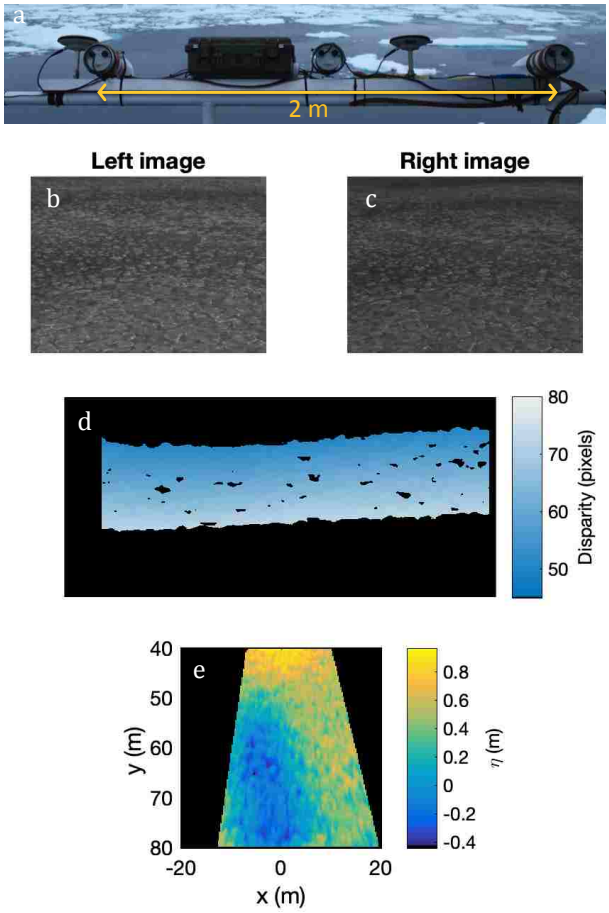

Figure 2.2: Stereo setup and example of processing steps. Panel (a) shows the stereo setup on the port side rail of the *R/V Sikuliaq*, with IMU-GNSS antennas mounted alongside cameras for stereo retrieval. Subsequent images show (b,c) an example of a pair of rectified stereo images, (d) the corresponding disparity map (in pixels), and (e) the resulting surface elevation map.

Table 2.1: Summary of bulk wave and ice conditions for observations. Wave parameters are obtained by processing 30-minutes stereo video bursts, and ice observations are from both processing stereo images (radius, r) and shipboard visual observations (thickness, z).

Observation	H_s [m]	T_e [s]	L_e [m]	r [m]	z [cm]	kr []
11 Oct 21:30	2.5	7.2	82	0.65	8	0.05
24 Oct 22:20	1.0	4.5	31	0.65	$\sim$20	0.13
24 Oct 23:18	0.9	4.6	34	0.52	5	0.10
01 Nov 19:17	1.0	4.3	29	0.51	6	0.11
01 Nov 19:35	1.1	4.8	37	0.58	7	0.10

date and starting time, and bulk wave and ice conditions for each. Stereo observations are collected in up to 30 minute bursts, which are processed to determine bulk wave characteristics following the steps described in the next section. Approximately 135 seconds of each observation are processed to characterize floe motion.

2.2.2 Wave estimates from stereo video

The stereo images are processed to obtain wave results following the methods described in *Schwendeman and Thomson* [2017]. The basic processing steps are calibration of the camera system, synchronization of all data streams, rectification of images, and rotation to earth reference frame. The methods are summarized here, but additional details may be found in *Schwendeman and Thomson* [2017].

Calibrations for the stereo camera setup are produced using the built-in routine in the Matlab Computer Vision toolbox. Sets of images of a 5x10 black and white checkerboard with 4" squares were acquired after the cameras were mounted on the ship during mobilization, prior to data collection. The Matlab calibration routine utilizes these image to determine both intrinsic and extrinsic parameters of the stereo cameras.

The Novatel IMU data were separately recorded, and thus it is necessary to synchronize

with images in post-processing. Offsets between the image and IMU data streams are determined using the cross-correlation of the time series of the pitch of the ship derived from the horizon tracking method from *Schwendeman and Thomson* [2015] and that recorded by the Novatel. These offsets are used to align IMU pitch and roll with the images, as the IMU is more accurate than the horizon tracking method, particularly in low wave conditions.

Rectification is a transformation process to project images onto a common plane, and is necessary for identification of matching pixels. Rectification slightly warps the epipolar lines in each image to make them horizontal, such that it appears that the images are simply horizontally offset. Pixels from left images are them mapped onto the right images to create a disparity map, showing the difference in pixel location for the same geographic location at each point. This is done using the Semiglobal algorithm in the Matlab Computer Vision Toolbox. An example of a pair of images and the resulting disparity map is shown in Fig. 2.2b-d.

The disparity map is rotated into the Earth reference frame in order to produce a surface elevation map in which waves can be observed. This is done using pitch and roll values from the synchronized IMU times series. Elevation map results are then interpolated onto a regular grid with 0.25 m spacing. An example map of surface elevations is shown in Fig. 2.2e.

Wave spectra are calculated from the gridded elevation maps using the Fast Fourier Transform (FFT) of the time series of surface elevation at each point, with 75% overlap. This is equivalent to treating each grid cell as a virtual wave buoy. The resulting spectra are then averaged together (all grid points) for each 5-minute burst of data analyzed. Bulk wave characteristics are determined from the spectra, including the significant wave height (H_s), peak wave period (T_p), and energy-weighted wave period (T_e). The energy-weighted wave period, defined as $T_e = \frac{\int E(f)df}{\int fE(f)df}$, is used to estimate average wavenumber k and wavelength L_e for use in subsequent calculations. Wavelength is calculated using $L_e = gT_e^2/2\pi$ as *Collins et al.* [2018] did not find any indication of deviation from linear deep water dispersion in these ice types.

Comparison with wave buoys

Previous application of this stereo setup in open water by *Schwendeman and Thomson* [2017] showed good agreement with traditional measurements from wave buoys. Here, we evaluate the stereo performance in the presence of sea ice before proceeding with the analysis. Spectra from the stereo system in sea ice are compared with simultaneously deployed SWIFT wave buoys. SWIFT buoys capture the wave signal by measuring horizontal displacement with a GPS receiver in 8-minute intervals, as described in further detail in *Thomson* [2012] and *Smith et al.* [2018a]. Figure 2.3 shows a comparison of wave spectra measured on 11 Oct 2015 21:30, where SWIFT 15 was within 2 km of the ship, and SWIFT 14 was approximately 20 km from the ship. The spectrum produced from the stereo video observations (black line) captures all the key features of the spectra from the wave buoys. There is a small amount of extra energy at the peak period as a result of uncorrected ship motion, which was observed in the open water comparison done by *Schwendeman and Thomson* [2017] as well, and additionally too much energy observed at frequencies below 0.06 Hz. There is clear noise contamination at high frequencies ($f > 0.4$ Hz), but those frequencies are beyond the scope of the present study.

Wave orbital velocities

The velocity due to wave orbitals $\overline{V_\eta}$ is the underlying motion that ice floes move with, and relative to, with the passage of each wave (Fig. 2.1). An estimate of the phase-resolved wave orbital motion can be calculated by applying linear wave theory using the time series of surface elevation, η, as

$$\overline{V_\eta}(t) = \frac{2\pi}{T(t)}\eta \tag{2.1}$$

Here, we use a time series of wave period T calculated from the η signal using the zero-crossing method with a smoothing interval of 2 seconds. This phase-resolved estimate represents a spatial average of velocities over the gridded domain. We can use the definition of $\eta =$

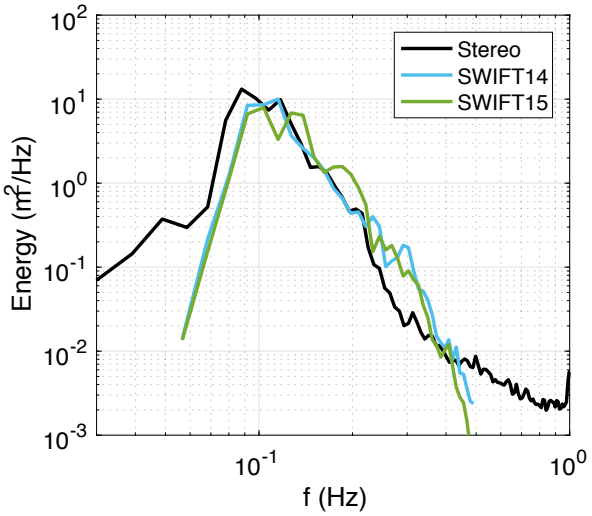

Figure 2.3: Comparison of wave spectra estimated from stereo video (black) with observations from two SWIFT wave buoys (light blue and green). Observations are from 11 Oct 21:30.

$\frac{H_s}{2}\cos(kx - \omega t)$ to estimate the time-average of the absolute orbital velocities as

$$\langle |\overline{V_\eta}| \rangle = \frac{2H_s}{T_e}. \tag{2.2}$$

2.2.3 Estimates of relative ice velocity

Observation of relative ice velocities

Estimates of relative sea ice velocities are made using a series of ortho-rectified images from one side of the stereo pair, recorded at 5 Hz. We use the left image, but the results are unaffected by the side chosen due to the overlapping footprint. An example of a single ortho-rectified image projected to geographic coordinates is shown in Figure 2.4, where the ship is located approximately at $y = 0$.

All estimates are made over a 8 x 25 m box centered in the domain, demonstrated by the blue rectangles in Fig. 2.4. Some observations contained periods with substantial rolling,

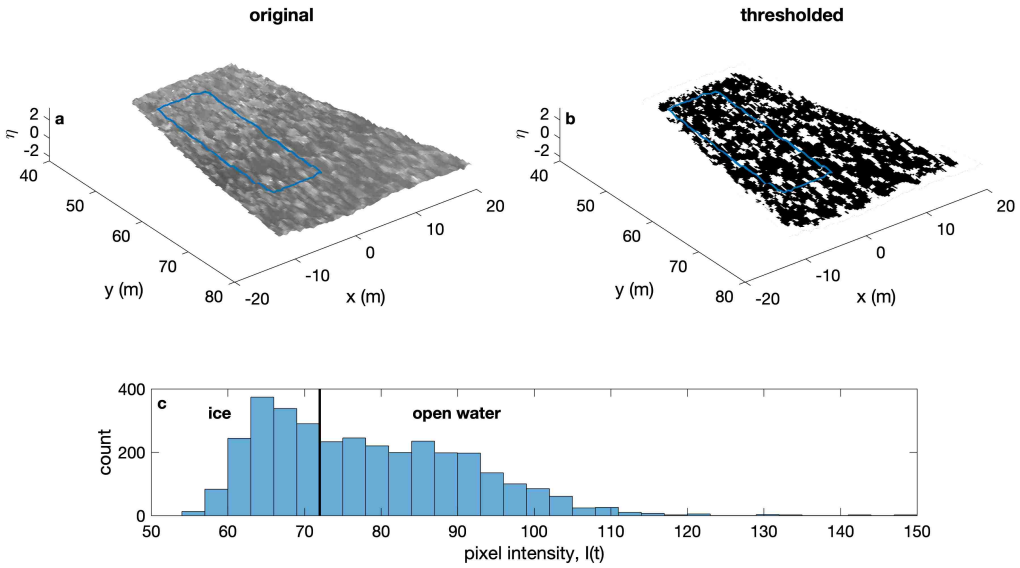

Figure 2.4: Example of (a) original and (b) thresholded images from stereo camera on 11 Oct 2015 21:30, projected onto geographic reference frame. Blue boxes represent the analysis box over which all values in Figure 2.6 are estimated. (c) Histogram of pixel intensities from original image. The horizontal line represents delineation of ice and open water based on Eq. 2.5.

such that the footprint of the stereo camera system changed significantly over time. The size of the analysis box was chosen to balance the desire to minimize the effect of rolling (by using a smaller box) with the need to provide a robust estimate (by doing a large spatial average). When the rolling was substantial enough such that any part of the analysis box was not captured, those images were ignored in subsequent calculations. The aspect ratio of the box was chosen to have the smallest reasonable width. As the wave propagation direction was typically parallel to the ship (or, in the x-direction of Fig. 2.4) this isolates the phase of a wave propagating through the box. The analysis box dimensions chosen limit the observable wave period to a minimum of 2.3 seconds.

Characteristic relative velocities of pancake floes ($\overline{\Delta V_{obs}}$) are calculated from images using

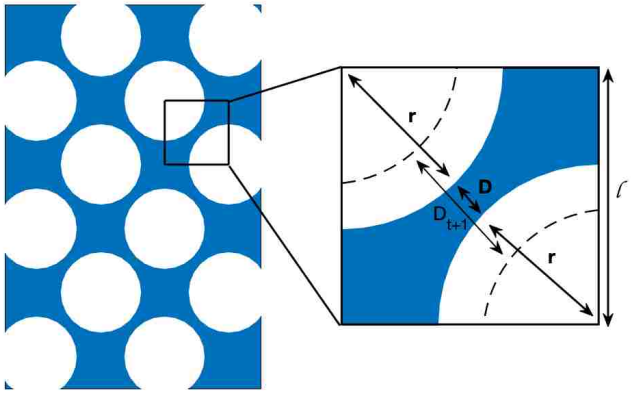

Figure 2.5: Schematic demonstrating the calculation of average distance between floes, in Eq. 2.4, using the areal concentration and floe radius. This method assumes uniform floe radius and uniform floe spacing. Dotted lines demonstrate the increase in floe distance D as floes diverge at some future time $t + 1$.

the change in average distance between floes. In order to calculate average distance between floes, we assume that the floes in each image have uniform radius and are evenly spaced, such that the areal concentration A can be estimated as

$$A = \frac{\frac{1}{2}\pi r^2}{l^2} \tag{2.3}$$

where l is the length of the box formed by connecting center of floes (shown schematically in Fig. 2.5). The average distance between floes is calculated as:

$$\overline{D_{obs}}(t) = \sqrt{\frac{\pi(2\overline{r})^2}{4A(t)}} - 2\overline{r} \tag{2.4}$$

where $\overline{r}$ is floe radius, and overbars indicate spatial averages (Fig. 2.5). Estimation of $\overline{r}$ and A to determine $\overline{D_{obs}}$ from observations are described below and demonstrated in Figure 2.6.

Floe radius is determined from the equivalent diameter of objects in thresholded images, produced using an adaptive threshold from the Matlab image processing toolbox. The right panel of Fig. 2.4 shows an example thresholded image, where each white object is considered an individual floe. An average $\overline{r}$ is calculated for each frame. A linear fit to the time series of radius $\overline{r}$ is used to avoid noise associated with the adaptive threshold algorithm and specific floes moving in or out of the box. Shading in Figure 2.6a-d represents the propagation of standard error associated with this linear fit, which is small. The accuracy of the estimate of radius is also limited by the pixel size, which is approximately 2 cm in the near-field and 12 cm in the far-field.

The change in areal concentration of sea ice over time, $A(t)$, is calculated from the change in pixel intensity $I(t)$. Concentration is calculated from the pixel intensity, rather than the coverage in thresholded images, as the adaptive threshold used adjusts based on the brightness so that resulting binary images do not well represent changes in concentration over time. However, the thresholded images give a good estimate for the average areal coverage for the entire time series, as can be qualitatively seen in the example in Fig. 2.4. The average areal concentration from binary, thresholded images ($A_{thresholded}$) is used to normalize the pixel intensities, such that the average value produced by both methods are equivalent:

$$A(t) = \frac{\overline{I}(t)}{\left\langle \overline{I}(t) \right\rangle / \left\langle A_{thresholded} \right\rangle} \tag{2.5}$$

The distribution of pixel intensity is not clearly bimodal (Figure 2.4c), as would be ideal to clearly separate sea ice from open water. The threshold value (shown by the vertical black line) is instead determined as the pixel intensity that is necessary to produce that same average concentration that is estimated by applying an adaptive threshold. An example of the concentration estimated from thresholded images and pixel intensities is shown in Fig. 2.6b. Throughout, the overline is used to represent a spatial average, and brackets are used to represent a temporal average.

Time series of average distance between floes (Fig. 2.6c) are calculated from time series of average radius and concentration using Eq. 2.4. The time series of average distance between

floes is linearly de-trended if it is complete (i.e. without any periods of substantial rolling), and smoothed with a span of 5 points (1 second). Time series of relative velocity between floes are then calculated using the change in average distance between floes,

$$\overline{\Delta V_{obs}}(t) = \left(\frac{d\overline{D_{obs}}(t)}{dt}\right)\frac{1}{2} \tag{2.6}$$

The derivative of the distance over time must be divided by two to determine the relative speed of each floe in a pair. In order to avoid artificially introducing a lag, this derivative is done using distances before and after each point in time, i.e. $\overline{\Delta V}(i) = \left(\frac{D_{i+1}-D_{i-1}}{t_{i+1}-t_{i-1}}\right)\frac{1}{2}$. The result is a characteristic speed of ice floes relative to each other within the domain. Although this estimate is spatially averaged within the domain, it is phase-resolved in time.

Prediction of ice velocities based on wave slope

Relative motion between floes is expected based on the gradient of orbital velocities along the sloped wave surface, as shown in the schematic in Figure 2.1. We can estimate this relative motion using the map of surface elevation over the field of view for each frame, produced from the stereo video processing (e.g., Fig. 2.4). A 2D linear fit is used to estimate the maximum slope ($\frac{d\eta}{dx}$) within the processing box in each frame. The spatial average of the relative velocity between floes is then

$$\overline{\Delta V_{\eta}}(t) = \frac{2\pi}{T_e}\frac{d\eta}{dx}2\overline{r} \tag{2.7}$$

The average diameter of floes ($2\overline{r}$) is used here as approximate scale over which relative motion is occurring.

Prediction based on Herman model

The average relative velocity of floes predicted by the *Herman* [2018] model is also calculated using the change in distance between floes. The average distance between floes based on Herman's Eq. 27 is:

$$D_H(t) = 2r\left(\frac{1-A}{A}\right) - 2\left(\frac{H_s}{2}\right)\sin\left(\frac{kr}{c}\right)\cos\left(\omega t + \frac{kr}{A}\right) \tag{2.8}$$

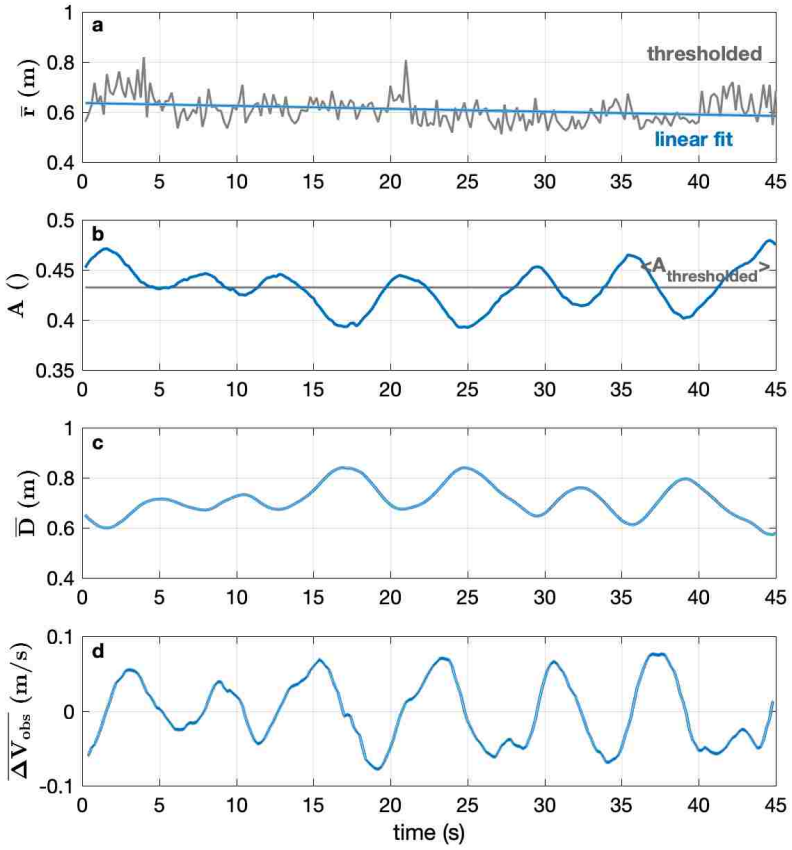

Figure 2.6: Example time series of observed floe characteristics, demonstrating methods used to estimate relative velocities. (a) Linear fit (blue line) to average radius in each frame (grey line). Shading represents standard deviation of values from frames. (b) Aerial ice coverage determined from image intensity (Figure 2.4a), normalized to the average coverage in thresholded images (Figure 2.4b; Eq. 2.5). (c) Distance between floes calculated using Eq. 2.4. (d) Characteristic relative velocity of floes calculated using Eq. 2.6.

This equation assumes initially equally spaced floes with identical radii, and disregards the effect of friction. We use the time-averaged concentration, $\langle\overline{A}\rangle$, such that the time variation is primarily a result of the wave motion $\overline{\eta}$ averaged over the box in Fig. 2.4:

$$\overline{D_H}(t) = 2\overline{r}\left(\frac{1-\langle\overline{A}\rangle}{\langle\overline{A}\rangle}\right) - 2\,\overline{\eta}\sin\left(\frac{k\overline{r}}{\langle\overline{A}\rangle}\right) \tag{2.9}$$

Similar to Eq. 2.6, the relative velocity between floes predicted by *Herman* [2018] is the change in average distance between floes over time:

$$\overline{\Delta V_H}(t) = \left(\frac{d\overline{D_H}(t)}{dt}\right)\frac{1}{2} \tag{2.10}$$

2.3 Results

2.3.1 Example phase-resolved velocities

The time series in Figure 2.7 shows an example of phase-resolved orbital and relative floe velocities using the first 45 seconds of the observations from 11 Oct 21:30. The net motion of floes due to orbital velocities (Fig. 2.7b), calculated from mean surface elevation (Fig. 2.7a), is approximately an order of magnitude larger than the relative motion of floes (Fig. 2.7d). As ice floe motion closely follows the wave motion, relative velocities are expected to be small.

The comparison of relative velocities from observations with predictions from the two models in Fig. 2.7d show that both models are able to describe magnitude of velocities, as well as key features of temporal variability. Comparison of the time series' predicted by the Herman model and wave slope methods with observations have correlation coefficients of $R^2 = 0.62$ and $R^2 = 0.77$, respectively. We can further see that the Herman model predicts relative velocities well because it is capturing variability in the average distance between floes (Fig. 2.7c).

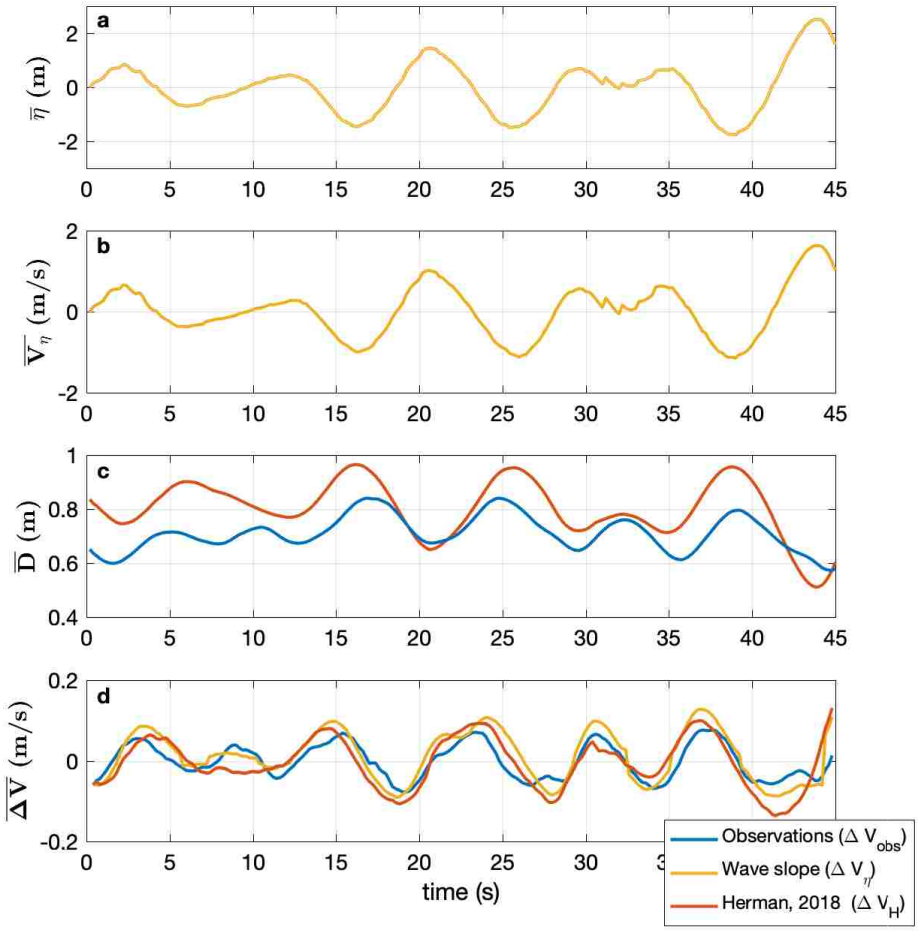

Figure 2.7: Example time series of mean and relative velocity estimates for the first 45 seconds of observations on 11 Oct 21:30. (a) Mean surface elevation; (b) mean orbital velocity (Eq. 2.1); (c) average distance between floes from observations and Herman model; and (d) relative velocity estimates for the three different methods.

2.3.2 Comparison of relative velocities

Relative velocities were estimated using the three methods described for all five observation periods (Table 2.1). Figure 2.8 compares the average relative speed $\langle|\overline{\Delta V}|\rangle$ determined by each method as a function of bulk wave steepness (H_s/L_e). In general, both models replicate the observations well. The bars represent the standard deviation of relative speed, and so are expected to be large based on the variation in velocity at different points in a wave period. We generally observe larger relative velocities of floes with increasing wave steepness. Steeper waves are expected to result in a larger gradient of orbital velocities at the surface. There was no significant phase lag between the observed relative velocities and predictions from the models for any of the observations.

Velocity estimates from observations are expected to have some error based on the assumptions behind Eq. 2.4: that floes have uniform shape and radius, and are evenly spaced at all times (Fig. 2.5). Although typically disc-shaped, pancakes are rarely perfectly circular; pancake sea ice has an average aspect ratio of 1:1.6 [*Alberello et al.*, 2019]. The ellipticity of pancakes will affect absolute values of D_{obs} calculated, but should have minimal affect on relative distance and thus relative velocity if an equivalent radius is used. The calculation of relative distances and velocities are more likely to be affected by assuming that floes are all the same average radius and evenly spaced. Floe size distributions of pancakes do not seem to follow any sort of power law distribution, but do typically have some spread in observed radii [*Alberello et al.*, 2019]. Due to the challenge of identifying and tracking individual floes, we are unable to calculate the associated error. These assumptions emphasize that calculated $\overline{V_{obs}}$ should be treated as a characteristic relative speed, rather than an absolute relative speed.

Velocity estimates from both models are strongly dependent on the choice of defining wave period and the associated wavenumber. The energy-weighted wave period is used throughout to best represent the wave conditions driving motion of floes. Use of the peak wave period results in substantially lower estimates of relative velocity for all methods (not

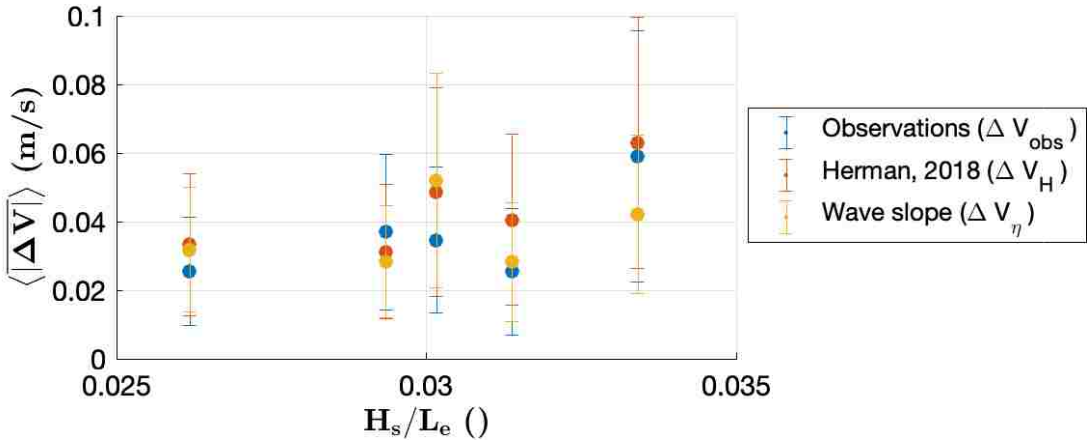

Figure 2.8: Average absolute value of relative floe velocities from observations (blue) compared with expectation based on gradient in orbital motion from wave slope (yellow), and Herman model (red), as a function of wave steepness (determined from bulk parameters). Bars represent standard deviation of absolute values of relative velocities.

shown).

2.3.3 Relative velocity estimates from bulk wave and ice parameters

The model estimates in Figure 2.8 require detailed knowledge of the time evolution of mean surface elevation η, in addition to bulk wave and ice characteristics. As this information is rarely available, we introduce estimates from these models that rely solely on bulk estimates. We propose a method to estimate relative velocities based on bulk parameters by using the definition of $\eta = \frac{H_{rms}}{2}\cos(kx - \omega t)$ to estimate the wave slope

$$\frac{d\eta}{dx} = \frac{kH_s}{2\sqrt{2}} \cdot -sin(kx - \omega t) \tag{2.11}$$

Here, $H_{rms} = H_s/\sqrt{2}$ has been substituted in so that the more commonly reported significant wave height can be used. To get a characteristic value of relative velocity, comparable to

those in Fig. 2.8, we average the absolute value and substitute in $k = 2\pi/L$ to get

$$\left\langle \left| \frac{d\eta}{dx} \right| \right\rangle = \frac{\pi H_s}{L_e\sqrt{2}} \cdot \frac{2}{\pi} = \frac{2H_s}{\sqrt{2}L_e} \tag{2.12}$$

where $\langle\rangle$ represents a temporal average. Substituting this back into Eq. 2.7 gives

$$\left\langle |\overline{\Delta V_\eta}| \right\rangle = \frac{8\pi}{\sqrt{2}} \cdot \frac{H_s \overline{r}}{T_e L_e} \tag{2.13}$$

As wave orbital velocities are proportional to H_s/T_e (Eq. 2.2), Eq. 2.13 can be rearranged to determine relative floe velocity normalized by mean floe velocity as a function of the ratio of average radius to wavelength. Figure 2.9 compares the normalized velocity determined from bulk parameters (grey line) with values from observations and both models. The prediction using bulk parameters generally captures the observed patterns, but with values that are an average of 50% higher than observations. The over-prediction may be a result of the drag and added mass of the ice floes, both of which would reduce the relative velocities. In our observations, average floe radius is typically a few percent of the wavelength and relative velocities are around 5-10 percent of wave orbital velocities.

The simple model using bulk parameters predicts that normalized relative velocities should increase with larger values of r/L_e. The observed normalized relative floe velocities generally follow this pattern, with the main exception being the observation furthest to the right in Figure 2.9, which is from the 24 Oct 22:20 case. This observation coincided with the thickest sea ice. Here, added mass associated with sea ice may be important. However, both models agree well with observations, which indicates that conditions resulting in lower relative velocities are well captured by the time variation of the wave field.

The shaded error bar in Fig. 2.9 shows the standard deviation in relative speed that would be expected based on the same assumptions behind Eq. 2.13. The deviation of observations from the mean (blue bars) are comparable to those predicted. Disparities in both mean and standard deviations of relative velocity observations and bulk predictions may be a result of divergence from monochromatic wave shape, and the smaller spatial and temporal coverage of the domain compared to bulk parameters.

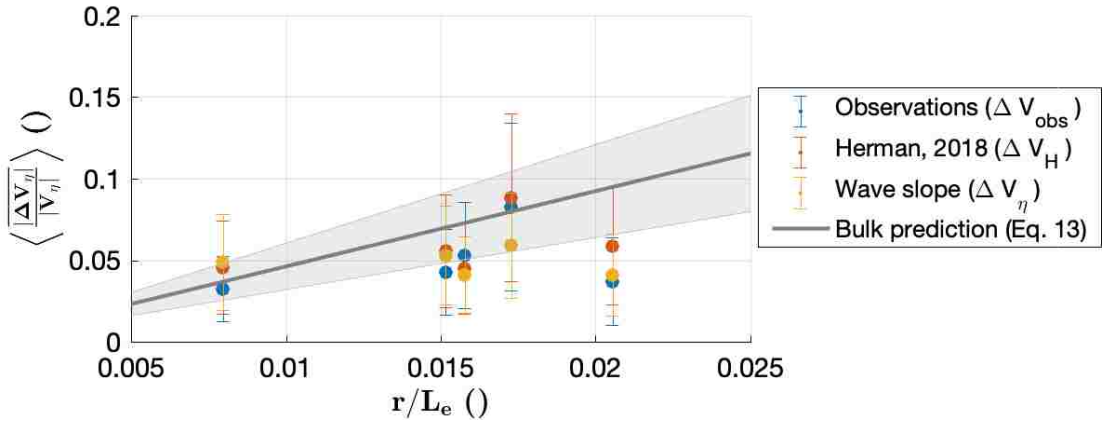

Figure 2.9: Average relative floe velocities normalized by orbital velocities as a function of the ratio of average floe radius to bulk wavelength. As in Fig. 2.8, points represent velocities from observations (blue), expectation based on gradient in orbital motion from wave slope (yellow), and Herman model (red), and bars represent standard deviation of absolute values of relative velocities. The grey line represents expectation based on linear theory, determined by bulk wave parameters (Eq. 2.13), and shading represents the standard deviation of relative velocity resulting from the assumption of monochromatic regular waves.

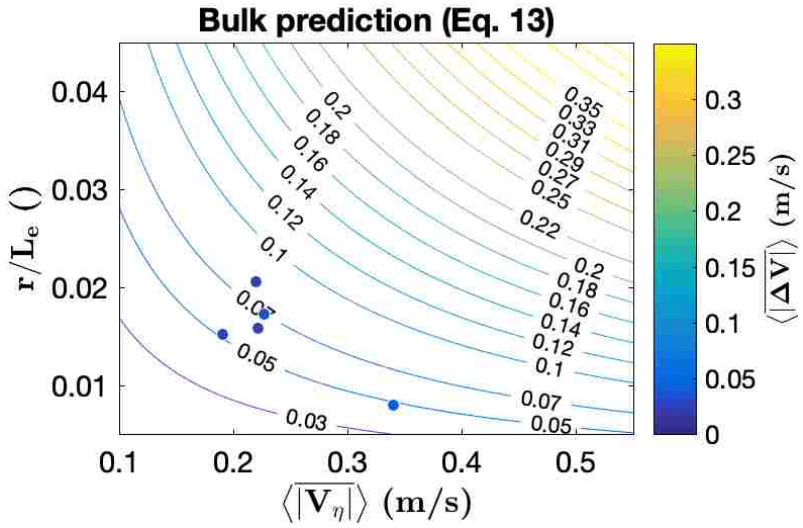

Figure 2.10: Contour plot of average relative floe velocity predicted using linear theory with bulk wave and ice parameters (Eq. 2.13). Filled points show observed values within the parameter space.

Predictions of relative velocity based on Eq. 2.13 are shown in Fig. 2.10 for a range of wave and ice values that may be expected in sea ice. Across the parameter space, relative velocities are always small ($\mathcal{O}(10^{-1})$). These relative velocities have implications for energy loss associated with collisions and turbulence, as discussed further in the next section. Values are expected to increase as both wave orbital velocities ($\langle\overline{|V_\eta|}\rangle$) and relative floe size (r/L_e) increase.

It should also be noted that observations presented here span a narrow parameter space compared to what might occur in polar oceans. Wave heights range from 0.9-2.5 meters, and energy-weighted periods range from 4.3-7.2 seconds, with all but one observation between 4-5 s (Table 2.1). Values of kr, which have been proposed to have an inverse relationship with how closely ice follows wave motion [*Herman*, 2018], are all well below one (i.e., we expect the ice to follow the wave motion quite closely).

We can derive a similar expression for characteristic relative velocities predicted from

bulk characteristics using the Herman 2018 model by integrating Eq. 2.9.

$$\langle|\overline{\Delta V_H}|\rangle = 2\frac{H_s}{T_e} \cdot \sin\Big(\frac{8\pi^2}{g}\frac{\overline{r}}{T_e^2 H_s}\Big) \tag{2.14}$$

This simple model can also be re-arranged to determine relative velocities normalized by orbital velocities (Eq. 2.2) as a function of bulk wave parameters and average floe radius. Predictions using this equation show similar patterns based on bulk wave parameters as those predicted by Eq. 2.13, and so are not shown here. *Herman* [2018] suggested that floes should more closely follow wave motion as kr approaches 0 and that floe motion is less a function of the radius when $\frac{2\pi}{k} > 10r$, as is the case for all observations here (Table 2.1). In this regime of small floes, observed relative floe motions do not vary significantly from the wave motion. As ice floes become larger, we may expect the *Herman* [2018] model to become more accurate. However, this has not been tested as we have sparse observations throughout the parameter space (Fig. 2.10). More observations are needed to determine the validity of these models under such conditions.

2.4 Discussion

2.4.1 Implications for pancake growth

It is well understood that the formation of pancakes occurs as a result of wave motion during ice formation conditions, but our ability to predict the growth rate and size of pancake floes is still limited. *Shen et al.* [2001] proposed a theoretical model for growth of pancake ice in a wave field, in which the lateral extent of floes is limited by either tensile or bending stress resulting from the surface wave field. Their theoretical model allows estimation of floe radius based on the tensile stress resulting from the wave field as

$$\overline{r} = \frac{1}{2}\sqrt{\frac{C_2 L_e^2}{\pi^2 \frac{H_s}{2} g \rho_{ice}}} \tag{2.15}$$

where C_2 is tensile mode parameter representing the bonding strength associated with freezing. *Roach et al.* [2018b] used simultaneous observations of floe growth and wave conditions

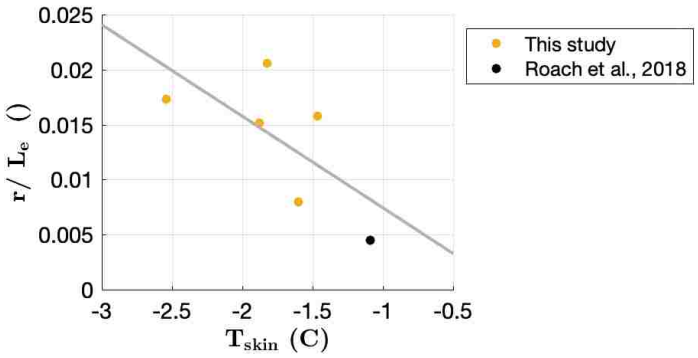

Figure 2.11: Average floe radius, scaled by wavelength, as a function of skin temperature. Yellow points are from this study, and black point is from *Roach et al.* [2018b]. $R^2 = 0.45$

from a SWIFT buoy during a pancake formation event to provide the first in situ validation of this model. The radius increased linearly as a function of the tensile failure mode $\sqrt{2L_e^2/H_s}$ (see their Fig. 8), indicating that lateral growth was well captured by the tensile stress model (Eqn. 2.15). Based on the fit, the tensile mode parameter was estimated as $C_2 = 0.167$ [N/m^2] for the observed conditions. This value is expected to vary under different conditions, and to be related primarily to the temperature.

We use the observations from the present study to test these formulations for pancake growth. The observations span a range of atmospheric and ocean conditions, suggesting a range of tensile mode parameters. We find that the radius of floes, scaled by the wavelength, is related to the skin temperature T_{skin}, measured here by a floating thermistor [*Persson et al.*, 2018a] as shown in Fig. 2.11. This suggests that the skin temperature is important for lateral growth of floes, and may be used to constrain the tensile mode parameter, C_2.

We use the average radii and tensile failure modes based on bulk wave characteristics to calculate the C_2 for each observation (Eq. 2.15). C_2 values ranged from 2.1 to 39 N/m^2. Values from this study and *Roach et al.* [2018b] are compared with the skin temperature in Figure 2.12. These results show that there is a good negative correlation between T_{skin} and

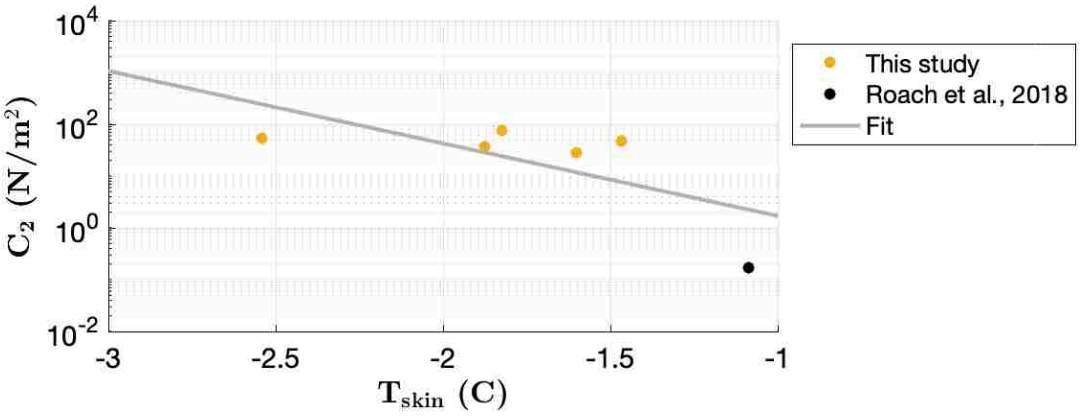

Figure 2.12: Tensile mode parameter C_2 as a function of the ocean skin temperature T_{skin}. Yellow points are those determined for this study using Eq. 2.15, and black point is from *Roach et al.* [2018b]. Logarithmic fit to these data (grey line) is given in Eq. 2.16.

C_2 ($R^2 = 0.46$). A logarithmic fit gives the function

$$\ln(C_2) = -3.2T_{skin} - 2.7 \tag{2.16}$$

As these observations span a small range of floe sizes, additional observations within the parameter space may improve this relationship or illuminate dependencies on other key variables. Parameterizations of the tensile failure mode may then be used to estimate typical floe sizes as a function of ocean skin temperature and bulk wave parameters by merging with Eq. 2.15. Additionally, combining these results with the simple models in Eqs. 2.13 and 2.14 may allow estimation of the normalized relative velocity with only ocean skin temperature and wave height.

2.4.2 Implications for wave energy loss

Improving estimates of the rate of wave energy dissipation remains an essential question for progressing understanding of waves in sea ice [*Shen*, 2019]. Many possible mechanisms contributing to the total rate of wave energy attenuation have been proposed. Here, we

discuss two possible mechanisms related to the relative velocities observed: collisions and turbulence.

The motion of floes with waves can result in collisions of floes, particularly when ice concentrations are high and waves are large. The force associated with floe-floe collisions has been described as a mechanism for wave energy attenuation [*Shen et al.*, 1987]. Collisions are also a key component of pancake ice formation and growth [*Shen et al.*, 2001], and the associated energy goes at least in part into lateral floe growth and evolution (such as through welding). Dissipation of wave energy from collisions is expected to scale with the relative kinetic energy of the ice floes. We estimate it here, in a fashion similar to the formulation in *Shen et al.* [1987], by using the square of the observed relative velocities to describe the change in kinetic energy that occurs when ice floes collide a rate of once per wave period T_e :

$$D_{collisions} \approx \frac{\Delta KE}{AT_e} \approx \frac{\frac{1}{2}\rho_{ice} z_{ice} \left\langle |\overline{\Delta V_{obs}}| \right\rangle^2}{T_e} \tag{2.17}$$

This represents the maximum kinetic energy that can be harvested by floe-floe collisions, assuming a restitution coefficient of 0 [*Shen et al.*, 1987].

Additionally, the differential velocity of ice relative to the water results in turbulence generation at the ice-ocean interface, which may dissipate wave energy. *Kohout et al.* [2011] made estimates of wave attenuation associated with this process, which showed frequency dependence in agreement with field observations of attenuation. Dissipation of wave energy from turbulence generated by shear between pancakes and the ocean scales with the relative velocity, so is approximated here using observed relative velocities as:

$$D_{turbulence} \approx \rho_w \left\langle |\overline{\Delta V_{obs}}| \right\rangle^3 \tag{2.18}$$

where ρ_w is the density of the ocean water. This approximation is similar to scalings that are used for law-of-the-wall boundary layers, though such a classic layer is not necessarily expected beneath pancake ice. Here, $\left\langle |\overline{\Delta V_{obs}}| \right\rangle$ is analogous to the friction velocity u^*, or the velocity scale of the energy containing eddies in a turbulent cascade. This is supported by the magnitude of the turbulent velocity fluctuations (also a few cm/s) measured just below

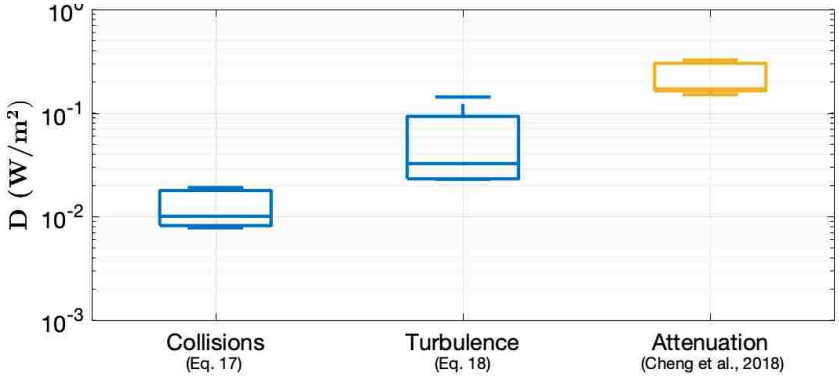

Figure 2.13: Boxplot showing total dissipation of wave energy D expected to be a result of floe-floe collisions and ice-ocean turbulence generation, compared to the dissipation associated with observed wave energy attenuation between wave buoys (yellow). Each bar shows the average, inter-quartile range, and total range for the five observations.

the ice using SWIFT buoys [*Smith and Thomson*, 2019].

We compare total dissipation rates estimated for the two relevant wave energy loss mechanisms ($D_{collisions}$ and $D_{turbulence}$) with those calculated from observed wave attenuation (Figure 2.13). Total wave energy dissipation per unit area is estimated based on observed wave attenuation as the change in wave energy between two SWIFT wave buoys [temporally collocated by *Cheng et al.*, 2017] as

$$D_{attenuation} \approx \frac{dEC_g}{dx} \tag{2.19}$$

Some of the SWIFT deployments used here are up to 3 km away from the stereo video observation area, but are expected to generally capture the same wave attenuation conditions. These observations correspond to average wave attenuation rates ranging from $\alpha = 2 \times 10^{-5}$ to 2×10^{-4}.

The estimates of energy dissipation from ice-ocean turbulence are larger than those from from collisions. Although there can be high kinetic energy loss associated with collisions, they are brief in time compared to the relatively continuous energy loss that can occur via

turbulence generation. As both proposed attenuation mechanisms scale with the relative ice velocities, they are expected to increase with wave steepness. This is consistent with results from a recent laboratory experiment which found that attenuation is greater for the same sea ice with a steeper wave field [*Toffoli et al.*, 2015].

Observations from the Sea State experiment in 2015 have resulted in a number of recent studies providing insight into turbulence under pancake and frazil sea ice. Measurements of near-surface turbulent dissipation across a range of wave and sea ice conditions were used to suggest that the production of turbulence underneath thin pancake sea ice largely balances the wind input [*Smith and Thomson*, 2019]. Using the same dataset, *Voermans et al.* [2019] showed that the turbulence underneath the ice can account for nearly all of the observed wave attenuation. Although the mechanisms proposed in these papers may seem contradictory, the results of the present study help us reconcile the results.

We find that the relative velocity of floes, which likely generates turbulence through ice-ocean shear, is a function of the bulk steepness of the waves (Fig. 2.8). The input of wind energy into the waves will increase (or maintain) wave steepness [e.g., *Plant*, 1982], even as energy is being attenuated by the sea ice. *Smith and Thomson* [2019] found that the rate of wind input is suppressed in the ice, but that the wind is still doing work on the surface. Thus, this wind work may maintain wave steepness (which would otherwise decrease rapidly in ice), which in turn drives the relative motion of the pancakes and turbulent eddies of a similar kinematic scale just below the ice. In other words, dissipation (and therefore attenuation) increases with higher wind input because the waves are generating turbulence through relative ice motions. This is in agreement with recent work showing that wind input may contribute a significant portion of the attenuated wave energy, and so is essential to consider in order to accurately predict wave energy [*Li et al.*, 2017].

The sum of wave energy dissipation that is estimated by these relative velocities is still somewhat lower than the dissipation required to explain the observed wave attenuation (Fig. 2.13). This discrepancy is likely a result of other attenuation mechanisms that have not been considered here. For example, recent work by *Rabault et al.* [2019] suggested that

the convergence of frazil may create small scale eddy structures that dissipate energy via turbulence. This has similar underlying mechanisms to attenuation from pancake collisions discussed. However, it can occur much more frequently due to the potentially small size and high concentration of frazil, and so could dissipate more energy overall than floe-floe collisions.

All of these possible mechanisms are encapsulated in the viscosity and elasticity parameters used in viscous and viscoelastic models for attenuation [e.g., *De Carolis and Desiderio*, 2002; *Wang and Shen*, 2010; *Sutherland et al.*, 2019], which are calibrated by fitting the model to observations [*Cheng et al.*, 2017; *Doble et al.*, 2015]. However, one major critique of these models is that unrealistically high viscosity values are necessary in order to describe attenuation observations. For the observations used in this study, *Cheng et al.* [2017] calculated viscosity parameters generally between 3.2-5.2 m^2/s, except for a value of 27 m^2/s from the first observation (11 Oct). The mechanism proposed by *Rabault et al.* [2019] could possibly account for the extremely high viscosity values necessary to reproduce attenuation observations using viscous models, but there has not yet been any work to constrain dissipation via this mechanism. Describing this process is challenging due to the lack of knowledge regarding frazil concentration and distribution in the water column. Determining the dominant attenuation mechanism specific to different wave and ice conditions remains a key requirement, as well as a key challenge, for understanding wave-ice interactions.

2.5 Summary

Shipboard stereo video is able to simultaneously resolve wave motion and relative motion of pancake floes. Stereo video captured in the Beaufort Sea in 2015 provides the first in situ observations of relative floe motion in a wave field that are resolved in both space and time.

The relative velocities of floes are captured well by existing models using observations of the surface elevation and slope. Simplifications of these models that utilize bulk parameters predict the general magnitude of relative velocities, but may somewhat over-estimate velocities, especially as sea ice radii increase. Additional observations under different wave

forcing and ice conditions are necessary to determine the appropriate correction factors for estimating characteristic relative floe velocity with bulk parameters only.

The relative velocity of floes is relevant for two possible mechanisms that contribute to wave energy loss: floe-floe collisions and turbulence from ice-ocean shear. Estimates of wave energy loss from ice-ocean turbulence exceed those from pancake collisions, and can explain most of the observed wave attenuation. The steepening of waves with wind input in the ice may increase the relative velocities of floes, and thus the attenuation of wave energy through turbulence may be intrinsically related to wind forcing.

Chapter 3

EPISODIC REVERSAL OF AUTUMN ICE ADVANCE CAUSED BY RELEASE OF OCEAN HEAT

3.1 Introduction

Autumn in the Arctic Ocean is characterized by decreasing temperatures, decreasing solar radiation, and strong heat fluxes from the ocean surface to the atmosphere. Areas of open water freeze as the sea ice advances southwards, with ice formation largely controlled by changing atmospheric conditions and reduced solar input.

In recent decades, the total area of seasonally open water has expanded, and thus a greater area of ice advance is required to return to the full winter ice cover [*Jeffries et al.*, 2013]. This spatial signal is accompanied by a temporal one: the ice advance has also been occurring later each autumn [*Meier*, 2017; *Stroeve et al.*, 2016]. This is especially true in the Beaufort Sea, the marginal sea north of Alaska and western Canada that contains the southernmost part of the deep Canada Basin. For the Beaufort Sea in particular, the transition from open water to seasonal ice has been occurring an average of 1-2 days later per year, with a net shift of ice advance from 1979 to 2010 almost one month later in the climatology [*Stammerjohn et al.*, 2012]. This delayed ice advance is responsible for longer open water periods [*Galley et al.*, 2016].

Some consequences of summer sea ice decline over the Canada Basin include enhanced surface wave generation, greater air-sea exchanges, and increased solar heating of the upper ocean. Large expanses of open water in the summer Arctic Ocean in recent years allow winds to form large swells that propagate into the ice pack [*Asplin et al.*, 2012, 2014]. Observations of discrete large wave events [*Asplin et al.*, 2012; *Collins et al.*, 2015; *Thomson and Rogers*, 2014b] are indicative of a general shift in the wave climate towards larger waves in the Beaufort Sea [*Stopa*, 2016; *Thomson et al.*, 2016b]. The extent to which the increasing wave climate has enhanced mixing in the surface waters, via mechanisms such as Langmuir turbulence [*D'Asaro et al.*, 2014], is not known. Larger surface waves increase turbulent fluxes and gas exchange at the surface [*Loose et al.*, 2009]. In open water, there are significantly larger energy exchanges between the upper ocean and the atmosphere [*Maykut*, 1978]. In the marginal ice zone, the area of transition between open ocean and sea ice pack, the high-

frequency portion of the wave spectrum is suppressed [*Zippel and Thomson*, 2016]. Although there are clear signals of these mechanical changes in the expanding marginal ice and open water zones, the thermodynamic feedbacks are not well understood.

The longer period of open water has delayed autumn ice advance by increasing the amount of solar radiation stored in the upper ocean [*Jackson et al.*, 2010]. The surface mixed layer in the Canada Basin is typically shallow (0 to 10 m) at the beginning of autumn. This is a result of freshwater input (sea ice melt and river input) and the lack of strong forcing (i.e., storms) to cause mixing during summer [*Peralta-Ferriz and Woodgate*, 2015]. During summer in the Canada Basin, sea ice melts to form a stratified layer called the summer halocline that is typically observed at 10 to 20 m [*Jackson et al.*, 2010]. Stratification in the summer halocline traps solar radiation, forming a near-surface temperature maximum (NSTM) that typically resides at 20 to 35 m and is a common feature in the Beaufort Sea region of the Arctic Ocean [*Maykut and McPhee*, 1995]. The NSTM typically has a salinity between 28-30 psu, and is defined as being less than 31 psu [*Jackson et al.*, 2010]. It stores a substantial amount of heat, with an average of 0.24° above freezing in the eastern Canada Basin (as observed in October 2005) [*Jackson et al.*, 2010]. Although the NSTM has been observed as a year-round feature, it normally deepens, cools, and disappears throughout the autumn and winter [*Jackson et al.*, 2010; *Steele et al.*, 2011]. The saltier, cooler region below the NSTM is thought to be the remnant winter mixed layer from the prior year [rWML *Jackson et al.*, 2010]. Below the rWML is Pacific Summer Water (PSW), which is a warm, relatively salty water mass, typically between 30-32 psu and over 0.5°C in the Canada Basin [*McLaughlin et al.*, 2011].

Average temperatures of both the surface mixed layer and NSTM have been increasing as a result of longer open water season in recent decades, which provides increased opportunity for input of solar radiation to the upper ocean [*Jackson et al.*, 2010; *Perovich et al.*, 2007; *Stroeve et al.*, 2014]. In particular, the NSTM in the Canada Basin warmed by about 1.5°C and freshened by about 4 psu from 1993-2009 [*Jackson et al.*, 2011]. Additionally, the summer halocline and NSTM have been shallower on average, with shoaling observed from 2002-2007

likely due to the increase of *in situ* sea ice melt [*Jackson et al.*, 2010].

Various studies using ice mass balance buoys (IMBs) and ice tethered profilers (ITPs) deployed on thick, multi-year ice floes in this region have shown entrainment of heat from the ocean mixed layer and NSTM to be a primary driver of sea ice melt through summer and autumn. *Perovich et al.* [2008] used IMB data to show that solar heating of the ocean was a primary driver for bottom melt of sea ice during the summer of 2007. *Jackson et al.* [2012] used ITPs deployed on 3-m thick ice floes north in the Canada Basin to show that solar heat stored in the NSTM during the following autumn and winter was periodically entrained into the mixed layer, corresponding to brief periods of bottom melt of thick sea ice. Similarly, *Timmermans* [2015] observed melt at the bottom of 3-4 m thick ice floes as a result of erosion of the NSTM. The correlation of ice thinning with loss of heat from the NSTM suggests that oceanic heat fluxes are causing sea ice melt and decreased winter ice growth. The ice melt that would be inferred from the total loss of ocean heat is only 20-60% more than the observed basal sea ice melt [*Timmermans*, 2015], indicating that the majority of upper ocean heat flux goes into the ice, rather than the atmosphere.

The seasonal entrainment of heat from the NSTM into the surface mixed layer in the Canada Basin is generally presumed to be a result of shear-driven mixing from wind and ice motion [*Jackson et al.*, 2012]. Strong wind or rapidly drifting ice causes relative motion between the surface mixed layer and NSTM, which results in mixing at the summer halocline. Although shear-driven mixing generally dominates, convective mixing due to salt plumes can occur under low ice-ocean relative velocities [*Barthélemy et al.*, 2015]. Convective mixing and overturning of the halocline as a result of brine rejection with sea ice growth has been observed by studies in the eastern Arctic Ocean, near Svalbard and Greenland [*Ivanov et al.*, 2016; *Roach et al.*, 1993], where the surface mixed layer in the eastern Arctic Ocean is on the order of 100 m deep with weak stratification (approximately 1 psu). However, the characteristic temperature and salinity profiles in the Canada Basin have comparatively shallow, strongly stratified surface waters that further reduce the likelihood of convective mixing [*McLaughlin et al.*, 2011]. Even with rapid ice formation throughout autumn in the

Beaufort Sea, mixing at the summer halocline and entrainment of heat from the NSTM is likely to result from high-wind events rather than brine rejection [*Yang et al.*, 2004]. In fact, it has been suggested that autumn storms, of increasing cyclonic intensity [*Simmonds and Keay*, 2009], are playing a significant role in the delay of ice edge advance via the release of upper ocean heat.

Although several previous studies have observed ocean mixing events causing sea ice melt under thick, multi-year ice floes, there are few prior observations of ocean-ice coupling under the thin ice that forms during autumn ice advance. As Arctic multi-year ice continues to decline, processes associated with new and first-year ice are becoming more important to the overall Arctic system. This study will use observations of a high-wind event over five days in the Beaufort Sea area of the Canada Basin to show how ocean heat can melt the thin, newly-formed sea ice. First, we will describe the high-resolution measurements made from both ship transects and drifting buoys. Then, we will examine key terms in heat and salt budgets controlling sea ice melt and the temporary reversal of the autumn ice advance. In the discussion, we will explore how the net impact of this autumn event compares to ocean heat loss events previously observed beneath Arctic sea ice. Specifically, we will speculate how the thinner ice and the presence of large surface waves may enhance mixing and ocean heat flux, relative to prior results under thick multi-year ice floes in the absence of surface waves.

3.2 Observational Methods

A high-wind event was observed 10-14 October 2015 over the northern Beaufort Sea, in the deep Canada Basin, north of Alaska (Figure 3.1). Measurements were made from the *R/V Sikuliaq* as part of the Sea State Departmental Research Initiative (DRI) field campaign in the Beaufort-Chukchi seas, from 01 October to 10 November 2015. Data acquisition during the entire cruise is described in the cruise report [*Thomson et al.*, 2015] and in an overview paper [*Thomson et al.*, 2018].

At the start of the event, on 10 October 2015, the ship arrived at the ice edge after

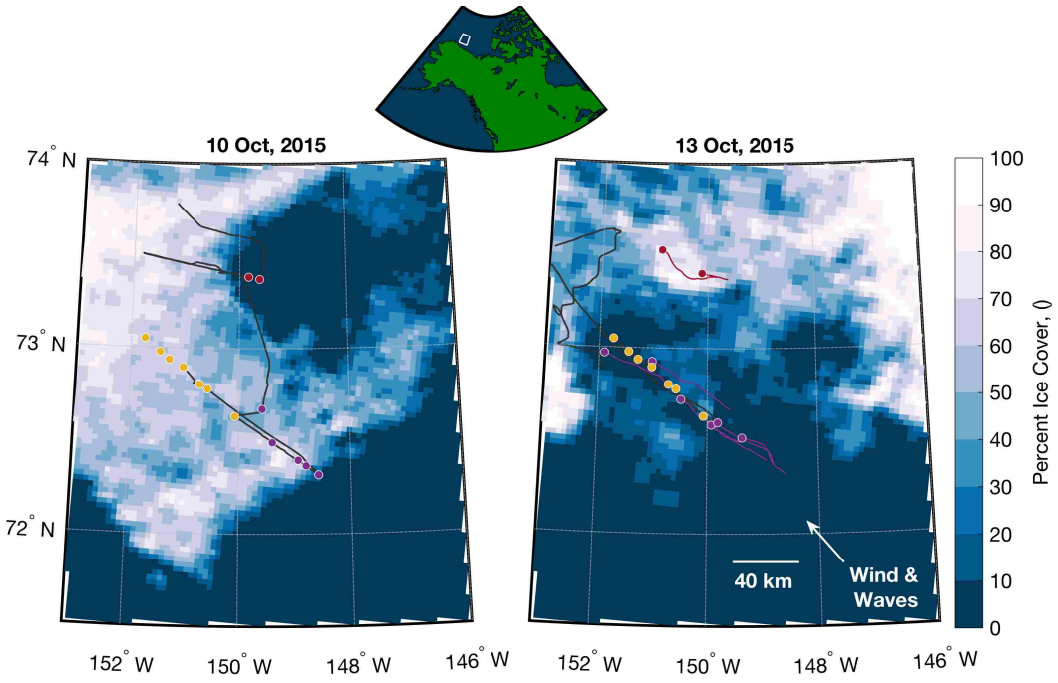

Figure 3.1: Ice concentration and measurement locations in the study area on 10 October 2015 (left), and 13 October 2015 (right). Sea ice concentrations are from 3.125-km daily AMSR2 satellite measurements [*Spreen et al.*, 2008]. Map inset at top shows location of study area. Initial measurement locations are shown on the left with the ship track (black line) from 10-11 Oct. Final measurement locations are shown on the right with the ship track from 12-14 Oct. The seven Eulerian locations, shown by gold dots, are (by definition) the same prior to and after the event. The main array of SWIFT buoys used for this analysis are shown by the six purple dots at the initial (left panel) and final (right panel) locations, with the intervening drift tracks shown by thin purple lines in the right panel. (Note a sixth SWIFT buoy location in the left panel is hidden behind a gold dot, third from right.) The two northern SWIFT buoys (indicated by red dots) will be revisited in the discussion. Buoy drift tracks are generally to the northwest during the event, in agreement with the wave direction and slightly to the right of the wind direction, with an average drift distance of 40 km to the northwest over the three days. The prevailing wind direction was 20-30° to the left (west) of the drift direction.

transiting through over 100 km of newly-formed pancake ice that characterized the initial ice cover. The extent of this pancake ice was remarkable, given the general rarity of pancake and granular ice formation previously observed in the Arctic [*Eicken et al.*, 1995], and was evidence that surface wave forcing had occurred prior to our arrival. During the 4-day storm, a ship-based survey was conducted along a ∼100 km transect normal to the ice edge and parallel to the surface drift direction, within and just outside the changing ice cover. Measurements from the ship characterized the evolution of the atmosphere, ice, and upper ocean heat and salt during the event. Additionally, surface-following buoys (SWIFTs) were deployed to measure surface winds, waves, currents, temperature, and salinity; these generally drifted to the northwest. Figure 3.1 shows the initial (Oct 10) and final (Oct 13) ice concentrations, overlaid with the buoy positions, the axis of the drift, and several repeat stations from the ship's track. We first describe the measurements made from the ship, and then describe the measurements made by SWIFT buoys. Measurement platforms and associated variables are summarized in Table 3.1. These measurements allow us to assess changes in ocean heat content, particularly in relation to changes in ice cover. This is accomplished by combining ship-based and buoy observations, as the buoys drifted with the ice in a surface-Lagrangian reference frame [*Lund et al.*, 2018], while the ship repeated stations in an Eulerian reference frame. Comparing the two reference frames allows for estimation of horizontal advection effects, and assessment of the space-time variability over the domain.

3.2.1 Ship-based measurements

Atmosphere observations

Atmospheric forcing during the event is characterized using bulk meteorological observations and turbulent flux measurements by a suite of instruments installed on the ship's mast. The measurements will be only briefly summarized here, with full descriptions of the instruments and data processing methods available in *Persson et al.* [2018a].

Table 3.1: Summary of variables and observational methods from ship-based and drifting buoy (SWIFT) platforms.

Type	Variables	Method
Ship-based (Eulerian)		
Surface	Wind speed & direction	Metek 3D
	Significant wave height	Reigl Lidar
Upper ocean	Temperature & salinity	OceanSciences uCTD
Sea Ice	Sea ice concentration, thickness, & type	ASSIST visual protocol [*Worby*, 1999b]
Drifting SWIFTs (Lagrangian)		
Surface	Wind speed & direction	Airmar PB200 sonic anemometer
	Wave spectra, height, period, & direction	Microstrain 3DM-GX3-35
Upper ocean	Temperature and salinity (0.5 m)	Aanderra CT
Calculated		
Surface	Net atmospheric heat flux (F_{atm})	see *Persson et al.* [2018a]
Upper ocean	Heat content (HC)	integrated uCTD profiles (Eq. 3.1)
	Salt content (SC)	integrated uCTD profiles (Eq. 3.2)

Wind speed (U_{10}) and direction were measured from heated Metek 3D ultrasonic anemometers sampling at 10 Hz installed at two heights on the ship's bow. Net atmospheric heat flux (F_{atm}) is a combination of radiative, sensible, and latent heat fluxes; a complete time series is obtained from a combination of shipboard measurements and derived calculations [*Persson*, 2012b; *Persson et al.*, 2018a]. Evaporation at the surface is calculated using shipboard measurements of latent heat flux as $E = \frac{LHF}{L_f \rho}$, where L_f is latent heat of fusion of seawater and ρ is the density. Latent heat flux (LHF) is measured using a Licor 7500 at 10 Hz [*Persson et al.*, 2018a]. Scanning and fixed-point laser rangefinders (Riegl) were installed at the top of the tower for continuous underway measurements of significant wave height [*Collins III et al.*, 2017].

Upper ocean observations

Eulerian changes of the upper ocean are examined using temperature (T) and salinity (S) profiles from an OceanSciences underway CTD (uCTD). The uCTD was deployed off the stern of the ship while moving at speeds of 0.5-3 m/s approximately once hourly, as ice conditions and ship speed allowed. Vertical profiles were generally acquired over 5 to 150 m depth; the top 5 m of data are excluded to eliminate contamination from the ship's wake. Data have been processed to correct for the different lagged responses of temperature and conductivity sensors with a variable fall rate, including recomputing salinity from the lag-corrected temperature and conductivity values [e.g., *Ullman and Hebert*, 2014].

The mixed layer depth (MLD) is identified for uCTD profiles. There have been a variety of different methods used in the literature for determining the MLD. Here, we identify the MLD as the shallowest depth at which potential density is more than 0.1 kg m^{-3} greater than the near-surface mean potential density. This method was selected by *Peralta-Ferriz and Woodgate* [2015], who reviewed Arctic Ocean mixed layer properties and determined that this method agreed well with visual assessments of MLD. Near-surface mean potential density is calculated as the average over the upper 10 m to account for noisy near-surface density profiles, and is calculated here from 5 to 10 m to avoid bias from the ship's wake.

Density is used instead of temperature in the Arctic Ocean, as the salinity has a strong impact on density [*Steele et al.*, 2011]. The temperature maximum below the MLD is identified as the near-surface temperature maximum (NSTM) following the definition in *Jackson et al.* [2010]. The temperature minimum below the NSTM is identified as remnant winter mixed layer [rWML *Jackson et al.*, 2011]. Below this is another temperature maximum in the Pacific Summer Water (PSW) layer.

Sea ice observations

Sea ice cover characteristics were recorded hourly from visual observations made from the bridge, including the average sea ice concentration, thickness, and type within 0.5 nautical mile of the ship. At night, observations were aided by use of the ship's flood lights. Observations were made following the ASSIST protocol, which provides a standardized way to make and record sea ice observations in the Arctic Ocean, and is based on the ASPeCT protocol developed for the Southern Ocean [*Worby*, 1999b]. Such visual estimates have been shown to be reasonably accurate, with error of approximately 30% for ice thickness less than 30 cm and approximately 10% for ice concentration [*Worby et al.*, 2008]. Ice thickness estimates are validated with physical samples collected hourly using a dip net over the side of the ship and measured on deck [*Wadhams et al.*, 2018]. Ice concentration estimates are validated with images collected from SWIFT buoys every 4 s (effective during daylight hours only) whenever spatially and temporally collocated (see Section 3.2.4).

An effective ice thickness, ice_{obs}, is calculated as $ice_{obs} = IC_{obs} \times z_{ice}$, where z_{ice} is the visually estimated ice thickness and IC_{obs} is the visually estimated ice concentration. Change in effective ice thickness at a location, Δice_{obs}, is calculated as the difference in initial and final observed concentrations multiplied by ice thickness.

3.2.2 Drifting buoy observations

Lagrangian observations of surface winds, waves, temperature, and salinity were made using version 3 (v3) Surface Wave Instrument Floats with Tracking (SWIFTs). SWIFTs are

freely-drifting buoys originally designed to measure surface turbulence [*Thomson*, 2012]. Observations occur in eight-minute bursts of raw data collection five times an hour, and are post-processed into half-hour intervals for bulk statistical quantities.

SWIFTs have a draft of 1.2 m and thus drift with the surface currents. *Lund et al.* [2018] show that SWIFT drift velocities are within 1 to 2% of ice drift velocities, resulting in less than a half kilometer difference in distance traveled over the approximately four day deployment. As the spatial scales considered here are on the scale of tens of kilometers, SWIFT measurements are considered to be in an ice-following reference frame.

The main buoy array consisted of six buoys that drifted along a transect approximately aligned perpendicular to the waves and ∼20-30° to the right of the wind direction from 72.3°N 148.5°W to 73.0°N 152.6°W. The deployments spanned from early on 11 October to late on 13 October, with initial (deployed) and final (retrieved) locations shown by purple dots in Figure 3.1. All buoys drifted to the northwest during the event. Two buoys were deployed on 10 October at approximately 73.4°N 150.0°W, to the north of the main observation area; these are colored red in Figure 3.1. These drifted in the same direction as the other six SWIFT buoys and parallel to the Eulerian ship track points (with drift tracks shown as thin colored lines in right panel), but are located ∼65 km north of the main array. Note that the ice concentration surrounding these two northern buoys actually increased from 10 October to 13 October, in contrast to the other six buoys (Table 3.2). These buoys will not be used in the analysis of this event, but will be revisited in the Discussion (see Table 3.2). The main array buoys were deployed in order to span the initial ice conditions from open water to thick pancake ice, while northern SWIFT buoys were within an open embayment that subsequently became ice-covered.

Measurements of local wind speed and direction are made from an Airmar PB200 ultrasonic anemometer on the mast of each SWIFT, one meter above the ocean surface. Ice buildup on the sensors occasionally results in spurious wind measurements (identifiable by high variance), and these values are removed in post-processing. Surface wind speeds (U_1) are corrected to ten meters above surface by $U_{10} = 1.19U_1$, as the bulk estimates of u_* and

Table 3.2: Comparison of forcings for main array and northern SWIFT buoys.

	Main array		North buoys	
U_{10} [m/s]	10-18		10-15	
H_s [m]	2-5		1-3	
	initial	final	initial	final
Ice_{obs} [cm]	4	1	1	4
Ocean HC [MJ/m^2]	20	9	35	?

R_{ib} suggest that a multiplicative factor of 1.14-1.23 is appropriate for the atmospheric conditions observed [*Sellers*, 1974]. Each buoy also acquires images of the ocean surface from the mast every 4 seconds using a uCAM serial camera. Images are useful for observing local ice conditions [e.g., *Rogers et al.*, 2016], although temporal coverage is severely limited by daylight and formation of ice on camera lenses. Water temperature and salinity are measured 0.5 m below the surface using an AADI Aanderaa Conductivity Sensor (model 4319).

Measurements of horizontal wave orbital displacements from a surface-following buoy can be used to infer the wave spectra based on linear wave theory, where it is assumed that wave orbitals are circular [*Herbers et al.*, 2012b]. Horizontal displacements are made by the SWIFT using a Microstrain 3DM-GX3-35 combination GPS receiver and Inertial Motion Unit (IMU). Wave orbital velocity components are measured with a horizontal precision of 0.05 m/s, which is sufficient to capture orbitals of most ocean waves (as most orbital velocities are on the order of meters per second), and at a frequency of 4 Hz. Spectral estimates of wave energy are calculated by applying a Fast Fourier Transform (FFT) with 4 windows with 75% overlap, then ensemble averaging [e.g., *Forristall*, 1981]. Further details on wave measurements from this platform can be found in *Thomson* [2012].

Bulk wave parameters are used to give a general characterization of the wave conditions, and are calculated from wave energy spectra as follows. Significant wave height describes the surface elevation associated with the wave field, and is defined as $H_s = 4\sqrt{m_0}$ - four times

the square root of the zeroth moment of the wave spectra (i.e., the total variance). Wave period (T_p) is defined as inverse of the energy-weighted frequency (f_e), $f_e = \frac{\sum E_f}{m_0}$. Peak wave direction describes the direction of wave propagation, and is determined as the maximum in the wave directional distribution, calculated from directional moments using the maximum entropy method [*Lygre and Krogstad*, 1986].

3.2.3 Heat and salt budgets

The heat and salt content of the upper ocean is expected to change over the course of the event as a result of the formation or loss of sea ice, and exchange with the stratified layers below and the atmosphere above. Observed one-dimensional changes in heat and salt content of an ocean layer are defined as ΔHC and ΔSC, and can be estimated by integration of upper ocean profiles as

$$\Delta HC = \Delta \int_h^0 \rho\, c_p\, (T(z) - T_{fr})\, dz = c_p \Big(\rho_{final} \int_h^0 (T_{final}(z) - T_{fr}) - \rho_0 \int_h^0 (T_0(z) - T_{fr}) \Big) \tag{3.1}$$

$$\Delta SC = \Delta \int_h^0 \rho(S - \bar{S}_{ML}) dz = \rho_{final} \int_h^0 (S_{final}(z) - \bar{S}_{ML}) - \rho_0 \int_h^0 (S_0(z) - \bar{S}_{ML}) \tag{3.2}$$

where c_p is the volumetric heat capacity of water, ρ is the average potential density, $T(z)$ and $S(z)$ are measured uCTD temperature and salinity profiles, and subscript 0 indicates the initial profile. Observed changes are calculated over the upper ocean to the depth h of the 1022 kg/m^3 isopycnal, which is generally below the final MLD. The choice of this integration depth is explored in Section 3.3.4. Change in heat content is calculated using the temperature relative to the freezing temperature, T_{fr}, the latter determined using observed salinity. Similarly, change in salt content is calculated using the salinity relative to the average salinity in the initial mixed layer, $\bar{S}_{ML}$, where MLD is defined as the shallowest depth at which potential density is 0.1 kg/m^3 greater than the near-surface potential density. This is necessary to account for vertical motion resulting in thickening of the mixed layer (as with inertial pumping).

One-dimensional heat and salt budgets are used to understand fluxes in the upper ocean during the event and, in particular, the relationship with changes in amount of sea ice cover. Full heat and salt budgets consider all mechanisms for changing heat or salt in a volume of water. The surface mixed layer heat budget proposed in *Cronin et al.* [2013] for use in the subtropical Pacific Ocean is adapted for use here, similar to that used in the eastern Arctic in *Polyakov et al.* [2013]:

$$\Delta HC = \Delta t\Big(\underbrace{F_{atm} - F_{ice}}_{\text{1: heat fluxes}} - \underbrace{\rho C_p h \bar{u} \cdot \nabla_H \bar{T}}_{\text{2: horizontal advection}} - \underbrace{\rho C_p \overline{w'T'}|_{z=h}}_{\text{3: turbulent flux}} \Big) \tag{3.3}$$

Term 1 on the RHS includes the atmospheric heat fluxes into/out of the ocean surface (F_{atm}), and the heat fluxes corresponding to the formation or loss of sea ice (F_{ice}). Term 2 represents horizontal (lateral) advection due to average horizontal velocity ($\bar{u}$) over horizontal gradients in the temperature profiles ($\nabla_H T$). Term 3 is the turbulent flux, alternatively referred to as diffusive mixing, which transports heat vertically. Estimation of these terms will be discussed further in the Results section. This heat budget differs from that used by *Cronin et al.* [2013] and *Polyakov et al.* [2013] in the inclusion of the heat flux to/from ice [i.e. *Timmermans*, 2015], and the exclusion of a vertical advection term. When constraining the heat budget to an isopycnal below the mixed layer, the vertical advection term (which would otherwise be large) becomes unnecessary.

The salt budget proposed in *Cronin et al.* [2015] is adapted for use here as

$$\Delta SC = \underbrace{\Delta t \rho (E-P) S_0}_{\text{1: evap. \& precip}} - \underbrace{\rho_{ice} S_{ice} \Delta ice_{obs}}_{\text{2: ice source/sink}} - \underbrace{\Delta t \rho h \bar{u} \cdot \nabla \bar{S}}_{\text{3: horizontal advection}} - \underbrace{\Delta t \rho \overline{w'S'}|_{z=h}}_{\text{4: turbulent flux}} \tag{3.4}$$

where term 1 represents evaporation and precipitation at the surface (E and P), with S_0 being the salinity at the surface. Term 2 is the change in salinity due to ice growth or melt, and is based on the salinity of the ice (S_{ice}) and the change in effective thickness of the ice (ice_{obs}). Terms 3 and 4 represent the processes of horizontal advection and turbulent fluxes, respectively (as described for the heat budget). As with the heat budget, the primary difference between this salt budget and that used in *Cronin et al.* [2015] is the inclusion

of salinity changes associated with growth or melt of sea ice (Term 2) and the exclusion of vertical advection justified by constraining the budget to an isopycnal.

Budgets are applied over the upper ocean from the surface down to the 1022 kg/m^3 isopycnal. Use of alternative depths h, as discussed in Section 3.3.4, changes the balance of terms in the heat and salt budgets, but does not significantly change the conclusions.

3.2.4 Reference frames

Heat and salt budgets are calculated for both Eulerian (fixed stations revisited by the ship) and Lagrangian (SWIFT buoys drifting with the ice) reference frames. Variables required to calculate these budgets for both reference frames are net atmospheric heat fluxes, evaporation and precipitation, change in effective ice thickness, and upper ocean heat and salt content. For the Eulerian reference frame, all measurements were measured aboard the ship. For the Lagrangian reference frame, variables not directly measured by the SWIFT buoy are estimated by collocating ship-based measurements with locations of each drifting buoy time series.

The ship-board measurements are collocated with SWIFT buoy time series' whenever ship and buoys were within 20 km and 3 hours. These cutoffs where chosen to be as restrictive as possible while still allowing a corresponding initial and final uCTD profile to be identified for each SWIFT buoy. This allows the ship-board measurements to be interpreted in an ice-following (Lagrangian) reference frame, and in particular to obtain initial and final uCTD profiles giving change in upper ocean heat content (ΔHC) and salt content (ΔSC) along a SWIFT drift track. While it should be noted that the 20 km threshold may represent a large spatial gradient of the observed ice and ocean conditions, the distance between initial and final uCTD profiles collocated with SWIFTs is no more than 10 km different from the distance between initial and final SWIFT locations over the same period. In this way, SWIFTs are providing a translation distance in order to be considered Lagrangian and in an ice-following reference frame. Additionally, the gradients within a 20 km spacing were observed to be less than the gradients observed between initial and final locations, which

were generally between 40 and 80 km apart.

3.3 Results

3.3.1 Atmospheric forcing

The sea-level pressure analysis from the European Center for Medium Range Weather Forecasting showed a strong pressure gradient between a high pressure center over the ice to the northeast of the study area and a weak, disorganized, transient area of low pressure over northern and central Alaska [e.g., see Fig. 7b in *Persson et al.*, 2018a]. There was no distinct frontal passage, nor well-developed cyclone with this strong wind event; the minimum sea-level pressure measured by the ship was 999 mb near 12 Oct 14 UTC.

Strong surface winds were observed from 11-14 Oct over the approximately 100 km x 100 km study area. Observed winds 16.5 m above the ocean surface were generally over 10 m/s, reaching a maximum of nearly 18 m/s, and were associated with a complex, bimodal low-level atmospheric jet structure, with one maximum ($\sim$19 m/s) centered near 300 m and the other ($\sim$18 m/s) near the top of the atmospheric mixed-layer at 900 m height [e.g., see Fig. 2 in *Guest et al.*, 2018]. Winds decreased above this height, such that strong winds were only observed in the lowest 2 km of the troposphere throughout the entire event.

3.3.2 Upper ocean evolution

The local evolution of the event, as observed in the Eulerian frame, is shown in Figure 3.2. Winds started increasing on 10 Oct and reached a maximum intensity along the ship track of 17 m s^{-1} early on 12 Oct (Figure 3.2a; black line). A long fetch of open ocean ($\sim$ 400 km) extended to the E and SE of the measurement area, to the Alaskan coastline (see inset in Figure 3.1), allowing the strong winds to produce increasing wave heights starting near 11 Oct 00 UTC and reaching a maximum wave height estimated by Lidar of nearly 5 m from midday 11 Oct through 12 Oct (Fig. 3.2a; gold line). The wave evolution generally followed the wind speed, with maximum wave heights of 4-5 m and wave periods of 8.6 s (not

shown) coinciding with maximum winds. Atmospheric heat fluxes were negative throughout the event, where negative fluxes indicate loss of heat from the ocean surface, and averaged about -90 W m^{-2} after midday 11 Oct (Fig. 3.2b). The early portion of the storm had large heat losses stronger than -230 W m^{-2} due to a large nighttime sensible heat flux, while the daytime heat losses during the event ($\sim$ hours 18 UTC-02 UTC) were smaller (-50 to -5 W m^{-2}).

Despite negative surface heat fluxes to the atmosphere, observed effective ice thickness decreased from 5-10 cm to 0-7 cm at the seven Eulerian stations that were revisited by the ship (Fig. 3.2c; black points). Simultaneously, the upper ocean heat content (HC) calculated following Eq. 3.1 decreased from 17-33 MJ/m^2 to 4-18 MJ/m^2 (Fig. 3.2c; gold points). The time-depth temperature field along the ship track (Fig. 3.2d) shows this to be a result of cooling of the mixed layer, where the MLD and 1022 kg/m^3 isopycnal are identified by thick and thin black lines, respectively. Convergence of the MLD and 1022 kg/m^3 over time indicate entrainment of the top of the NSTM. Even after entrainment of heat from the NSTM to the mixed layer, heat was lost at the surface. The overall implication is that the ocean lost heat to both the ice (which melted as a result) and to the atmosphere.

SWIFT buoys drifting with the sea ice during the event [*Lund et al.*, 2018] provide observations of the upper ocean in the Lagrangian reference frame, as shown in Figure 3.3. Wind speed measured by SWIFT buoys peaked at 17-20 m/s on the 12th (Figure 3.3a; black lines), and are comparable to those measured from the ship (Figure 3.2a) but with more spatial variability. The wind direction was initially from 95° E, and veered slightly southerly to 120° by early Oct 13 (not shown). The buoys drifted 20-30° to the right of the wind; hence, the buoy drift tracks and ship line were oriented approximately ESE-WNW (Fig. 3.1). The variation in wind speed and wave heights in the buoy reference frame show that the sea state evolved through both space and time. Spatial gradients in the waves were caused by interactions with the pancake ice, as described by *Rogers et al.* [2016], with a net result of smaller wave heights (Fig. 3.3a; purple lines) and longer wave periods (not shown) farther into the ice.

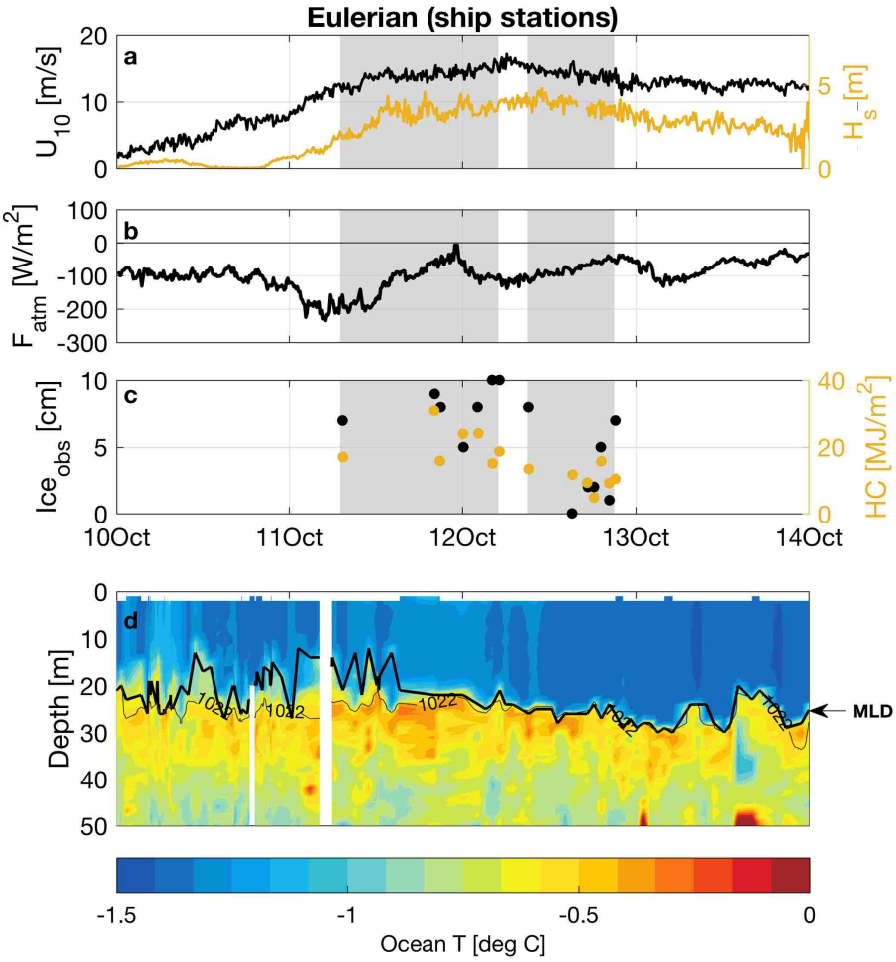

Figure 3.2: Time series for 10-14 Oct 2015 (UTC) of measurements in ship-based reference (Eulerian) frame of (a) ten-meter wind speed (black) and significant wave height (gold), (b) net atmospheric heat flux, (c) effective ice thickness calculated from visual estimates of ice concentration and ice thickness (black) and heat content over the upper ocean (gold), and (d) upper ocean time-depth temperature field. MLD and 1022 kg/m^3 isopycnal are identified on the temperature field as thick and thin black lines, respectively. Effective ice thickness and heat content are shown at Eulerian stations only, while all other variables are shown over the entire ship track. Grey shaded areas identify initial and final measurements used in Eulerian heat and salt budgets.

The sea ice and upper ocean are expected to move approximately with drifting buoys in the Lagrangian reference frame. As in the Eulerian reference frame, negative net atmospheric heat fluxes indicate that heat is being lost from the ocean surface to the atmosphere (Figure 3.3b). Yet, sea ice effective thickness decreases from 0.8-4.2 cm to 0-1.5 cm (black points in Fig. 3.3c). The observed decrease in ice is associated with a substantial decline in upper ocean heat content (purple points in Fig. 3.3c). By the time the buoys are recovered, the mixed layer is nearly uniformly at the freezing temperature (Figure 3.3d). Again, the implication is that the ocean lost heat to both the ice (which melted as a result) and to the atmosphere.

In both Lagrangian and Eulerian reference frames, pairs of initial and final temperature at all measurement locations show a loss of heat from the upper ocean (Figure 3.4). Heat is removed from the mixed layer, such that final mixed layers are nearly uniformly at the freezing point. Some erosion of heat from the NSTM is observed. Pairs of initial and final salinity profiles in Lagrangian and Eulerian reference frames show that the mixed layer undergoes slight freshening, especially in the Lagrangian reference frame, due to freshwater input from sea ice melt. Offset of the 1022 kg/m^3 isopycnal between initial and final profiles (grey and black points) is believed to primarily result from downwards vertical advection of the upper ocean. Vertical advection likely results from inertial pumping, which is defined as upwelling or downwelling at or near the inertial period as a result of divergence in the surface velocity field. Divergence in surface velocities may result from a spatial gradient in sea ice and associated wind stress [*Khandekar*, 1980]. The observed horizontal convergence of Lagrangian drifters is consistent with the amount of inertial pumping required to created the vertical offsets observed.

All initial and final upper ocean profiles shown in Figure 3.4 are also plotted as T-S diagrams with water masses identified in Figure 3.5. The T-S diagram corresponding to Lagrangian profiles also includes measurements of temperature and salinity 0.5 m below the surface from the SWIFTs. (These shallow depths are contaminated by the wake of the ship in the uCTD dataset, and thus are only available from the SWIFTs.) T-S diagrams avoid

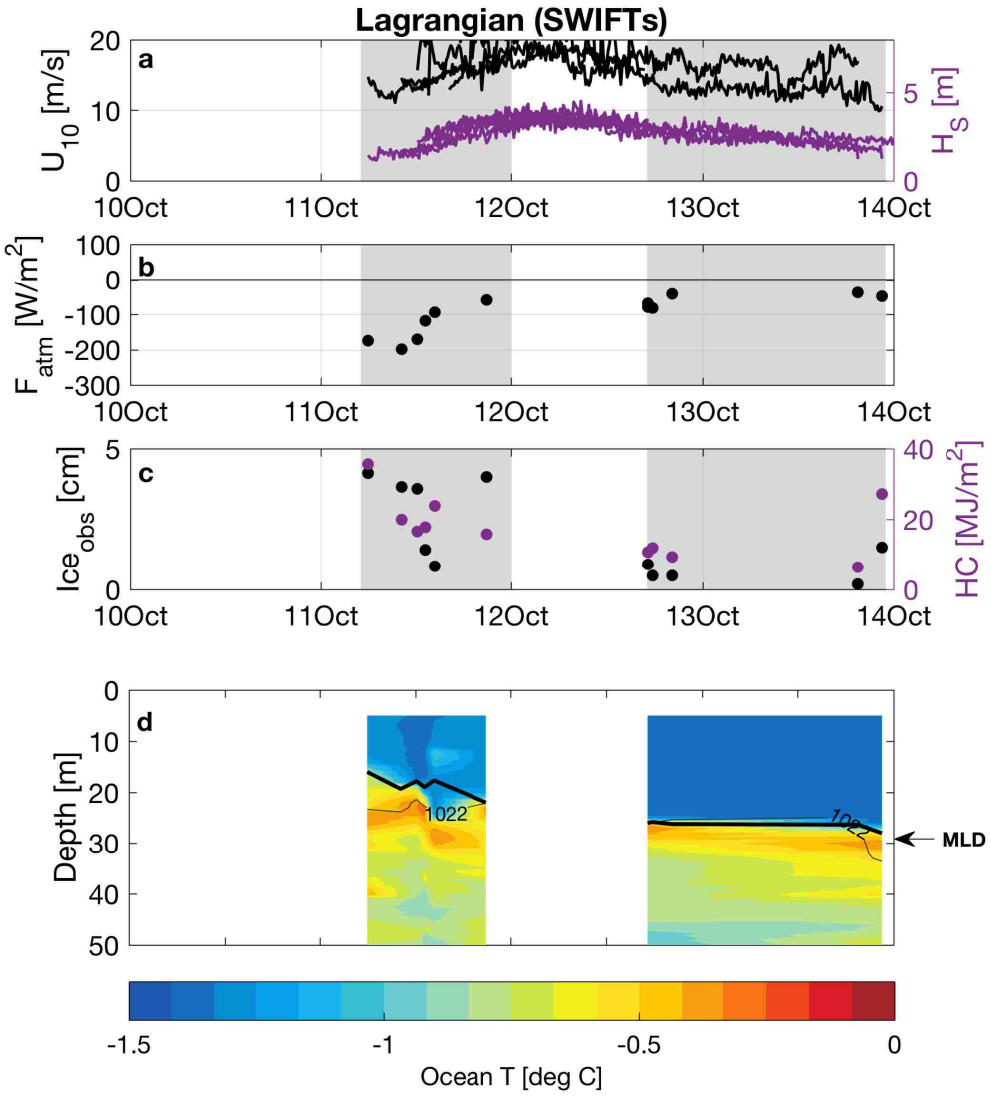

Figure 3.3: Time series from 10-14 Oct 2015 (UTC) in Lagrangian reference frame (main array of SWIFT buoys) of (a) ten-meter wind speed (black) and significant wave height (purple), (b) net atmospheric heat flux, (c) effective ice thickness (black) and heat content (purple) over the upper ocean, and (d) upper ocean time-depth temperature field. MLD and 1022 kg/m^3 isopycnal are identified as thick and thin black lines, respectively. Grey shaded areas identify initial and final measurements used in Lagrangian heat and salt budgets.

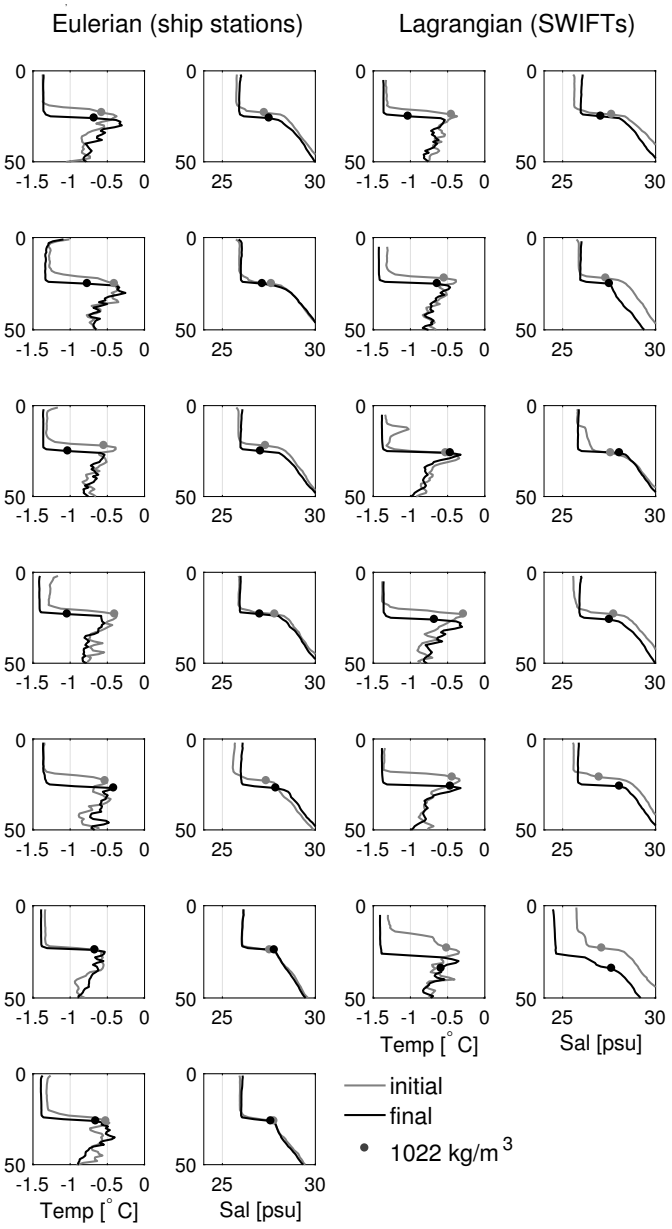

Figure 3.4: Temperature and salinity profiles at initial (grey) and final (black) times for all stations (7 total) and buoys (6 total). Profiles are shown for Eulerian (ship-based) reference frame on the left, and for Lagrangian (SWIFT-following) reference frame on the right. Points mark a density of 1022 kg/m^3, which is the bottom of the upper ocean layer to which budgets are applied.

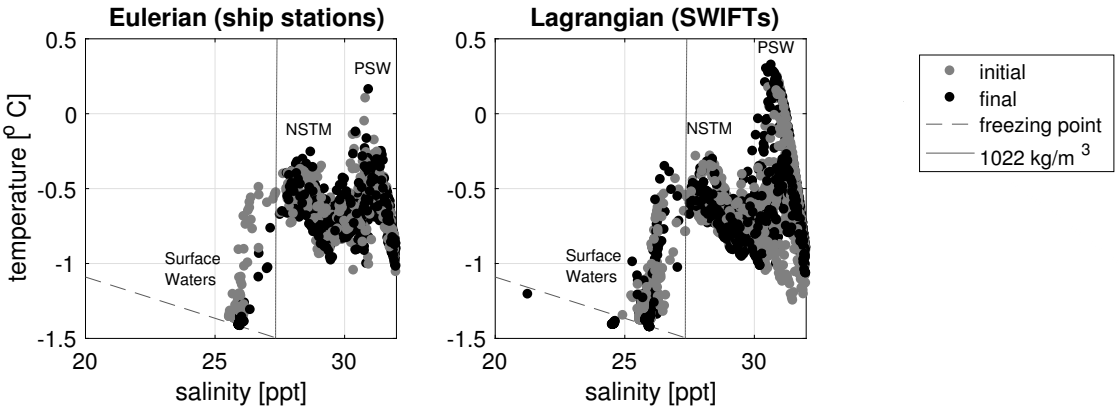

Figure 3.5: Temperature-Salinity diagrams for initial (grey points) and final (black points) measurements, in both Eulerian reference frame (left) and Lagrangian reference frame (right). The depth of measurements increases to the right, from 5 to approximately 80 m, as density is primarily a function of salinity. In the Lagrangian reference frame, SWIFT measurements of temperature and salinity at 0.5 m (below surface) are also included. The dashed line indicates the seawater freezing point at atmospheric surface pressure, and the thin vertical line represents a density of 1022 kg/m^3. Surface waters (within the mixed layer), the near-surface temperature maximum (NSTM) and Pacific Summer Water (PSW) are also identified.

isopycnal displacement problems by plotting temperature as a function of salinity, which sets the density in this area. Measurements in the surface mixed layer are clustered near the freezing point (dashed line), and the NSTM and PSW are identifiable as local temperature maxima. Comparing the initial (grey points) and final (black points) measurements show erosion of the NSTM and a more distinct transition between surface waters (in the mixed layer) and the NSTM below, especially in the Eulerian reference frame. NSTM, PSW and water masses below PSW are spatially variable, evidenced by the spread of points.

3.3.3 Heat and salt budgets

The link between the upper ocean evolution and sea ice melt is evaluated using the heat and salt budgets defined in Eqs. 3.3 and 3.4. Temperature and salinity profiles paired at fixed (Eulerian) and drifting (Lagrangian) locations (see Figure 3.4) are integrated to obtain changes in heat content (ΔHC) and salt content (ΔSC). The overall results are a substantial loss of heat and a negligible or minor salinification. Each of the terms on the right-hand side (RHS) of the budgets in Eqs. 3.3 and 3.4 are calculated and considered in turn. The balance of the changes in upper ocean heat and salt content are summarized in Figure 3.6 (left and right, respectively), with error bars showing the standard deviation from each set of estimates.

Fluxes to the atmosphere (term 1 in the heat and salt budgets; turquoise bar in Figure 3.6) are estimated with measurements following *Persson et al.* [2018a]. The average heat flux out of the ocean surface is estimated for each profile as an average of collocated ship-based net atmospheric heat flux (F_{atm}). Average values are larger in the Lagrangian reference frame than the Eulerian primarily due to the longer time period covered (Δt). Precipitation was observed to be zero for all stations and SWIFTs locations during the event. Average observed evaporation from the surface of $1.3 - 1.5 \times 10^{-4}$ m/s leads to a minor salinity increase at all locations.

Loss of heat due to the loss of sea ice (term 1 in the heat budget and terms 2 in the salt budget; blue bar in Figure 3.6) is calculated with $F_{ice} = \rho L_f \Delta ice_{obs}$ where Δice_{obs} is the change in effective thickness from visual observations. Ice density is estimated to be 938 kg/m^3 following *Weeks and Ackley* [1986] with an assumed brine volume of 36% and bubble fraction of 1%, and latent heat of fusion is estimated to be 215 kJ/kg following *Ono* [1966]. Corresponding changes in observed ice thickness (Δice_{obs}) at the location of each profile are calculated as the change in effective ice thickness; that is, the observed ice concentration multiplied by the average ice thickness observed. Similarly, salinity flux due to the loss of sea ice is calculated based on observed change in effective thickness as given in Eq. 3.4; a

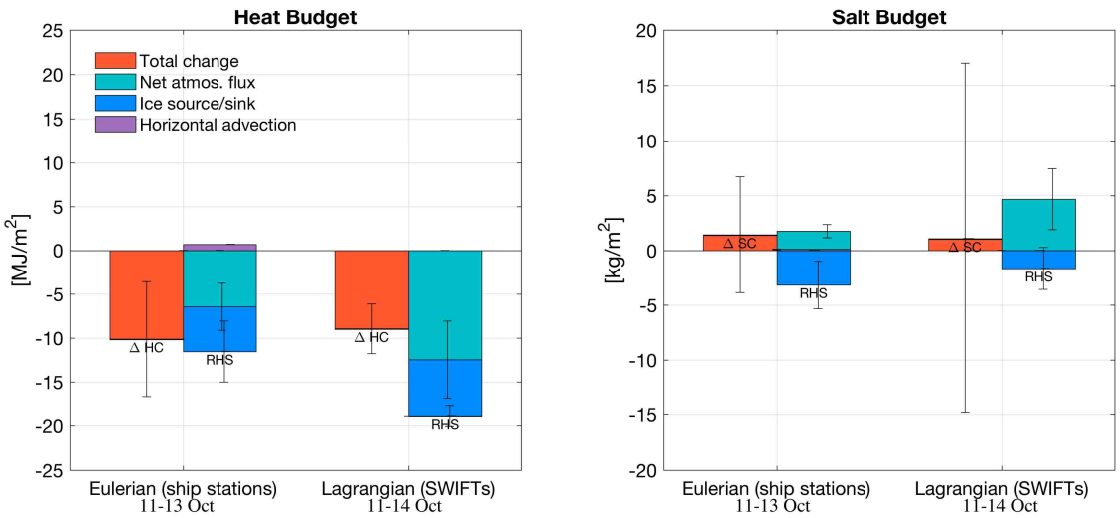

Figure 3.6: Upper ocean heat budget (left) and salt budget (right) for 7 Eulerian ship stations, and 6 Lagrangian SWIFT buoys. For each pair of bars, observed changes in mixed layer heat (ΔHC) and salt content (ΔSC) calculated using collocated uCTD profiles are shown on the left, while estimates of RHS terms - net atmospheric fluxes, ice source/sink, and horizontal advection - are shown on the right (Eqs. 3.3 and 3.4). Negative values represent loss of heat and salt from upper ocean, respectively. Error bars are the standard deviation from each set of estimates. Details describing the terms and their calculations can be found in the Methods and Results sections.

salinity of 6 ppt is used for sea ice (S_{ice}), based on average measurements of ice collected with the dipnet during the event [*Wadhams et al.*, 2018].

Horizontal advection describes the effect of spatial variability in upper ocean structure and sea ice (term 2 in the heat budget and term 3 in the salt budget; purple bars in Figure 3.6), and so may be represented by the difference of the observed changes in Eulerian and Lagrangian reference frames. As the upper ocean moves approximately with the Lagrangian buoys, this provides an estimate of the effect on the Eulerian (fixed) reference frame. Estimates of changes in heat and salt content due to horizontal advection of the upper ocean are calculated as the difference between Eulerian points closest to the final SWIFT locations (4-7) and Eulerian points closest to the initial SWIFT locations (1-3). This difference is scaled by the ratio of temporal coverage of the Eulerian and Lagrangian budgets. The horizontal advection term accounts for a small positive change in heat and salt content in Eulerian reference frame as a result of some spatial variability in initial mixed layer temperature and salinity. Although this estimate neglects much of the spatial and temporal variability of the event, the small value indicates that the role of horizontal advection on the depths being considered is negligible compared to the other terms.

Finally, the turbulent fluxes in the upper ocean (final terms in Eqs. 3.3 and 3.4) are estimated to be negligible. Following *Cronin et al.* [2015], turbulent heat and salt fluxes can be approximated using diffusivity constants κ_T and κ_S as

$$\begin{aligned} \rho C_p \overline{w'T'}|_{z=h} &= -\kappa_T \overline{\frac{\partial T}{\partial z}}\Big|_{z=h} \\ \rho C_p \overline{w'S'}|_{z=h} &= -\kappa_S \overline{\frac{\partial S}{\partial z}}\Big|_{z=h} \end{aligned} \tag{3.5}$$

Jackson et al. [2011] found diffusivity constant of $\kappa_T \approx 3 \times 10^{-6}$ to realistically replicate temperature changes in the near surface waters of the Canada Basin. Estimation of turbulent (diffusive) heat flux using these values gives heat content change on the order of 0.1 MJ/m^2 for this event, approximately two orders of magnitude smaller than the heat content change observed. We therefore assume that the turbulent flux term in the heat and salt budgets is negligible at all the measurement locations.

Overall, the results of the two reference frames are consistent: loss of heat from the upper ocean corresponds to the loss of sea ice at the surface. There was a significant loss of mixed layer heat and erosion of the NSTM over approximately two days that can be mostly accounted for by heat flux into the atmosphere and melting of surface sea ice. Of the total ocean heat lost, approximately 60-70% went into the atmosphere, and 30-40% went into melting sea ice (Fig. 3.6). Thus, the observed changes in heat content are primarily driven by heat fluxes from the ocean to the ice and atmosphere (i.e., $\Delta HC \approx \Delta t(F_{atm} - F_{ice})$). Horizontal variability and turbulent fluxes have small and negligible effects during this event, respectively. The minor change in salt content in both reference frames can be accounted for by the balance of evaporation (increasing salt), and melting ice (freshening).

3.3.4 Budget depths

Using heat and salt budgets (Equations 3 and 4) to understand evolution of the upper ocean requires appropriate choice of depth over which they should be integrated. Though there are a variety of choices of h that seem reasonable to use as the definition of the bottom of the 'upper ocean' based on temperature profiles and prior literature, the correct choice of h is not immediately obvious. Here we will explore a number of possible choices of h and their impacts, ordered by increasing depth:

1. MLD. This is the method used in *Jackson et al.* [2012].

2. Maximum MLD over the time series of each station or buoy (MLD_{max}) such that a single depth results in a constant volume of integration.

3. A constant density isopycnal that is unaffected by mixing; i.e. always below MLD. Here, the $\rho = 1022$ kg/m^3 isopycnal is chosen as it is observed to be below final MLDs.

4. Temperature minimum of the rWML (approximately 40-50 m). This is the method used in *Timmermans* [2015].

We will use the resulting change in heat content ΔHC, the left-hand side term in the heat budget (Eq. 3.3), to understand the implications of each choice of h (Figure 3.7). The results presented in the main body of the paper use the third method. The methods are detailed and compared below.

1. *Jackson et al.* [2012] observed the change in heat content from the surface to the base of the surface mixed layer (MLD) to track diffusion of heat into the mixed layer. This will estimate heat that is lost from the mixed layer into the ice or atmosphere. However, in this study, the observed atmospheric heat flux is greater than the heat content calculated using this method (Figure 3.6), suggesting additional heat lost from below the MLD (Figs. 3.2 and 3.3). Using the MLD as the bottom depth of integration will not capture any heat from the NSTM, which appears to comprise a substantial amount of heat lost from the upper ocean. In fact, the estimates of changes in heat content made using this definition of h are smaller than any others, and even show an increase in heat at some locations as indicated by the error bars.

2. Although it is initially tempting to use a constant depth of integration, such as the maximum MLD over each record, we can see the danger of this choice by examining salinity profiles in the Lagrangian reference frame in Figure 3.4. Over these deployments, there is substantial vertical advection due to inertial pumping of the MLD and isopycnal below. As a result, the change in heat content is drastically over-estimated in the Lagrangian reference frame (nearly twice that estimated in the Eulerian reference frame).

3. Using an h that follows an isopycnal accounts for changes due to vertical advection, and thus avoids the problem in the preceding method. We define h with a constant isopycnal that lies below the depths affected by mixing (i.e. the MLD). Defining a depth that is just below the MLD will allow all heat content changes due to mixing to be included. We observe that the 1022 kg/m^3 isopycnal lies below the MLD (thick line) the majority of the time, and is approximately the depth of the MLD at the final time (Figs. 3.2 and 3.3). The change in heat content using this h is consistent between the two reference frames, and consistent with what we qualitatively observe in the temperature profiles (Figure 3.4).

4. *Timmermans* [2015] use the rWML depth, which is well below the MLD and NSTM, to examine changes in stored solar heat over the annual cycle. In Figures 2 and 3, we can see this temperature minimum is generally around 40-50 during this event. This depth allows the heat budget to include all water masses containing summer solar heat, and is well below the depth that may be effected by entrainment events. However, this choice is problematic for this event in that the near-surface temperature maximum is seen to be quite spatially variable (Figure 3.2), and the Lagrangian buoys will drift with the mixed layer into areas where the NSTM has less initial heat. As a result, this method will result in reasonable estimates of change in heat content for the Eulerian reference frame, but will significantly underestimate change in heat content in the Lagrangian reference frame due to different initial NSTM heat content further north.

In summary, we determine the 1022 kg/m^3 isopycnal to best capture the upper ocean evolution that occurs during this event. Though there are likely other appropriate definitions of h that could be used to describe the upper ocean here, we find that this definition adequately suites our purposes. Whenever h is used throughout the paper, it is defined as the depth at which $\rho = 1022$ kg/m^3.

3.4 Discussion

3.4.1 Comparison to prior studies

Prior studies under thick, multi-year ice in the Canada Basin have also observed upper ocean heat loss that results in sea ice melt. Stored ocean heat is a result of solar input throughout the summer and early autumn that becomes becomes trapped by stratification. Heat can become entrained into the surface mixed layer when mixing erodes the stratification in autumn and winter. *Timmermans* [2015] and *Jackson et al.* [2012] described entrainment of heat from the upper ocean during 2006-2008 and 2007-2008, respectively, and found substantial fluxes of ocean heat to sea ice during high wind events. The event described here has similar mechanisms to these previously described autumn entrainment events. However,

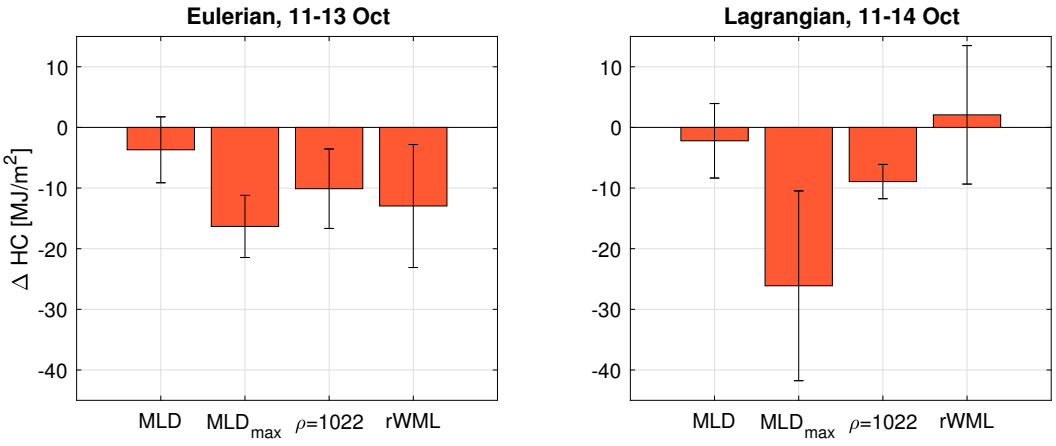

Figure 3.7: Comparison of change in heat content (ΔHC; Eq. 3.1) calculated using four different methods of defining h. Values are compared for the Eulerian reference frame on the left, and Lagrangian reference frame on the right. Error bars are the standard deviation from each set of estimates.

previous studies used measurements from ITPs, which by definition must be deployed on thick ice floes, while the present study used ship-based measurements and ocean buoys to study changes in thin, pancake sea ice. As a result, there are key differences in the surface conditions, the magnitude of the heat fluxes observed, and the outcomes.

Oceanic heat flux from seawater to ice is estimated as the product of heat and turbulence at the ice-ocean interface [*Krishfield and Perovich*, 2005]. Direct measurements of this value are difficult to make, so it is often parametrized using a combination of mixed layer temperature and ice-ocean friction velocity [*McPhee*, 1992] or using sea ice thermistor profiles [*McPhee and Untersteiner*, 1982], both of which are possible using ice mass balance buoys. The former method was used by *Jackson et al.* [2012]. We can alternatively estimate the oceanic heat flux with upper ocean temperature profiles as the change of upper ocean heat content over time ($\Delta HC/\Delta t$), where it is assumed all heat loss is due to upwards oceanic heat flux. Change in upper ocean heat content is calculated by integrating the temperature relative to freezing temperature (Eq. 3.1).

We compare estimates of oceanic heat flux during the October 2015 marginal ice zone event with autumn ocean heat fluxes in 2007 (parametrized using ice-ocean friction velocity from an ITP and autonomous ocean flux buoy [AOFB, *Jackson et al.*, 2012]) and in 2015 but in pack ice (estimated using temperature profiles from four ITPs [*Toole et al.*, 2011] deployed in the Canada Basin between ∼76 and 82°N, i.e., north of the October marginal ice zone observation) (Figure 3.8). The ITP used in *Jackson et al.* [2012] was deployed on approximately 3-m thick ice floe, and the ITPs deployed in 2015 were on ice floes with thicknesses between 1.0-1.9 m. Ice thicknesses during the October marginal ice zone observations, by contrast, were on the order of 0.1 m. Oceanic heat flux for the October observations (gold and purple points, corresponding to Eulerian and Lagrangian as in Fig. 3.1) and ITPs deployed in 2015 (grey lines) are determined as the rate of change of upper ocean heat contents. Corresponding initial and final upper ocean heat contents (HC) are shown in the top panel of Figure 3.8, and are determined as described in Eq. 3.1 but with h defined for ITP profiles as the depth where $\rho = 1023$ kg/m^3, as that was empirically determined to be more consistently at or just below the MLD (see Section 3.3.4). In addition, ITPs don't begin measuring data until about 6 m below the surface so the surface waters, including $\rho = 1022$ kg/m^3, are often not sampled. Heat content values based on the ITP profiles are significantly lower than those in *Timmermans* [2015], due to the shallower depth of integration used here, which generally excludes most of the warm NSTM.

The magnitude of heat content and flux during the October marginal ice zone observations are significantly larger than those observed in the autumn ITP time series. Upper ocean heat content observed throughout the marginal ice zone observations are larger than that observed by the ITP under thicker ice. Observations generally show negative ocean heat fluxes, indicating a loss of heat over time, with values around -100 W/m^2. Heat flux values are more than twice as high as average flux observed by ITPs in the same period. Positive ocean heat flux values are occasionally observed by 2015 ITP profiles, and indicate an increase in heat content estimated for the upper ocean, possibly due to horizontal advection or other terms.

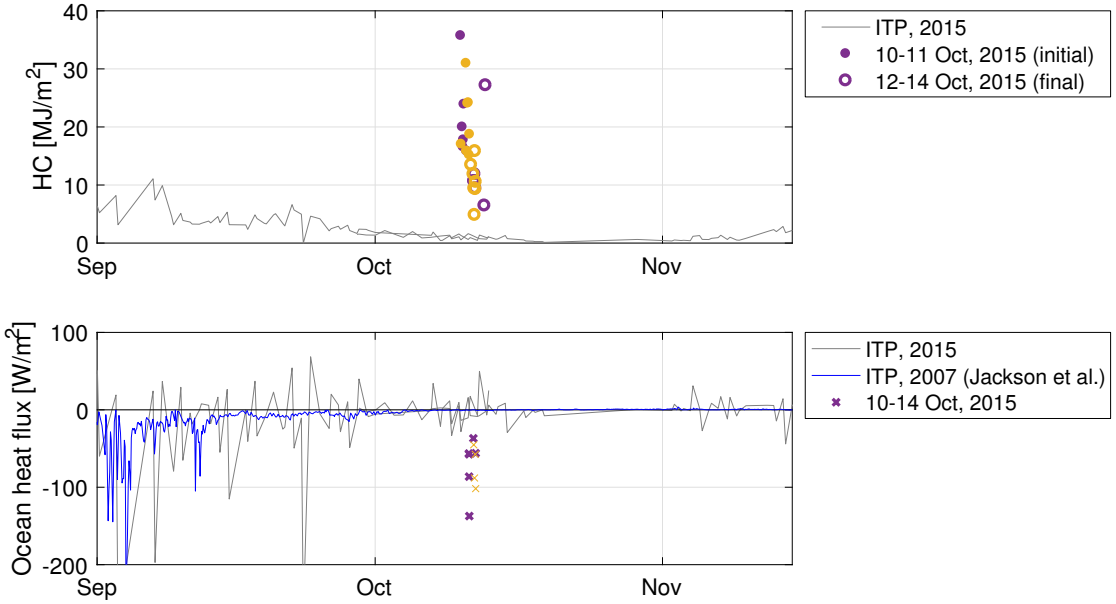

Figure 3.8: Comparison of ocean heat content (HC) and heat flux observed during autumn in the Canada Basin from: four ice-tethered profilers [ITPs *Krishfield et al.*, 2008; *Toole et al.*, 2011] deployed during 2015 (grey lines); an ITP deployed in 2007 [*Jackson et al.*, 2012, blue line]; and in the Eulerian and Lagrangian reference frame in the October 2015 marginal ice zone measurements (gold and purple points, respectively). For October 2015 measurements, closed circles represent initial HC values, open circles represent final HC values, and x's represent oceanic heat flux based on the change between. Heat content is calculated for ITPs deployed in 2015 using h where $\rho = 1023$ kg/m^3. Ocean heat flux was parametrized from the ITP deployed in 2007 following the method of *McPhee* [1992]. Negative values of ocean heat flux indicate that heat is transferred from the ocean to the atmosphere or sea ice.

The thin, new ice at the advancing ice edge is likely to see much larger upper ocean heat entrainment events with strong negative heat fluxes in the autumn. Despite the significantly higher oceanic heat flux, a much smaller portion of the net heat flux is found to go into sea ice melt in thin ice than under thick ice. In Figure 3.6, between 60-70% of the ocean heat flux is directly lost to the atmosphere, with the remainder used to melt pancake ice. In comparison, *Timmermans* [2015] found nearly all of the heat loss was used for basal ice melt (of thicker pack ice), with less than 1/3 accounted for by conductive flux to the atmosphere.

Compared to basal melt of thick ice by oceanic heat entrainment, melt of thin sea ice may have more extreme consequences for future sea ice and snow cover. Loss of thin sea ice during autumn ice advance effectively resets the snow accumulation for the area in question. *Webster et al.* [2014] found that delayed freeze-up in the Canada Basin is strongly correlated with thinner winter snow depth. As snow cover can both influence winter sea ice growth [*Mellor*, 1964] and maintain a higher surface albedo [*Barry*, 1996], the effect of this event may extend through the winter and into the following spring.

3.4.2 Wave effects

The October 2015 marginal ice zone event presented conditions that lie somewhere between the limiting cases of thick, multi-year ice and completely open water. One key difference between these limiting cases and the marginal ice zone is the presence of surface waves in ice, which are generally increasing in the western Arctic [e.g., *Thomson et al.*, 2016b]. At lower latitudes, surface waves are known to enhance mixing of the upper ocean through the generation of Langmuir Turbulence and the shear in the Stokes drift profiles [*D'Asaro et al.*, 2014]. Globally, wave effects may produce mixed layers that are 20% deeper, on average [*D'Asaro et al.*, 2014]. Thus, the presence of waves in the October 2015 marginal ice zone event may have increased the amount of heat released from the upper ocean.

Here, we explore how the conditions in this event compare to the limiting cases of thick ice studies [*Jackson et al.*, 2012; *Timmermans*, 2015] and open water, the latter defined for wind speeds observed during the October 2015 event but without the presence of sea

ice. We include results from the northern two SWIFT buoys (Fig. 3.1), excluded from the analyses up this point, to further distinguish the wave conditions. The two northern buoys experienced smaller waves and an increase in ice rather than a decrease (Table 3.2). Figure 3.9 shows ranges of observed ice draft, wind speeds U_{10}, wave Stokes drift in the surface layer $u_{s,SL}$, and turbulent Langmuir number La^{-2}. Here, surface layer Stokes drift is defined as the average Stokes drift from $z = 0$ to $z = 0.2(MLD)$, as defined in *D'Asaro et al.* [2014]. The Stokes drift is estimated from the observed wave spectra as

$$\mathbf{u}_s(z) = \frac{16\pi^3}{g} \int_0^\infty f^3 \, e^{-kz} \, E(f) \, df, \tag{3.6}$$

where f is frequency, E is energy density, k is wavenumber, and g is gravity. This is calculated for the open water case based on the fully-developed wave spectra of *Pierson and Moskowitz* [1964] using observed wind speeds. For the ITP cases, we simply assume zero waves under thick ice. The Langmuir number, ($La^{-2} = u_{s,SL}/U_{10}$), is then used to compare relative strength of the wave forcing to the wind forcing [e.g., *D'Asaro et al.*, 2014].

The wave forcing ($u_{s,SL}$) decreases significantly across these cases, despite comparable wind forcing (U_{10}). The Langmuir number is scaled by the wind, and thus has a similar signal. The signals are of course tied to the ice, because ice attenuates waves and limits the fetch available for wave generation. This suggests a feedback mechanism, in which ice formation can limit surfaces waves directly, indirectly limiting ocean heat fluxes. In contrast, wave growth may enhance mixing such that ocean heat fluxes are increased relative to pure wind forcing, and thus melting is promoted. Though not presented here, results show that these feedbacks are dependent on the short (high-frequency) surface waves, which are most severely affected by ice and most important in setting the Stokes drift (i.e., the f^3 dependence in Eq. 3.6).

Here, we will apply a nondimensional fetch scaling to interpret the observed wave forcing and provide guidance for future applications in ice-covered oceans. The two buoys to the north measured noticeably smaller waves (Table 3.2) as a result of the fetch-limited conditions in the open water embayment in which the buoys were deployed (Figure 3.1). Under fetch-

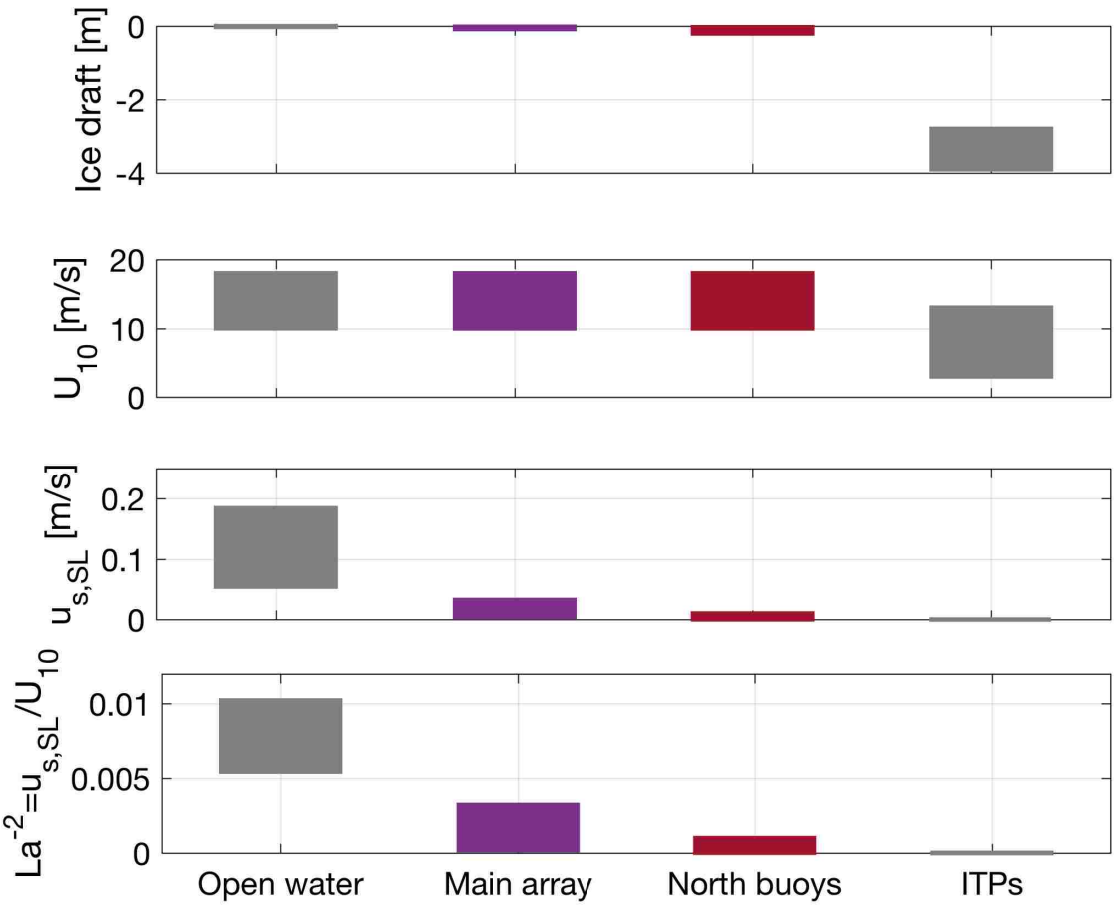

Figure 3.9: Comparison of ice, wind, and wave forcings observed in open water, during the 10-14 Oct event, and under thick ice observed by ITPs [*Jackson et al.*, 2012; *Timmermans*, 2015]. Observations during the 10-14 Oct 2015 event are separated out into the main array and northern SWIFT buoys, in purple and red respectively.

limited conditions, wave height is a function of the fetch distance, such that nondimensional wave energy is directly related to nondimensional fetch [*Young*, 1999]. Nondimensional fetch is defined as

$$\mathcal{X} = \frac{gx}{U^2} \tag{3.7}$$

where g is gravitational acceleration, x is the dimensional fetch distance, and U is wind speed. Approximate dimensional fetch distances to ice or land are calculated as described in *Thomson and Rogers* [2014b]. Nondimensional wave energy (E) is defined as

$$E = \frac{g^2 H_s^2}{16 U^4}. \tag{3.8}$$

where H_s is the significant wave height. Under a constant wind forcing, wave energy (height) will increase exponentially with increasing fetch.

In fact, the waves in this marginal ice zone event do scale by fetch. Figure 3.10 compares the nondimensional fetch and nondimensional energy of waves in the main array and the north pair. Along the main array, wave energy scales with fetch by the relationship $E \sim \mathcal{X}^{1.6}$ (purple points). The wave energy of the northern SWIFT buoys scales with fetch according to $E \sim \mathcal{X}^{0.88}$ (red points). Both relationships fall within the range of exponential values described by conventional open water fetch relationships [*Young*, 1999], which have previously been shown to hold in the Arctic Ocean [*Smith and Thomson*, 2016; *Thomson and Rogers*, 2014b].

However, we see that wave energy at the northern buoys is limited not just by the decreasing fetch distances as the embayment closes up, but also by the presence of ice which limits the 'effective fetch' distance over which waves can grow in partially ice-covered ocean [*Smith and Thomson*, 2016]. The exponential relationship between fetch and energy then has a lower power as a result of partial ice cover at the location of the northern SWIFT buoys. In contrast, as ice along the main array melts and SWIFT buoys drift north, the fetch becomes larger and wave heights continue to grow. As a result, the range of Langmuir numbers is much higher for the main array than for the northern SWIFT buoys (Figure 3.9). This suggests that in the future, specific details of air-ice-ocean interactions and release of

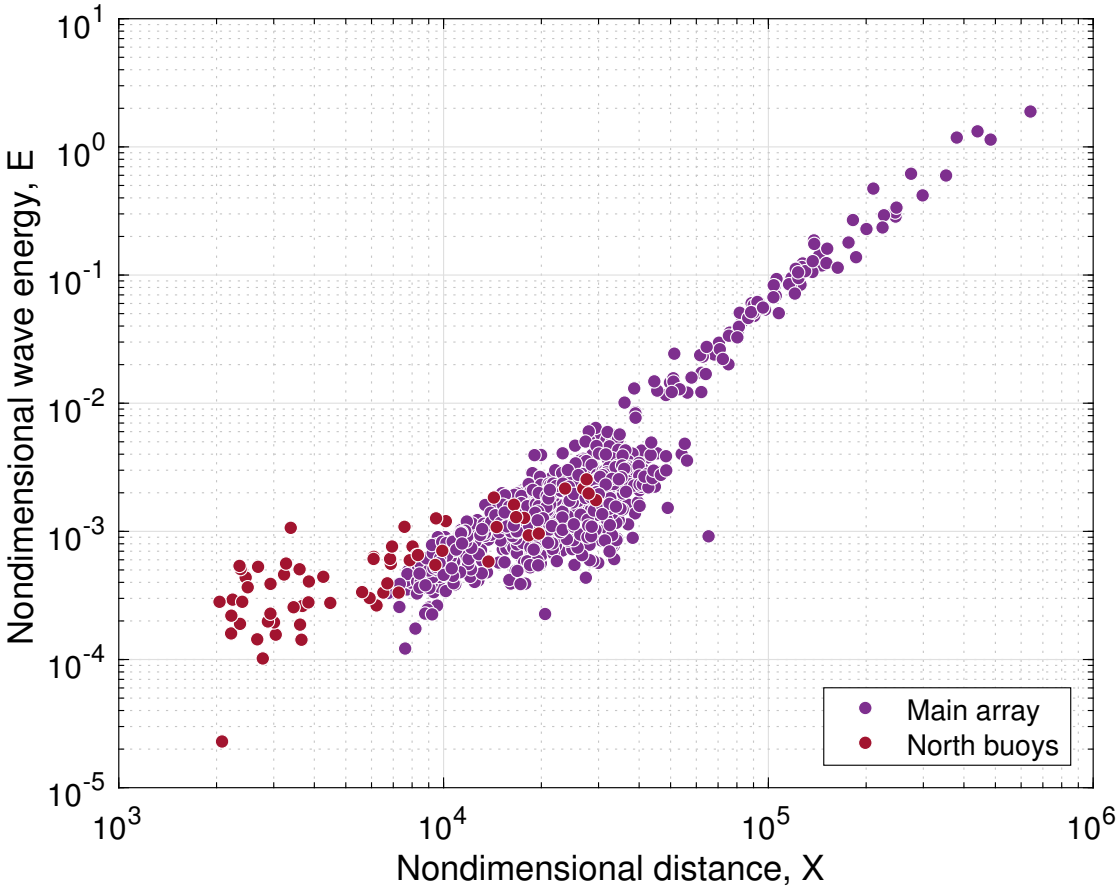

Figure 3.10: Comparison of nondimensional fetch and nondimensional energy from SWIFT buoys in main array (purple) and northern SWIFT buoys (red).

upper ocean heat may be sensitive to effective fetch.

We speculate that the variation in the wave forcing accounts for the variation in the outcome of this event. While initial upper ocean heat content and wind speeds were similar between the northern SWIFTs and the main array, there are strong differences in the evolution of surface waves, and opposing trends in sea ice (Table 3.2). For the northern buoys, ice formation was sufficient to limit the wave growth and associated processes. For the main array, the release of ocean heat was substantial, and ice melt was sufficient to maintain wave growth. The spatial differences may also be a result of ocean pre-conditioning, such as associated with nonlinear ice retreat [e.g., *Steele and Ermold*, 2015], but the observations actually show more initial heat content in the ocean under the north buoys rather thanless. Without observations of the final ocean heat values for the northern SWIFTs, we are unable to determine conclusively whether surface wave forcing, ocean pre-conditioning, or other factors led to the different fates of sea ice at these two locations.

With the expansion of seasonally ice-free area in the western Arctic, increasingly large areas are undergoing autumn freeze-up [*Galley et al.*, 2016]. As thin ice and large open water fetches become more common [*Kwok and Rothrock*, 2009; *Thomson and Rogers*, 2014b], the role of upper ocean heat on delaying ice advance may be greater. It is important for models to be able to capture episodic storm events such as the October 2015 marginal ice zone observations described here. Such events clearly have a rapid impact on sea ice at the operational forecast level. They are additionally important for better estimating the fate of stored upper ocean heat under the winter ice cover, which is a critical parameter in models at the climate and inter-annual level. However, most current operational and research models are not yet up to the task [*Gent et al.*, 2011; *Metzger et al.*, 2014]. In order to fully capture this event, a model would need to predict sufficient wind and waves, entrainment of upper ocean heat, and the rate of heat flux to the sea ice and atmosphere. Though this coupling is beyond current model capabilities, this highlights the importance of high resolution, fully-coupled models for the Arctic. Continuing to advance our understanding of the many ways in which ocean heat contributes to thinning and retreat of Arctic sea ice is essential for future

projections [*Carmack et al.*, 2015].

3.5 Conclusions

Observations of an autumn storm in the Beaufort Sea illustrate how an event can temporarily reverse the seasonal ice edge advance. Prior to the *in situ* observations, pancake ice was formed by surface waves and strong negative atmospheric heat fluxes. As the event progressed, ocean heat was released, and most of the newly formed ice melted. The event was remarkable, relative to climatology, in the magnitude and extent of the ocean heat flux. Furthermore, pancake ice and large surface waves have been only rarely observed in the Canada Basin.

The key observations and results are summarized as follows:

- An autumn high wind event in the Beaufort Sea released a large amount of stored solar heat from the ocean mixed layer and near-surface temperature maximum (NSTM)
- A significant portion of heat released was used to melt thin, new pancake ice that had recently formed as part of the seasonal ice advance
- The rate of ocean heat release is larger than that observed in prior studies under thick Arctic ice, with a much larger fraction accounted for by convective flux to the atmosphere
- The magnitude of heat released and sea ice melted may be related to the changing wave climate in the Arctic Ocean

Although entrainment of upper ocean heat has been observed under multi-year ice in the Canada Basin, the observations presented here indicate that this mechanism can also melt new sea ice and, in fact, control the rate of ice advance in the marginal ice zone, an area that is increasing as the Arctic Ocean transitions to a seasonal sea ice cover [*Meier et al.*, 2014]. Under multi-year ice, rapid ocean heat flux and ice melt occurs primarily in the summer

and early autumn, when solar heat inputs are largest. The magnitude of this event is much larger than events observed in autumn under multi-year ice, and indicates that stored solar heat can have an impact over much more of the year with thinner ice cover.

The magnitude of this event may have been enhanced by the strong wave climate as well as the high winds, both of which are expected to be generally increasing. The average winds associated with Arctic cyclones have been increasing over the last few decades, and so stronger winds may occur more frequently in the future [*Asplin et al.*, 2015; *Serreze et al.*, 2001]. Wave events of this magnitude are rare in the Arctic basin, and only occur at most a few times within a given autumn. However, this probability appears to be increasing [*Thomson et al.*, 2016b]. Attenuation of high frequency waves is a plausible feedback to suppress wave-driven mixing during ice edge advance. Either way, the increasing surface wave climate in the western Arctic is having at least one noticeable affect: the prevalence of pancake ice during ice advance.

Following the storm, the ice re-formed, and the ice edge advanced over this area just a few days later. A few days of reversal in ice edge advance may not seem consequential to the overall seasonal cycle. However, the net thermodynamic ice growth through the autumn and winter may be significantly less as a result of events such as this one. Additionally, delayed autumn freeze-up in the Beaufort region has been found to be strongly correlated with thinner snow cover on sea ice [*Webster et al.*, 2014], which results in a lower surface albedo [*Perovich and Polashenski*, 2012].

Chapter 4

OCEAN SURFACE TURBULENCE IN NEWLY FORMED MARGINAL ICE ZONES

4.1 Introduction

The turbulent kinetic energy dissipation rate at the air-sea interface in ice-covered regions controls exchanges of heat, momentum, and gas transfer. The amount of wind-driven turbulent kinetic energy in the ocean's near-surface region changes as a function of waves, as well as the sea ice cover. Near surface turbulence remains the least constrained in ice-covered regions, which can cover up to 10% of the world's oceans. This is particularly important for improving parametric models for air-sea gas exchange in the marginal ice zone (MIZ), which utilize estimates of turbulent kinetic energy dissipation rates [*Loose et al.*, 2014]. The impact of sea ice on air-sea gas exchange may vary widely, as the presence of sea ice can both enhance exchange by causing stirring and inhibit exchange by serving as a barrier [*Bigdeli et al.*, 2018].

In the MIZ, the flux of momentum from the wind (i.e., the wind stress τ_{wind}) is transmitted to the ocean below via drag on both open water patches and ice floes. It is common to partition the wind stress as

$$\tau_{wind} = (1 - A)\tau_{air-water} + A\tau_{ice-water}, \tag{4.1}$$

where A is fractional areal coverage of sea ice [e.g., *Steele et al.*, 1989; *Yang*, 2006]. The first term represents the stress from the wind on open water patches, and the second term represents the stress from the wind on ice floes. Although a useful framework for many studies, this partitioning of the wind forcing may not be an accurate representation of a marginal ice zone in which the ice floes and open water patches are acting as a continuum on scales much smaller than the turbulent eddies in the atmosphere. Further, this partitioning is unnecessary to determine the total momentum flux to the ocean below (τ_{ocean}) if there is no significant acceleration of floes, such that the momentum flux must be conserved as $\tau_{wind} = \tau_{ocean}$. In the simplified case of constant wind forcing, a steady-state momentum balance from the wind to the water can be established through a constant relative ice-ocean velocity (Δu).

Here, we investigate ocean turbulence just below the marginal ice zone as a function of

the total wind stress τ_{wind}, with the implicit assumption that $\tau_{wind} = \tau_{ocean}$. Wind stress is estimated for observations using the covariance methods, which inherently integrates spatial conditions. This approach avoids partitioning momentum between open and ice-covered areas, and also avoids specification of ice-ocean drag coefficient, because total momentum flux is simply conserved through the air-water-ice interface of the marginal ice zone.

The rate at which the wind stress τ_{wind} does work on the ocean can be related to the effective speed c_e at which the dynamic roughness elements (creating surface drag) move with that stress. The rate of wind-work, $c_e\tau_{wind}$, has been used in previous studies to define the input flux of turbulent kinetic energy (TKE) to the ocean by the wind. The dynamic roughness elements at the surface in open water are short waves, and the effective transfer velocity for wind-work is thus related to the phase speed of the waves [*Gemmrich et al.*, 1994]. Several studies in ice-free regions have shown that this input rate of TKE is in balance with the TKE dissipation rate ϵ integrated over an active layer depth as [*Terray et al.*, 1996; *Thomson et al.*, 2016a]:

$$c_e\tau_{wind} \approx \rho \int \epsilon(z)dz \tag{4.2}$$

Thus, in ice-free regions the turbulent dissipation rate ϵ is often parameterized using the wind stress and an effective transfer velocity related to wave phase speed. As the roughness of the open ocean is primarily dependent on the short waves, it has been found that a typical open water effective transfer velocity is approximately $c_{eo} \approx 2$ m/s [*Thomson et al.*, 2016a]. This value can be adjusted according to the wave age, which is the ratio of the phase speed at the peak of the wave spectrum to the wind speed, c_p/U_{10} [*Terray et al.*, 1996]. It should be noted that these formulations for TKE in ice-free areas are much larger than law-of-the-wall estimates would suggest, because breaking surface waves directly inject turbulence at much higher rates than shear production can supply [*Agrawal et al.*, 1992]. This approach then inherently neglects viscous stresses, which are likely to be much smaller than wave-supported stresses in all but the lowest wind conditions [e.g., *Grare et al.*, 2018].

One previous study has applied this model for wind-work via an effective transfer speed to a marginal ice zone (MIZ). *Zippel and Thomson* [2016] found the effective transfer speed

to be a function of ice concentration, in addition to wave speed. Waves decrease in amplitude with distance into the MIZ due to attenuation processes. The *Zippel and Thomson* [2016] study showed that the attenuation of waves with increasing ice concentration in the MIZ reduced the growth rate of waves due to the wind. Thus, ice reduced the amplitude of the roughness elements and thereby the wind-work and associated TKE input rate. This prior study used observations in an old marginal ice zone with melting ice floes. Here, we apply observations in several newly forming (freezing) marginal ice zones and test the dependence of the effective transfer velocity on wave and ice conditions. It is expected that the effective transfer speed in such MIZs may have a dependence on both ice concentration and thickness, as the amplitude of the short waves, which typically dominate the roughness at the ocean surface, is strongly related to the volume of ice.

When there is sufficient ice such that waves are small or absent, the roughness of the surface is dominated by the ice, rather than the waves. The roughness elements then move at a speed relative to the ocean that is set by the velocity of the sea ice. The present study tests this relative ice-ocean velocity as an effective transfer velocity of wind-work to determine the input rate of TKE to the upper ocean. We retain the framework of Eq. 4.2, where the input rate of TKE from wind through ice balances the TKE dissipation. We identify this as a distinct regime, in which the input rate c_e is determined by the motion of the ice rather than by the motion of the waves.

In addition to the mechanical forcing of wind-work, buoyancy flux (B) may be important in ice-covered oceans due to the generation of dense, salty water with ice formation [e.g., the brine rejection reviewed in *Morison et al.*, 1992]. Recent observational work in the Canada Basin by *Gallaher et al.* [2016] evaluated thermodynamic evolution of the upper ocean and local freshwater and associated buoyancy fluxes. They found buoyancy fluxes equivalent to a TKE flux on the order of 10^{-8} to 10^{-7} m^2 s^{-3}. In comparison, previous estimates of near-surface turbulence in the Canada Basin MIZ were on the order of 10^{-5} to 10^{-3} m^2 s^{-3}[*Zippel and Thomson*, 2016]. The buoyancy term in this region is relatively small and the mechanical input at the air-ice or ice-ocean interface likely is the dominant source of TKE.

Another potential source of TKE input to the ocean surface layer, in addition to wind-work, is the turbulence generated directly by wave-ice interactions. It is well-established that dissipative processes cause nonconservative attenuation of wave energy in the marginal ice zone, but the exact mechanisms remain unknown. Possible mechanisms include drag at the base of the ice layer, viscous drag within the ice layer, breakup of floes, and inelastic floe-floe collisions. In the absence of wind (i.e., swell conditions), waves might cause ice floes to move relative to the water below and dissipate wave energy in the form of turbulence. This process has been suggested to be especially dominant in thin, new ice types [*Kohout and Meylan*, 2008], and for long period waves [*Ardhuin et al.*, 2016]. *Doble and Bidlot* [2013] found that inclusion of this parameterization in a wave model (WAM) improved agreement with observations of waves in sea ice. Although turbulence production by ice-ocean drag has been proposed as an important mechanism for attenuation of wave energy in sea ice, there have been no direct observations of this relationship to our knowledge. This mechanism is difficult to isolate in the present study, because most of the conditions have young waves that are strongly correlated with the local winds (i.e., no swell conditions are observed). In the chosen framework for this study, the local winds provide all of the forcing, and waves mediate that forcing without directly providing additional input. Although this approach may be incomplete, in terms of mechanisms, it has an advantage of being completely local (i.e., it does not require knowledge of spatial gradients in wave energy flux through the MIZ).

In the following sections, we use observations of turbulent dissipation rates in open water and new pancake and frazil ice cover to explore how turbulence is altered in the marginal ice zone. Central to this approach is an assumption that wind-work generates turbulence at a rate given by the wind stress and an effective transfer speed, and that turbulence is then dissipated locally in the ocean surface layer. To match the observations, we define parameterizations for effective transfer velocities based on wave and ice conditions. We present three regimes, each with an example case.

1. In the ice-free open ocean, the effective transfer velocity is related to wave phase speed.

2. In thin ice when the sea state is relatively high, the effective transfer velocity is reduced relative to open water as a result of damping by ice.

3. In thin ice when the sea state is low, either due to low wind or strong wave attenuation, the effective transfer velocity is related to the relative velocity between ice and ocean.

After presenting these results, we discuss the transition point between these regimes and limitations of the framework. Finally, we briefly evaluate the implications for near-surface turbulence as a possible mechanism for wave attenuation (i.e., direct wave energy loss) in the marginal ice zone.

4.2 Methods

This study uses upper-ocean turbulent dissipation rate profiles from field campaigns in both the Arctic and Antarctic MIZ during autumn ice advance. Vertical profiles of dissipation rates, $\epsilon(z)$, in the upper 0.5 m of the ocean were made using a Nortek 2 MHZ Aquadopp HR Doppler profiler installed on SWIFT drifters [*Thomson*, 2012]. We will first describe the field campaigns and data collection, and then describe the instrument and turbulent dissipation rate data processing methods.

4.2.1 Field campaigns

Around 350 hours of SWIFT buoy data were obtained in the Beaufort and Chukchi Seas in the Arctic Ocean during the *Arctic Sea State* field campaign, which took place from 01 October to 10 November, 2015 on the *R/V Sikuliaq*. An overview of the field campaign can be found in *Thomson et al.* [2018], with further details in the referenced papers. Additionally, we will use approximately 5 hours of measurements obtained in the Ross Sea in the Antarctic during the *Polynyas and Ice Production in the Ross Sea (PIPERS)* field campaign from 11 April to 14 June, 2017 on the *R/V Palmer*. Locations of buoy deployments made during these two field campaigns that will be utilized in this study are shown in Figure 4.1.

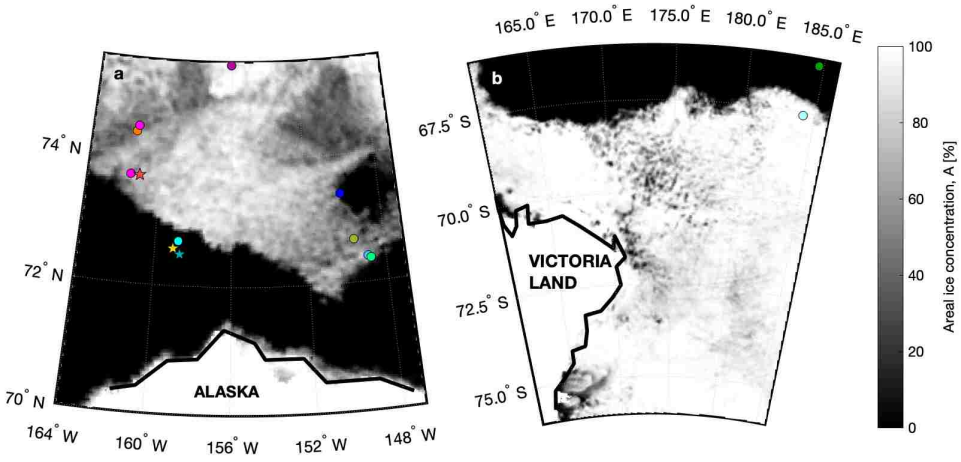

Figure 4.1: Map of SWIFT deployments in (a) Beaufort Sea, Arctic Ocean (2015) and (b) Ross Sea, Southern Ocean (2017). Grayscale shading indicates ice concentration from AMSR2 [*Spreen et al.*, 2008] where white indicates 100% ice cover and black represents open water. Each colored point represents one SWIFT deployment, where the color corresponds with deployments used in subsequent plots, and stars indicate those shown in example plots in Results. Conditions observed during each deployment are summarized in Table 4.1.

Deployments span three different regimes describing how momentum from wind stress is transferred to near-surface turbulence: open water, 'wave-transferred' MIZ, and 'ice-transferred' MIZ. Images of example conditions during each of these regimes are shown in Fig. 4.2, and complete time series and profile data corresponding to each of these examples follow in Results. Open water deployments were separated based on images taken by the buoys and recorded ship-based observations. Wave-transferred and ice-transferred MIZ deployments were categorized primarily based on ice concentration, with the ice-transferred regime expected to occur when ice concentrations were over 80% and waves were small. Deployments that did not clearly fall into one regime or had multiple regimes represented over time were not used. Conditions during all deployments used in subsequent analysis are summarized in Table 4.1. Time series and profiles for all deployments are given in the Supplemental Material.

Ship-based measurements of key parameters are collocated with buoy measurements when they are within 5 km. During both field campaigns, visual observations of sea ice were made hourly following the ASPeCt protocol, which includes estimates of ice thickness (z_{ice}) and areal concentration (A). This protocol was developed by the Antarctic Sea ice Processes and Climate (ASPeCt) group in 1997 as a standard method for sea ice observations made by ships in the Antarctic pack ice, and has since been applied widely over the Arctic and Antarctic [*Worby*, 1999a]. Visual estimates of ice thickness are reasonable, with an error of approximately 30% for thicknesses less than 30 cm [*Worby et al.*, 2008]. Additional estimates of ice thickness were made during the Arctic Sea State campaign using a thermodynamic technique based on surface temperatures measured by rail-mounted Heitronics KT-15 infrared 421 thermometers [*Persson et al.*, 2018a; *Wadhams et al.*, 2018]. This method builds on satellite-based algorithms by *Yu and Rothrock* [1996] and *Wang et al.* [2010] to use measurements of skin temperature, wind, ocean freezing temperature, and energy fluxes to estimate ice thickness over approximately 3 meter spots with the surface energy budget. Estimates from visual observations and the thermodynamic method will be referred to as simply visual and thermodynamic subsequently. As we were primarily making measurements in newly

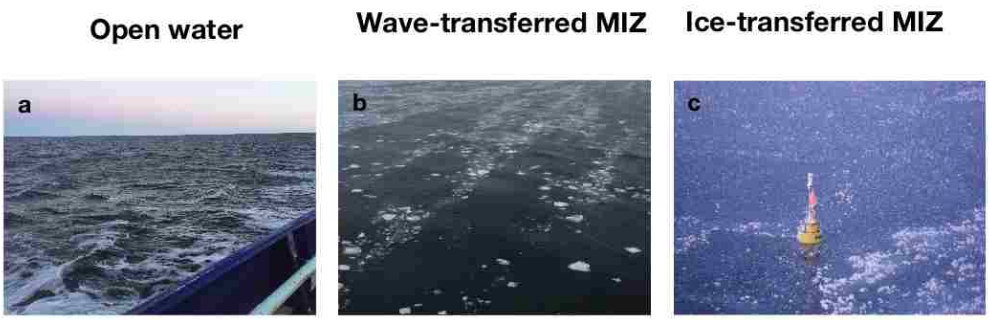

Figure 4.2: Photos taken from the *R/V Sikuliaq* of examples of the three turbulence generation regimes explored: (a) open water; (b) MIZ with wind-work transferred via waves; and (c) MIZ with wind-work transferred via ice.

formed sea ice, thickness and concentration typically varied over the scale of a few kilometers. This is typically a large enough area to represent the scale for which direct wind stress measurements integrate over.

Wind stress is calculated using observed wind speed from buoys and best estimates of drag coefficients from the ship. As the surface drag coefficient C_d can vary by nearly an order of magnitude with different types of ice cover [*Guest and Davidson*, 1991], collocated 10-minute average measurements made from the ship using the covariance method during the Arctic Sea State field campaign are used when available [*Persson et al.*, 2018a]. These measurements are significantly lower than previous bulk estimates of drag coefficients in the marginal ice zone; estimates in pancake ice during this field experiment were typically around 1.2×10^{-3}, whereas estimates using the scheme from SHEBA [*Persson et al.*, 2002a] were around 1.8×10^{-3}. As collocated drag coefficients are available only sporadically, an average drag coefficient is determined for each buoy deployment. Deployments typically span a day or two, or as little as a few hours. When ship-based measurements are unavailable (as is the case for all Ross Sea deployments), the air-ocean drag coefficient is assumed as the median of the observed values: $C_d = 1.4 \times 10^{-3}$. The use of a single drag coefficient for each deployment is justified by low range in the collocated coefficients, typically less than 20% of the average value, such that variation in wind stress is mostly captured by the variation in the wind speed. Air-side friction velocity is determined using wind velocity (measured by SWIFT buoys) as $u_{*a} = \sqrt{C_d U_{10}^2}$. Then, the ocean friction velocity u_* is calculated from air-side friction velocity using the ratio of air density (ρ_a) to average water density (ρ_w), as

$$u_* = u_{*a}\sqrt{\rho_a/\rho_w}. \tag{4.3}$$

We assume constant air and water densities of 1.225 and 1025 kg/m^3, respectively. Total wind stress imparted on the ocean is then calculated using the ocean friction velocity as

$$\tau_{wind} = \rho_w u_*^2. \tag{4.4}$$

Following the assumption that ice is not accelerating, this is assumed to be equal to the total stress τ_{ocean} received by the ocean beneath the marginal ice zone (i.e. $\tau_{ocean} = \tau_{wind}$).

4.2.2 SWIFT buoys

Surface ocean and atmospheric measurements during both field campaigns were made using SWIFT buoys. SWIFT buoys are a freely-drifting, surface following platform designed primarily to measure waves and near-surface turbulence. The relevant systems will be briefly described here, but further details of the platform and systems can be found in *Thomson* [2012] and *Smith et al.* [2018a].

The top of the 1-m mast is equipped with an Airmar PB200 ultrasonic anemometer measuring wind speed and direction, and a uCAM serial camera which takes images of the surface every 4 seconds (although image quality is limited by daylight and formation of ice over the camera lens). A Microstrain 3DM-GX3-35 combination GPS receiver and Inertial Motion Unit at the ocean surface height in the hull of the buoy is used to obtain wave spectra and bulk parameters. An AADI Aanderaa Conductivity Sensor mounted on the hull of the SWIFT (0.5-m below the surface) is used to measure temperature and salinity at 1 Hz, with a response time of $\sim$10 seconds and $\sim$3 seconds, respectively. Although bulk changes in density ρ_w over time can be observed, the response time of the instrument is not sufficient to calculate buoyancy flux.

SWIFTs used throughout this study were deployed with a Nortek Aquadopp HR mounted upwards-looking on the hull of the buoy. Velocity measurements from the upwards-looking Aquadopp HR are used to calculate turbulent dissipation, as described in the next section. Some SWIFT drifters equipped with a Nortek Aquadopp mounted downward-looking on the hull were deployed in tandem with SWIFTs with upward-looking Aquadopp HRs. Downward-looking Aquadopps measure velocity profiles from 1.5 to 21 m below the surface in 0.5-m bins. SWIFT buoys have been shown to drift with ice at the surface within 1% [*Lund et al.*, 2018] such that the observed velocity can be assumed to represent the change in velocity between the ice and ocean. Then, Δu is estimated as relative velocity between the ice and ocean 1.5 m below the surface, which is measured by the first bin of the Aquadopp profiler. Values of change in velocity from simultaneously deployed downlooking SWIFTs

(when available) are collocated with uplooking SWIFTs, which are as far as 10 km apart.

4.2.3 Turbulent kinetic energy dissipation

Nortek Aquadopp HRs were mounted facing upwards from 0.8-m below the surface on the hull of SWIFT drifters [*Thomson*, 2012]. Beam 1, which is used for turbulent dissipation rate calculations, is oriented approximately 60 degrees counterclockwise from the wind vane, to avoid measuring the wake of the buoy. Profiles are truncated at 0.5 m subsurface to remove known hull interference at the bottom of profiles.

Along-beam velocity profiles $u(z)$ are recorded by the Aquadopp at 4 Hz in 4-cm bins. Basic quality control is completed to remove velocity measurements with return amplitude and pulse correlation less than 30 and 50, respectively. These cutoffs were empirically determined by *Thomson* [2012] as the maximum corresponding to profiles out of the water and spurious points. Quality controlled velocity records are used to calculate average and turbulent (root-mean-square) velocity profiles.

Dissipation is then estimated from velocity profiles using the second order structure function, which is robust to SWIFT platform motion. The structure function is defined as

$$SF(z) =< [u(z) - u(z+r)]^2 > \tag{4.5}$$

where z is the bin depth, and r is the distance between bins [*Wiles et al.*, 2006]. Turbulent dissipation profiles $\epsilon(z)$ are estimated by fitting the structure function to a $r^{2/3}$ dependence following the methods in *Thomson* [2012] and *Zippel and Thomson* [2016]. This method has been validated by comparison with ADV point measurements of dissipation [*Thomson*, 2012] and dissipation profiles estimated using frequency spectra [*Zippel et al.*, 2018]. The application of the structure function here varies from previous applications primarily in that it uses only measurements within six bins of each depth ($6r$) and is double-sided.

When sea ice is present, reflections from ice at the surface and suspended ice particles in the water column can result in erroneous Aquadopp velocity measurements. Two quality control steps are applied to data to account for this. First, we remove data at and above

bins with spikes in correlation and amplitude that result from reflections. This approach is similar to methods that have been long used to measure ice draft with uplooking Sonar, and more recently extended to uplooking ADCPs [*Magnell et al.*, 2010; *Lohrmann et al.*, 2011]. When correlation exceeds 98% or amplitude exceeds 195, it is presumed that ice is present and velocity measurements will not provide accurate estimates of turbulence. The removal of data via this process is referred to as an "ice mask". In some cases, erroneously high velocity measurements as a result of ice contamination do not correspond to high amplitude or correlations, and result in additional peaks in the distribution of raw velocity data. Bursts of data where there is more than one significant peak in the velocity distribution are completely removed, and dissipation rates are not calculated. Of all data in the wave-transferred MIZ, approximately 3.3% of bursts are removed due to multiple peaks in the velocity distribution, and approximately 39% of the remaining data are removed as a result of other quality control metrics. Of all data in the ice-transferred MIZ, approximately 14% of bursts are removed due to multiple peaks in the velocity distribution, and approximately 34% of the remaining data are removed as a result of other quality control metrics.

4.3 Results

4.3.1 Examples

Open water (no ice) example

Time series of the wind speed, significant wave height, peak wave period, relative ice-ocean velocity, and integrated near-surface turbulent dissipation rates are shown for an open water example, 23-24 Oct 2015 (a), in Figure 4.3. Peak wave period, T_p, is related to the wave age (c_p/U_{10}) by the wave phase speed, calculated using the deep-water dispersion relation, $c_p = \frac{gT_p}{2\pi}$. Figure 4.4 shows Aquadopp HR data following quality control and processing for the same example. In open water, it is typical to see moderately high amplitudes and correlations throughout the water column. Turbulent velocities and dissipation generally peak at the surface as a result of input from breaking waves, and these parameters decay

Table 4.1: Summary of conditions for all SWIFT deployments in open water, wave-transferred marginal ice zones, and ice-transferred marginal ice zones used in this study. Deployments with * after the date correspond to examples shown in Figures 4.3-4.8. Deployments in 2015 all occurred in the Beaufort Sea, and deployments in 2017 occurred in the Ross Sea. Range of values for wind speed and wave heights are from SWIFT buoy measurements, near-surface change in velocity values are determined from a collocated SWIFT with downward-looking Aquadopp, and ice thickness and areal concentration are from ship-based visual estimates. Average air-ocean drag coefficients (C_d) shown are based on observed values collocated from the ship, except where noted by $\hat{}$, indicating constant value of 1.4×10^{-3} is used.

Date	U_{10} [m/s]	H_s [m]	Δu [m/s]	z_{ice} [m]	A [%]	C_d
Open water						
02 Oct 2015	10.5-11.7	0.95-1.2	N/A	N/A	0	1.2×10^{-3}
04 Oct 2015	6.7-11	0.4-0.6	N/A	N/A	0	1.2×10^{-3}
23-24 Oct 2015 (a)*	7.2-15	0.93-1.5	0.08-0.41	N/A	0	1.4×10^{-3}
Wave-transferred MIZ						
10 Oct 2015	4.8-11	0.17-0.54	0.22-0.75	0.03-0.04	32-46	$1.4 \times 10^{-3}\hat{}$
11-14 Oct 2015 (a)	8.9-26	2.0-4.3	0.03-0.40	0.02-0.05	15-24	1.2×10^{-3}
23-24 Oct 2015 (b)	16-29	0.12-1.4	N/A	0.02-0.09	13-50	1.4×10^{-3}
03 June 2017	8.7-12	0.35-0.80	N/A	0.2-0.3	100	$1.4 \times 10^{-3}\hat{}$
05 June 2017	4.6-14	2.3-3.9	N/A	0.5	70-80	$1.4 \times 10^{-3}\hat{}$
11-14 Oct 2015 (b)	4.0-27	2.4-4.5	0.01-0.40	0.02-0.04	6-30	1.5×10^{-3}
11-13 Oct 2015	10-19	1.2-3.9	0.01-0.40	0.06-0.1	40-85	1.4×10^{-3}
25-27 Oct 2015*	3.2-10	0.02-0.37	0.02-0.32	0.14	6-80	1.3×10^{-3}
Ice-transferred MIZ						
16-18 Oct 2015 (a)	4.0-9.0	0.06-0.30	0.02-0.56	0.08-0.1	82-85	0.8×10^{-3}
06-08 Oct 2015	2.3-7.8	0.01-0.02	0.01-0.36	0.15	99-100	0.6×10^{-3}
16-18 Oct 2015 (b)*	0.3-5.4	0.01-0.34	0.02-0.56	0.08-0.5	83-93	0.7×10^{-3}

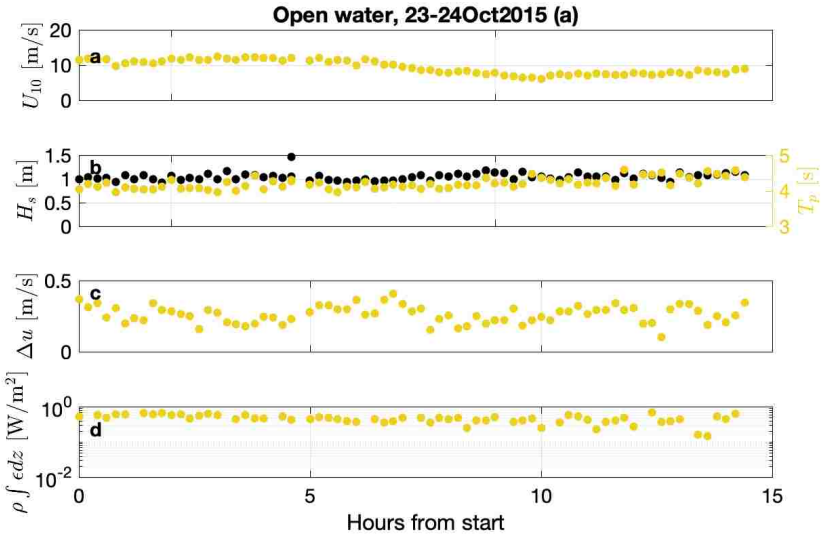

Figure 4.3: Time series from a SWIFT deployed in open water, 23-24 Oct, 2015 (a) of (a) wind speed, (b) significant wave height and peak wave period, (c) relative velocity of ice and ocean (at 1.5 m depth), and (d) vertically integrated TKE dissipation rates.

with depth [e.g., *Thomson et al.*, 2016a].

Wave-transferred MIZ example

The time series in Figure 4.5 shows an example of conditions encountered during a deployment in a wave-transferred MIZ. In addition to those shown in Fig. 4.3, panel (c) shows the ice thickness and concentration, which are increasing over time in this example. Figure 4.6 shows the Aquadopp HR data following quality control and processing specific to

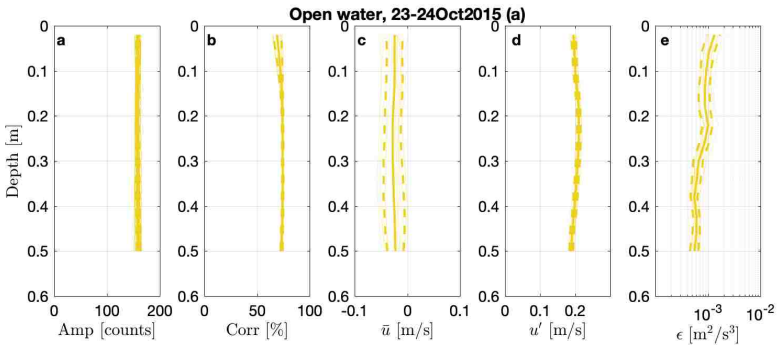

Figure 4.4: Aquadopp burst data from SWIFT deployed in open water, 23-24 Oct, 2015 (a). Vertical profiles of (a) amplitude, (b) pulse correlation, (c) average velocity, (d) turbulent velocity, and (e) dissipation rate.

observations in sea ice cover. Initially, dissipation profiles are similar in shape and magnitude to those observed in open water. The correlation and amplitude values are moderate, such that dissipation rate can be calculated over the entire profile. As sea ice thickness and concentration increase over time, turbulent velocities and dissipation rates rapidly decrease. The "ice mask" is applied to the later profiles at and above depths with high correlations or amplitudes, which is indicated by the gray shading in Fig. 4.6. The depth of the ice mask provides an estimate of sea ice thickness (Fig. 4.5c), in addition to the thickness estimates from the shipboard sampling.

Ice-transferred MIZ example

The example of Aquadopp HR data following quality control and processing in an ice-transferred MIZ in Figure 4.8, with corresponding time series in Fig. 4.7, shows a more extreme application of this quality control. (Note that the change in upper ocean velocity, Δu, is from a collocated buoy deployed later and no values are available for the first 11 hours.) Here, the upper bins of the dissipation profile cannot be calculated throughout the whole observation period due to the presence of significant ice. The bin-averaged dissipation

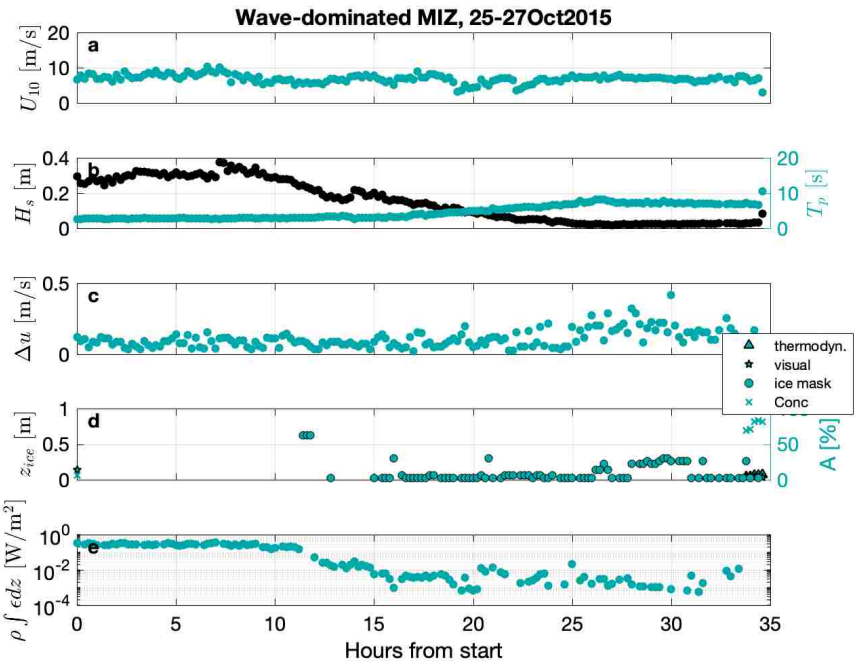

Figure 4.5: Time series from SWIFT deployed in wave-transferred MIZ, 25-27 Oct, 2015 of (a) 10-m wind speed, (b) significant wave height and peak wave period, (c) relative velocity of ice and ocean (at 1.5 m depth), (d) ice thickness and concentration estimates, and (e) vertically integrated TKE dissipation rates.

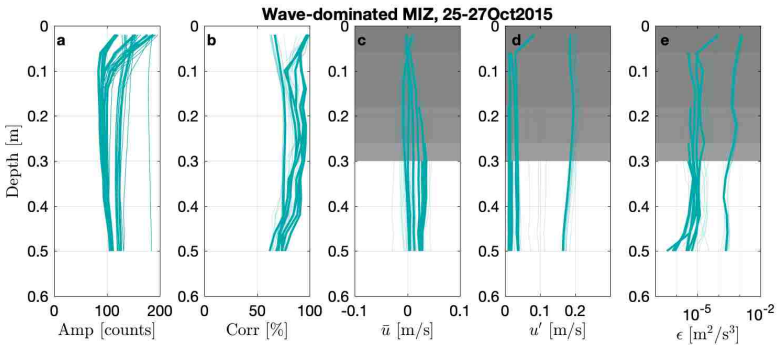

Figure 4.6: Aquadopp burst data from SWIFT deployed in wave-transferred MIZ, 25-27 Oct, 2015. Vertical profiles of (a) amplitude, (b) pulse correlation, (c) average velocity, (d) turbulent velocity, and (e) dissipation rate. Thick lines indicate averages binned by ice mask, and gray shading corresponds to ice mask for each bin.

rate profiles show that dissipation still decays with depth.

The examples of each of the three turbulent transfer regimes demonstrate the processes controlling the balance of wind-work and turbulent dissipation. In open water (Figs. 4.3-4.4), the integrated TKE dissipation rate decreases with declining wind speed. In the wave-transferred MIZ example (Figs. 4.5-4.6), dissipation rates decrease with declining wave height and increasing ice, rather than any change in the wind (which is relatively constant in time). In the ice-transferred MIZ example (Figs. 4.7-4.8), dissipation is more variable over time, but appears to be most closely tied to changes in the wind and relative ice-ocean velocity (Δu). The physical mechanisms distinguishing the wave-transferred and ice-transferred MIZ regimes are explored further in the next sections using the full data set and spanning a range of conditions. Table 4.1 summarizes characteristic values of key variables, but the subsequent analysis uses full time series of observed values as shown in the Figures in the Supplemental Material.

As we are interested in understanding what controls enhanced turbulence at the surface above background levels, subsequent presentations of integrated dissipation rates, $\rho \int \epsilon dz$, all

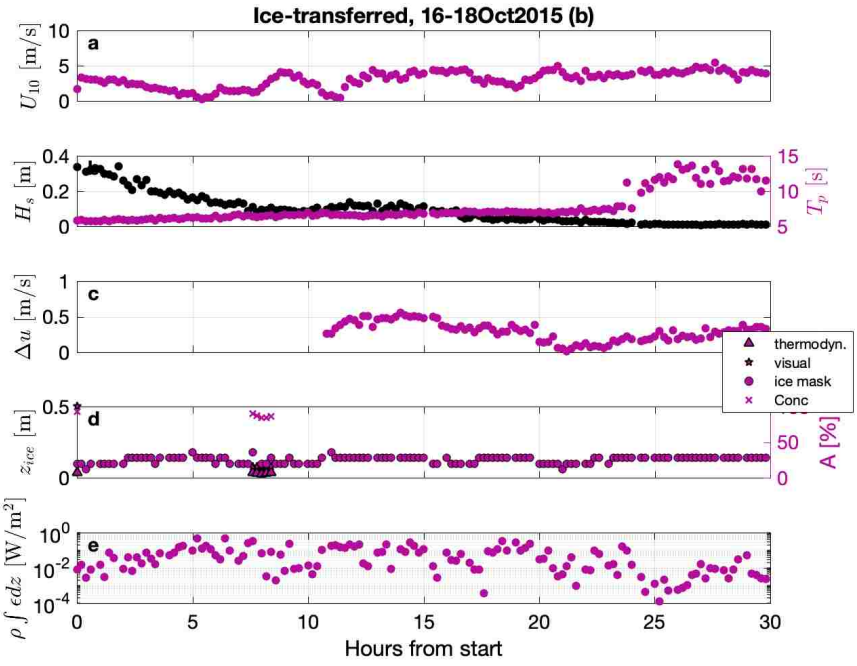

Figure 4.7: Time series from SWIFT deployed in ice-transferred MIZ, 16-18 Oct, 2015 (b) of (a) wind speed, (b) significant wave height and peak wave period, (c) relative velocity of ice and ocean (at 1.5 m depth), (d) ice thickness and concentration estimates, and (e) vertically integrated TKE dissipation rates.

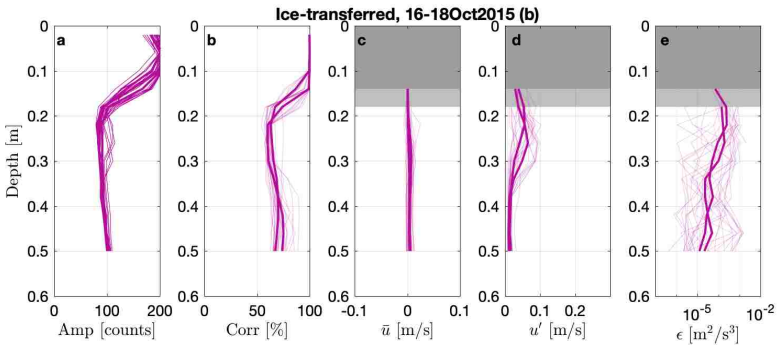

Figure 4.8: Aquadopp burst data from SWIFT deployed in ice-transferred MIZ, 16-18 Oct, 2015 (b). Vertical profiles of (a) amplitude, (b) pulse correlation, (c) average velocity, (d) turbulent velocity, and (e) dissipation rates are colored by time (hours) from the beginning of the deployment. Thick lines indicate averages binned by ice mask, and gray shading corresponds to ice mask for each bin.

have an average offset removed. The offset for each deployment is calculated as the integrated value using the average of the measured dissipation rate at the bottom of the profile, $z = 0.5$ m, which is generally the lowest magnitude of ϵ in the profile.

4.3.2 Open Water (no ice)

The input rate of TKE in open water is calculated as $c_e \tau_{wind}$ using measured wind stress and estimates of open water effective transfer velocity. Effective transfer speed is estimated using a typical parameterization based on wave age,

$$c_e \approx c_{eo} \left(\frac{c_p}{U_{10}} \right) \tag{4.6}$$

where c_p is the wave phase speed at the peak of the spectrum and U_{10} is the wind speed [*Terray et al.*, 1996; *Thomson et al.*, 2016a]. The canonical effective transfer speed typical in open water is $c_{eo} = 2$ m/s, and the wave age dependence is weak [*Thomson et al.*, 2016a]. The open water points (warm colors) in Figure 4.9 show that this wind input rate balances with the observed vertically integrated dissipation rates, consistent with previous studies in

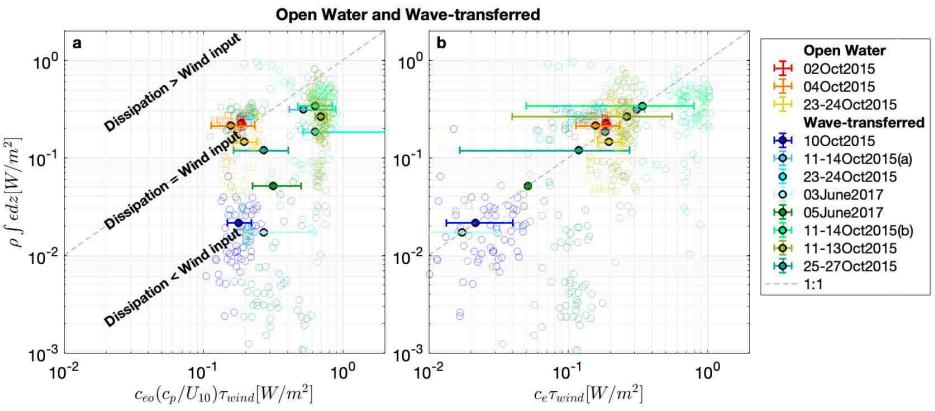

Figure 4.9: (a) Comparison of vertically integrated TKE dissipation rates with input rate from wind expected based on open water conditions. (b) The same comparison where input rate for the wave-transferred MIZ uses effective transfer velocities determined assuming a balance of wind input and observed dissipation rates. Each color represents a SWIFT deployment (warm colors represent open water, and cool colors represent wave-transferred MIZ), and filled points represent averages for each deployment. Bars represent the range of measured drag coefficients, when applicable. Dashed black line is the 1:1 line, where expected input and dissipation are equal. Wave-transferred MIZ bin-averages in (b) have been forced to lie on the line.

open water. Each open point represents an hourly value, and filled points represent averages from each deployment. The dynamic range observed is small, but the open water balance is not the focus of the present study.

4.3.3 Wave-transferred MIZ

Measurements in the MIZ with waves present are plotted on Figure 4.9 (a) (cool colors) using the open water parameterization for effective transfer velocity in Eq. 4.6. Dissipation rates are lower than the expected input rate (i.e., points are below the 1:1 line). Deployments from 11-14 Oct had larger wind stress observations than the deployments in open water, and

yet the observed integrated dissipation rates are comparable. *Zippel and Thomson* [2016] argue that dissipation rates in the MIZ are reduced as a result of lower effective transfer velocities in ice cover. We can estimate appropriate effective transfer velocities (c_e) for these deployments by assuming that observed dissipation rates in the wave-transferred MIZ are in equilibrium with local energy input from wind, as in Eq. 4.2. Figure 4.9b shows the same comparison of wind input and observed integrated dissipation, where c_e values for the MIZ cases have been determined using the assumption of equilibrium.

We find effective transfer velocities in the wave-transferred MIZ in the range of 0.01-0.8, with most clustered around 0.1-0.5. In contrast with typical relationships in open water, the MIZ transfer velocities do not depend on wave age. Instead, the MIZ effective transfer velocities have a positive correlation with wave height, and a negative correlation with ice thickness and concentration (to be shown later as a combined parameter in the Discussion section).

4.3.4 Ice-transferred MIZ

When the sea state is low, the roughness of the surface is set primarily by the ice, rather than the waves. The observed drag coefficients (C_d) in this regime are lower as a result of the milder wind and wave conditions and higher ice concentrations. The input of turbulent kinetic energy from the wind to the ocean is then mediated by the motion of the ice. For these conditions, we test the concept of an effective transfer velocity that is set by the relative velocity between ice and upper ocean, Δu, such that the rate of wind-work is

$$c_e \tau_{wind} = \Delta u \tau_{wind}. \tag{4.7}$$

Similar to the relationship of the open water transfer velocity to the wave speed, the proposed transfer velocity $c_e = \Delta u$ is intended as a characteristic velocity scale, rather than a quantitative description of the shear velocity. This assumes that the ice is moving at a constant speed relative to the ocean, such that work is being transferred through the ice (and not being done on the ice).

This parameterization of TKE energy input rate from the wind is moderately correlated with the observed integrated dissipation rate under ice, as shown in Figure 4.10. Hourly measurements are represented by open circles, and bin-averages by ice mask depth are shown as filled circles. Bars represent the standard error of the averages, but not the error associated with velocity or wind stress measurements, both of which may be significant. Bin-averages are necessary to satisfy the assumption that the material derivative of turbulence is zero, and averaging over similar ice conditions is most appropriate, as changing ice thickness is expected to most significantly change the total turbulent kinetic energy. A linear fit to the bin-averaged measurements has a coefficient of determination $R^2 = 0.50$ and probability of false-correlation $P = 0.015$. We note that when all hourly measurements are used for a linear fit, the significance decreases substantially with an $R^2 = 0.02$ and $P = 0.20$. The binned averages are all within an order of magnitude of the 1:1 line, and the overall dependence is consistent with increasing TKE dissipation rates in the presence of increasing wind input rates.

4.4 Discussion

4.4.1 Scaling turbulent regimes in the MIZ

When waves are the dominant roughness in the MIZ, the effective transfer velocity is expected to be a function of wave and ice characteristics. *Zippel and Thomson* [2016] examined controls on the transfer velocity and input rate in brash ice (small fragments of ice, ¡2 m, formed from the wreckage of other types) and found that the effective transfer velocity in brash ice decreased with increasing ice concentration. The measurements used in this study were all made in frazil ice cover (a collection of loose ice crystals) and pancake ice cover (round pieces of ice formed by waves), both of which form in turbulent conditions.

The transfer velocity is primarily associated with the high frequency waves that dominate surface roughness. High frequency waves in the equilibrium range have been shown to be a strong function of ice cover, and the magnitude of spectral damping varies with the ice

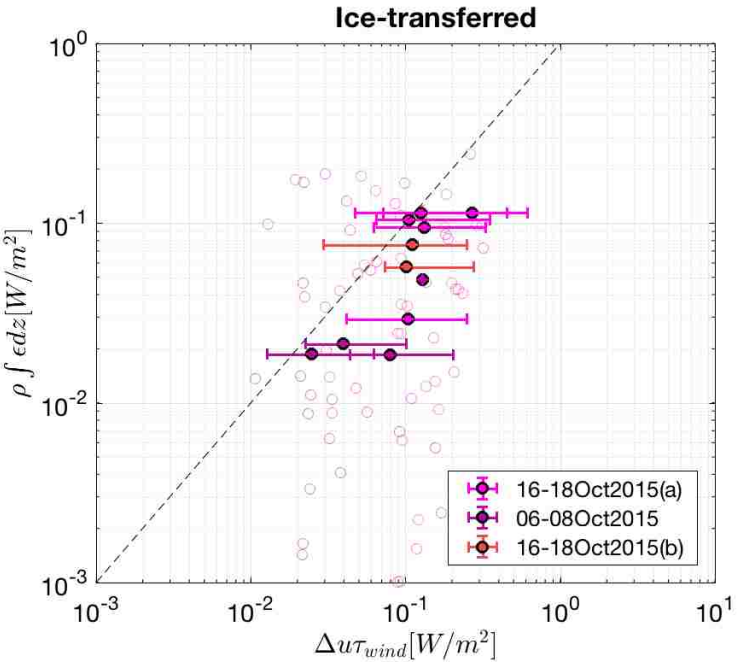

Figure 4.10: Comparison of vertically integrated TKE dissipation rates and expected input rate from ice to ocean in marginal ice zones where wind stress is ice-transferred. Each color represents a SWIFT deployment, and filled points represent ice-mask binned averages. Error bars represent the range of measured drag coefficients. Dashed black line is 1:1 line, where expected input and observed dissipation are equal.

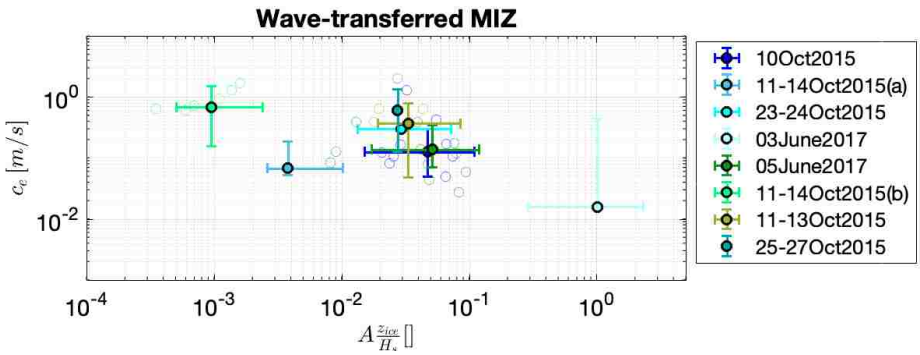

Figure 4.11: Effective transfer velocity in wave-transferred MIZ using the results of Fig. 4.9, as a function of ice concentration and nondimensional ice thickness ($A\frac{z_{ice}}{H_s}$). Each color represents a deployment in the wave-transferred MIZ.

characteristics [*Rogers et al.*, 2016]. It is then essential to consider ice characteristics in addition to the wave height, as the magnitude of damping at high frequencies may not be fully reflected in the significant wave height (which is weighted towards the swell waves). The effective transfer velocity is expected to decrease with increasing ice volume, by increasing concentration or thickness, and decreasing wave heights.

In Figure 4.11 we compare a proposed scaling parameter incorporating wave and ice conditions, $A\frac{z_{ice}}{H_s}$, with the effective transfer velocity in ice, determined by assuming local wind input and dissipation are precisely balanced (Fig. 4.9b). This nondimensional parameter and the effective transfer velocity appear to be related by a power law with the form:

$$c_e = a\left(A\frac{z_{ice}}{H_s}\right)^b \tag{4.8}$$

This parameterization is for the regime where transfer in the MIZ is dominated by surface waves, so it will not be valid at the limit as H_s approaches zero where transfer is dominated by ice. The upper limit on this parameterization will be the open ocean transfer velocity (Eq. 4.6) at very small values of Az_{ice}.

Applying a power law fit yields values for the coefficients $a = 0.11 \pm 0.10$ m/s and $b = -0.23 \pm 0.20$, with a coefficient of determination $R^2 = 0.45$ and a probability of false

correlation $P = 0.25$. Although these coefficients are not well constrained by the small number of measurements in this study, the formulation may be useful for future studies. Thickness is likely necessary to parameterize changes in the TKE input rate for these new-ice conditions, as thickness represents a larger change in total ice volume in the relatively thin pancake and frazil ice. In the thicker brash ice of *Zippel and Thomson* [2016], the percent change in volume is mostly described by changes in concentration.

Combining parameterizations for the effective transfer velocity in the wave-transferred and ice-transferred MIZs allows estimation of near-surface turbulent dissipation from open water into thin, new ice cover using the effective transfer framework of Eq. 4.2. The effective transfer velocity c_e is found to be a function of the wave and ice conditions which control roughness. When conditions are such that turbulence production is likely to be transferred via waves, the transfer velocity can be estimated using estimates of ice thickness, concentration, and significant wave height. When conditions are such that turbulence production is likely to be transferred via ice, the effective transfer velocity is the change in near surface velocity (Δu). Then, the dependencies of the effective transfer velocity through these three regimes can be summarized by the piece-wise function:

$$c_e \approx \begin{cases} c_{eo}\left(\frac{c_p}{U_{10}}\right) & \text{OPEN WATER} \\ a\left(A\frac{z_{ice}}{H_s}\right)^b & \text{WAVE-TRANSFERRED MIZ} \\ \Delta u & \text{ICE-TRANSFERRED MIZ.} \end{cases} \tag{4.9}$$

The resulting estimates of integrated near-surface dissipation are shown schematically in Figure 4.12. Our representation of this piece-wise function suggests that the transfer velocity in the wave-transferred MIZ is bound by the transfer velocities in open water and the ice-transferred MIZ, i.e. $c_{eo}(\frac{c_p}{U_{10}}) > a(A\frac{z_{ice}}{H_s})^b > \Delta u$. It is hypothetically possible for Δu values to approach open water transfer velocity values, although velocities are typically an order of magnitude lower in this dataset.

It is clear in Fig. 4.12 that the local dissipation in the MIZ regimes described will always be lower than in open water. The parameterization for the ice-transferred MIZ is

additionally expected to represent an upper bound on the work done by the wind on the ocean, as the parameterization for the effective transfer velocity relies on the assumption that the relative velocity between ice and ocean is constant (i.e. ice is not accelerating). The observed integrated TKE dissipation rates in Figure 4.10 are lower than those predicted by the parameterization, possibly indicating some additional work is being done on the ice.

These predictions provide estimates for the vertically integrated dissipation in the near-surface (upper 0.5 m). In all cases, the dissipation rate maximum is at the surface (or the base of the ice) and monotonically decreasing with depth. Although the total dissipation clearly depends on the extent of the vertical integral, the steep vertical profiles suggest that the majority of the dissipation occurs within 0.5 m of the surface.

These results suggest that turbulence production can be parameterized in either regime based on wave and ice conditions; however, it is necessary to determine whether wind-work is wave-transferred or ice-transferred. We introduce a non-dimensional scaling parameter, which we call W, representing the ratio of wave-transferred and ice-transferred transfer velocities. This parameter can be used to determine whether wind input to waves or input ice dominates near-surface turbulence, and can be related to observed ice and wave conditions based on the power law fit (Figure 4.11) in Eq. 4.8, such that

$$W = \frac{0.11}{\Delta u}\left(A\frac{z_{ice}}{H_s}\right)^{-0.23}. \tag{4.10}$$

We expect that when this parameter is high, input from wind will be wave-transferred, and when it is low, input will be ice-transferred.

The range of values of W calculated for SWIFT deployments categorized as wave-transferred and ice-transferred are summarized in Figure 4.13. This figure includes all measurements in each regime where all four of the required variables are available (n=65 in the wave-transferred MIZ regime; n=107 in the ice-transferred MIZ regime). We expect conditions associated with this value to be quasi-steady, such that they vary on the hourly timescale. The Δu time series, which has measurements every 12 minutes, has substantial temporal noise associated with the challenge of using a narrow-band Doppler measurement

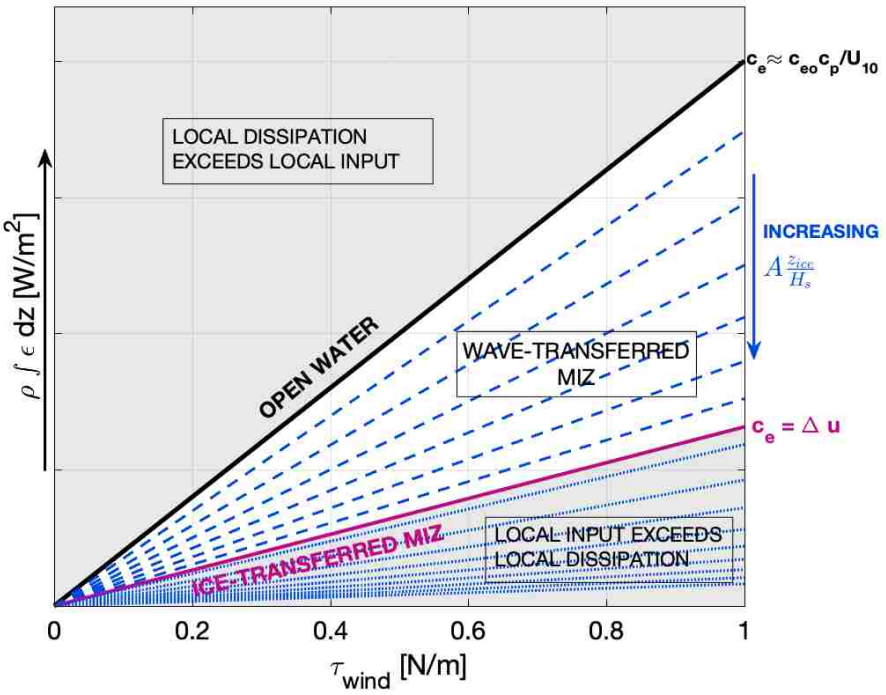

Figure 4.12: Schematic representation of integrated near-surface dissipation rate predicted as a function of wind stress, on the x-axis, and the effective transfer velocity, given by the slope of each line. This result assumes a local balance of turbulence production from wind input and dissipation. The largest dissipation rate will occur in open water conditions, where transfer velocity c_e in a young wave field is typically twice the wave age [black line; *Thomson et al.*, 2016a]. The effective transfer velocity in ice decreases as the ice increases and the wave height decreases, such that the ratio $A\frac{z_{ice}}{H_s}$ increases (blue lines). Typically, the smallest dissipation rates will be observed when the effective transfer velocity is set by the relative ice-ocean velocity, Δu (purple line), as is commonly seen in nearly 100% ice cover. Grey shaded areas represent regimes where local production and dissipation are not in balance.

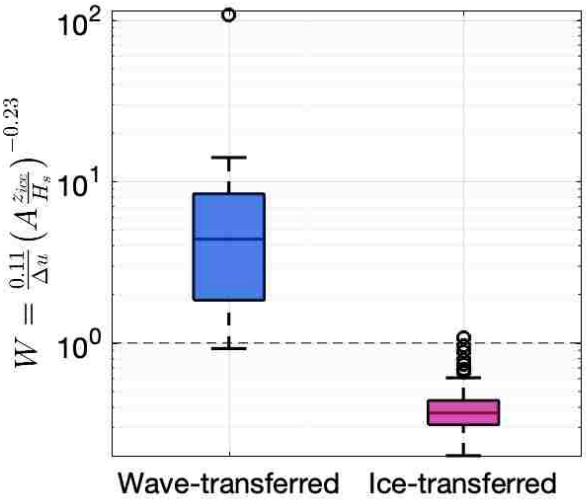

Figure 4.13: Boxplot of scaling parameter, W (Eq. 4.10), calculated for SWIFT deployments in wave-transferred MIZ (blue) and ice-transferred MIZ (purple). Boxes contain interquartile range of data, and whiskers contain data within 2.7σ of median. Dashed line at $W = 1$ indicated proposed threshold for transition in dominant generation mechanism.

in the low scattering environment of the Arctic. This velocity time series was smoothed using the moving average method with a span of 3, such that the resulting time series represents changes over 36 minute periods.

Values of W are expected to be lower for observations in the ice-transferred MIZ than for observations in the wave-transferred MIZ, as the observations were initially sorted qualitatively based on small waves and high ice concentration (as described in the Methods). Additionally, we find that wind stress in the MIZ is generally wave-transferred if $W > 1$, and ice-transferred if $W < 1$. This parameter provides a more quantitative and less subjective method for separating observations in future work. As this nondimensional parameter is derived from the ratio of transfer velocities, this result indicates that the wind stress will drive turbulence generation through the roughness element with the fastest characteristic velocity. The turbulence generation can then be parameterized the same way in both MIZ regimes, using the largest relevant transfer velocity.

The application of the scaling and equations for approximate dissipation should be limited to a similar range of conditions as those observed, with low to moderate sea state and thin, new sea ice cover. These conditions are most common during the autumn and winter near the advancing ice edge. Additionally, following the assumption of a local energy balance, it is necessary to average over the time scale in which ice conditions are relatively constant to ensure stationarity.

Products of ice thickness, wind speed, and wave height are available for many areas by satellite and/or reanalysis products, and may be useful for large-scale estimates of turbulence from this method. Wind and wave data may be obtained from the ERA-Interim reanalysis [*Dee et al.*, 2011], for example, but it should be noted there has been little validation of the wave results in sea ice cover. Comparison of different available sea ice thickness products can be found in *Labe and National Center for Atmospheric Research Staff* [11 Sep 2017]. In particular, skill in measuring thin sea should be considered, which has been suggested to be well captured by microwave techniques. The relative ice-ocean velocity cannot be estimated from remote sensing products and caution should be used in replacing with other velocity

estimates such as ice drift speed, which was found to have low correlation in these data (not shown). The relative ice-ocean velocity is likely best estimated currently with coupled models [*Yang*, 2006].

It is possible to parameterize the observed changes in TKE dissipation rates in other ways, such as a model in which the effects of ice on near-surface turbulence is fully accounted for by reduction of wind stress into the ocean (i.e. by application of Eq. 1). Although this model may be more in line with what has been previously applied for partially ice-covered oceans [e.g., *Yang*, 2006], the thin MIZ may be more dynamically similar to open ocean, and thus application of the open water effective transfer velocity framework may be more appropriate. Additionally, such a model would require detailed observations of ice-ocean stress, which we do not have here. Observations of wind stress, as we have in this study, are more commonly available and often made from ships.

4.4.2 Buoyancy flux

It has been previously suggested that near-surface buoyancy production during sea ice formation may provide an additional source of turbulence. Lacking a direct estimate of the buoyancy flux, we make a rough estimate for the observations with the strongest ice growth (25-27 Oct) using the approximate freshwater flux. The total increase in ice volume over the approximately six hour deployment corresponds to a negative freshwater flux of 1.1 m^3/day. This corresponds to an approximate salt flux of 3.5×10^{-5}, which is converted to a buoyancy flux of $3.5 \times 10^{-6} m^2/s^3$ by multiplying by g/ρ. Referring back to the dissipation rates in Figure 4.6, we see that this estimate of buoyancy flux is small compared to the observed dissipation values, even during this case of rapid ice growth. Buoyancy is only likely to become a significant source when wind input via waves and ice is sufficiently low, and ice formation is exceptionally rapid.

4.4.3 Dissipative mechanisms for waves in ice

Turbulence under ice has been proposed as a possible key dissipative mechanism for wave energy in marginal ice zones [*Kohout et al.*, 2011]. Although the attenuation of wave energy in the marginal ice zone has been extensively studied and significant work is ongoing to parametrize attenuation rates [i.e. *Cheng et al.*, 2017], the actual mechanisms are still an open question. By using winds as the universal source of upper ocean turbulence, communicated by either waves or sea ice, the present study has excluded the possibility that observed turbulence is caused directly by attenuation of waves propagating through the ice.

Although our approach is inherently focused on under-ice turbulence due to local wind input, our observations of turbulent dissipation rates do not point to near-surface turbulence as a strong attenuation mechanism. We observe that turbulence is always suppressed in the MIZ compared to open water values (Fig. 4.9). In open water, similar wind stresses as those we observed in the MIZ would result in significantly larger dissipation values to maintain the expected balance. However, the wind input to waves in the MIZ is not well-constrained; the 1:1 line from the open water parameterization (Fig. 4.9) thus is an upper bound on what the dissipation in the MIZ would need to exceed for wave attenuation to occur. The strong correlation of winds and waves in the young, often fetch-limited, seas of these data sets prevent a rigorous isolation of these mechanisms.

The relative importance of wave attenuation via turbulence is likely different across the various conditions observed here. Closer examination of time series of observations from one deployment in the wave-transferred MIZ show that the rapid drop of turbulent dissipation with increasing ice (i.e. Figure 4.5) occurs well before the decrease in wave energy, such that turbulent dissipation is unlikely to account for the observed wave attenuation over time. This case is particularly illustrative, as the winds are mostly constant over time, such that the changes in waves are coupled to changes in ice, rather than wind. If this relationship holds in ice-transferred conditions, as well, then the decrease in energy input from wind to waves will correspond to a decrease in energy lost from the wave field to the upper ocean as

turbulence. As in the wave-transferred MIZ, we find that the values of near surface turbulent dissipation when ice controls the wind input are almost always lower than those observed in open water (Fig. 4.10).

Although some energy will be lost from the wave field to turbulent dissipation via wave breaking and/or ice-ocean shear in both MIZ regimes, these results suggest that local wind input is a key driver of turbulent dissipation. The observed turbulent dissipation rates can largely be accounted for by the local wind. It is thus challenging to decouple local input via wind and input from attenuation of wind seas over the MIZ. Additionally, comparison of wave attenuation coefficients (calculated by *Cheng et al.* [2017]) with integrated dissipation shows that attenuation rates are not correlated with observed local dissipation rates. Direct contributions to turbulence from wave energy may be significant under some MIZ conditions outside of those observed here, and is likely to be significant under larger, thicker ice floes. Further work is necessary to determine which of the other possible mechanisms for dissipation of wave energy are important, and under what conditions they apply. For the new, thin ice herein, other dissipative mechanisms such as viscous drag within the ice layer, or floe-floe collisions [*Shen and Squire*, 1998] may be key mechanisms for wave attenuation.

4.5 Conclusions

This study uses observations to build a framework for estimating near-surface turbulent dissipation rates in marginal ice zones with relatively thin ice. Here, "thin ice" is used to describe newly formed frazil and pancake ice, where the ice thickness is approximately 50 cm or less. The near-surface turbulent dissipation rate is a function of the total wind stress, which does work on the ocean at an effective transfer rate. This is the characteristic speed at which roughness elements move in the dynamic boundary layer, and will be either be related to the wave or ice speed in new MIZs. In situ measurements of turbulence dissipation profiles across a range of conditions in newly formed sea ice allow parameterization of the effective transfer velocities controlling TKE input rate. We have introduced a scaling parameter, W, which may be used to determine the dominant roughness elements controlling the rate of

wind-work on the ocean, based on observed or estimated sea ice thickness and concentration, wave height, and relative ice-ocean shear velocity. Energy input rate for turbulence generated by wind may then be estimated using calibrated relationships determined by this study.

We do not observe under-ice dissipation values that exceed wind input rates in the marginal ice zone, and as such we speculate that wave attenuation modulates turbulent dissipation but does not cause it directly. In other words, local wind input may be more important than dissipation of wave energy from remote sources (i.e. attenuation of swell waves) for the generation of turbulence in thin, young MIZs.

These results build on those of *Zippel and Thomson* [2016] and others to provide parameterizations for near-surface turbulent dissipation in the marginal ice zone. These may be applied for the purposes of estimating gas exchange, heat and momentum transport. Further field and lab measurements of turbulent dissipation are necessary to improve physical understanding of mechanisms and expand parameterizations to a wider variety of conditions. In particular, different parameterizations will likely be necessary for older and thicker sea ice, including brash ice, based on measurements in those conditions.

Chapter 5

CONCLUSIONS

5.1 Summary

The marginal ice zone is a challenging environment in which to make observations, and observations during the autumn freeze-up are particularly rare. This dissertation contributes to two main gaps in understanding: the influence of waves on sea ice formation, and the impact of sea ice on waves and turbulence. The use of unique tools to observe the 'new Arctic' in autumn during the Sea State program provided insight into such wave-ice interactions. Chapter 2 used a shipboard stereo video system to evaluate models for pancake sea ice growth mechanisms. In Chapter 3, a sea ice melt episode was described using a large suite of measurements characterizing the atmosphere, sea ice, and ocean. Chapter 4 described the combined effect of the resulting sea ice and waves on near-surface turbulence generation. The main findings from analysis of these observations are summarized here.

In Chapter 2, [*Smith and Thomson*, submitted] simultaneous estimates of wave and pancake sea ice motion were used to show that relative ice motion can be described well by the existing models. Shipboard stereo video resolves spatial and temporal changes in the wave field, and is also used to quantify sea ice motion over time. The relative motion of sea ice is typically an order of magnitude smaller than the mean orbital motion.

The results of this chapter provide important quantification of pancake growth, as observations of pancake sea ice are becoming more common [*Thomson et al.*, 2017]. The rate of lateral growth can be parameterized using the provided models with wave parameters and skin temperature. Coupled wave-ice-ocean models that include floe size distribution [*Roach et al.*, 2018a, i.e.] may be able to predict and model pancake formation in the future. Additionally, the models tested may be used to improve estimates of wave attenuation, as the turbulence generated by relative motion of ice likely accounts for a majority of wave energy loss.

Chapter 3 [*Smith et al.*, 2018a] used a variety of observations spanning the atmosphere-ice-ocean system to describe coupled changes in the ice and ocean resulting from a high wind and wave event. Measurements centered on both the Eulerian and Lagrangian reference

frames were used to produce consistent heat and salt budgets. Despite strong losses of ocean heat to the atmosphere, a significant amount of new pancake sea ice was melted by mixing of ocean heat to the surface.

The evolution observed during the event in Chapter 3 is likely indicative of the effect the changing wave climate and stored solar heat will have in the western Arctic Ocean. Compared to prior observations showing melt of multi-year sea ice by entrainment of the near surface temperature maximum [*Jackson et al.*, 2012; *Timmermans*, 2015], the heat fluxes during this event were much larger and more rapid. The large waves, which reached nearly 5 m, enhanced ocean mixing levels above those resulting from wind alone. While almost all of the heat entrained under multi-year floes went into ice melt, only 30-40% contributed to sea ice melt under the pancake ice, with the remainder released to the atmosphere.

Chapter 4 [*Smith and Thomson*, 2019] used measurements of near-surface turbulence in a range of wind, wave, and new ice conditions to show that the amount of near-surface turbulence across the marginal ice zone can be parameterized using a relevant wind input velocity. The speed of the wind input velocity is related to the speed of the primary roughness elements. When waves are present, they provide the roughness for wind input and the input velocity can be adjusted using bulk wave height and ice characteristics. When ice coverage is high and waves are small, wind is input through the ice, and the relative ice-ocean velocity is the relevant velocity scale.

The results of Chapter 4 indicate that the majority of the observed turbulence can be accounted for by local wind input. In combination with the results from Chapter 2, this suggests that the steepening of the waves by local wind input maintains wave attenuation by generation of turbulence. An important consequences of this result is implied larger gas exchange in marginal ice zones with waves, as the gas transfer is primarily controlled by the turbulent kinetic energy dissipation rate [*Bigdeli et al.*, 2018].

5.2 Implications & Future Directions

A key message of this thesis is that surface waves are important to a variety of processes in the Arctic Ocean MIZ during the autumn. Waves increase ice-ocean interaction, by driving relative motion between the two and enhancing mixing of water from below the mixed layer. They additionally increase the atmosphere-ocean interaction, by resulting in larger near-surface turbulence than when waves are not present. Wave-ice interaction processes, including those described here, are important to quantify in order to understand the seasonal evolution of the Arctic system.

5.2.1 Wave attenuation in new ice

This work has partially addressed the question of what mechanisms dominate attenuation of waves in pancake and frazil ice. In Chapter 2, rough estimates of dissipation due to floe-floe collisions showed that it was orders of magnitude lower than observed dissipation of wave energy. However, the dissipation due to ice-ocean turbulence accounts for a large portion of wave attenuation, in agreement with recent work by *Voermans et al.* [2019]. This process is likely maintained by the wind input, which was shown in Chapter 4 to be approximately in balance with turbulent dissipation rates. The wind and waves are inevitably correlated; the known equilibrium of wind and waves in open water is likely to persist in the MIZ, albeit with modulation by the ice.

A suggested next step is to create an energy budget for the near-surface of the marginal ice zone that simultaneously considers the wind and the waves. *Voermans et al.* [2019] presented a simplified budget, in which all the dissipation in the near surface was assumed to be a result of wave energy dissipation. While there was strong correlation between the two, the turbulent dissipation was on average 1.5-2 times larger than that required to explain the observed wave energy loss. The dissipation of turbulence in the near-surface is likely a result of both local wind input and attenuation of non-local wind energy. In particular, it may be illuminating to begin by more closely examining the evolution of near-surface turbulence

as a function of wind and waves throughout Wave Experiment 3 (which was the subject of Chapter 3). Insights from this experiment may then be used to expand to a more generalized budget for the entire Sea State dataset.

The current state-of-the-art for forecasting waves in sea ice covered regions uses data-driven models to predict frequency-dependent wave attenuation. Although these models are able to reproduce trends in areas similar to those where observations have been made, they are not reliable unless adequately calibrated. In order to improve predictions, we need better parameterizations for the relevant mechanisms with thorough tuning. The work in Chapters 2 and 4 present approaches for parameterizing ice-ocean turbulence, floe-floe collisions, and wind input, but additional observations are needed to parameterize remaining mechanisms.

5.2.2 Autumn ice melt

The increase in wave energy with decreasing ice cover [*Thomson et al.*, 2018; *Li et al.*, 2019b] may suggest that melt events like that described in Chapter 3 will become more common in future Arctic autumns. *Timmermans et al.* [2018] has recently found that the upper ocean heat content in the Beaufort Sea has nearly doubled over the last three decades. The fate of this upper ocean heat was a major motivation for a recent ONR research program, 'Stratified Ocean Dynamics of the Arctic' (SODA). Observations of near-surface mixing and heat evolution from the process cruise in September 2018 may be used to understand the relative role of wind and waves in mixing heat to the surface.

Additionally, analysis of satellite sea ice observations and wind and wave model reanalysis could be used to explore how often heat release might cause autumn ice retreat events. This may help to determine the probability of autumn sea ice retreat events, and correlation with surface conditions. The near-surface ocean is currently not well enough resolved to allow prediction from coupled models. Future improvement of high-resolution regional Arctic models may allow forecasting of these events.

5.2.3 Observational needs

One of the take-aways from this and other recent work is that the waves and sea ice are often tightly coupled in the MIZ. Autonomous and remote methods for observing waves in sea ice have been well validated, but a reliable method for characterizing sea ice over time and space remains a key challenge. Improvements in sea ice observation techniques are critical to furthering our understanding of waves in sea ice. Satellite remote sensing is able to quantify sea ice concentration [*Labe and National Center for Atmospheric Research Staff* , 11 Sep 2017], and improvements are being made in measuring of thickness [*Ricker et al.*, 2017; *Tietsche et al.*, 2018], but the resolution of these products are unlikely to be able to capture the small-scale variation necessary for process studies. Local remote sensing platforms such as UAVs [*Li et al.*, 2019b; *Williams et al.*, 2016] have been successful at using visible imagery to classify and calculate coverage of local sea ice covers. Paired deployments of UAVs and autonomous ocean platforms could provide unparalleled opportunities for characterization of local conditions. The addition of other sensors to these platforms, such as stereo or IR cameras, may be able to measure thickness and other ice properties. Alternatively, sea ice thickness may be able to be quantified from buoy based methods, such as acoustic backscatter (similar to the method used in Chapter 4).

Stereo video shows great potential as a tool for observing the spatial and temporal variation of waves in sea ice. The stereo video dataset utilized in Chapter 2 may be used to provide further insight into pancake ice. Tracking individual floes between frames may help constrain how much the motion of individual floes varies from the bulk values used here. Similarly, automated identification of collision events would allow for testing of proposed collision models, such as that in *Herman* [2018]. Further work with stereo instrumentation and processing in sea ice will likely benefit from the progress being made for a range of applications in open ocean applications [e.g., *Benetazzo et al.*, 2018a; *Sutherland and Melville*, 2013]. For example, cameras with larger frame of views, infrared capability, or higher possible sampling rates may improve measurements and resolution of processes. Additionally,

cameras with larger sensors will improve performance in the low-light conditions common in polar environments. With improved resolution, it may be possible to measure thickness of pancake floes (in addition to radius and area) from a stereo camera [*Rohith et al.*, 2009].

Similarly, autonomous systems designed for other open ocean environments are proving promising for study in the new Arctic. The thick ice of the old Arctic is largely gone, and measurements should focus on utilizing new observational platforms that are better adapted to the thinner ice conditions that are now prevalent. Successful recent deployments of Liquid Robotics Wavegliders and v4 SWIFT buoys in the Arctic have demonstrated the utility of autonomous systems for observing processes at the air-sea-ice interface [*Lee et al.*, 2017]. Additional adaptation of these instruments to address the extreme temperatures and icing conditions of the Arctic would allow for even greater spatial and temporal coverage than is traditionally possible from ship-based systems.

5.2.4 Antarctic sea ice

Although the focus of this work has been on understanding the importance of waves as a new feature in the Arctic Ocean, many of the processes can be expected to apply to sea ice-covered areas in the Antarctic as well. Due to the strong wave climate of the Southern Ocean, waves and pancake ice have long been common in the Antarctic MIZ [*Lange et al.*, 1989]. As waves and sea ice floes both tend to be much larger in the Antarctic, stereo video observations here will be useful for validation of models for pancake ice motion across a broader parameter space. Typical Antarctic wave and ice characteristics suggest that relative ice motions should be larger, and so more wave attenuation through generation of turbulence may occur. Collisions are still not likely to be a significant source of attenuation, but they clearly play an important role in the formation and growth of pancake ice.

The mechanisms associated with waves in sea ice may be particularly important for understanding coastal polynyas, a number of which exist along the Antarctic coastlines. Coastal polynyas are hotspots for sea ice production as a result of the cold temperatures and strong katabatic winds. The role of waves in Antarctic polynyas may be studied in the future

using a dataset I collected in April-May 2017 in the Terra Nova Bay polynya. SWIFT buoys were deployed during and after katabatic wind events in the polynya. In particular, one deployment during the peak of a katabatic wind event started with the buoy approximately 25 km from the coast in open water, and drifted with the wind and waves over about 12 hours into recently formed sea ice about 65 km from the coast. Winds were between 15-20 m/s at 1-meter height throughout the event (Fig. 5.1). Preliminary analysis shows that the waves were smaller than expected based on classic fetch scalings by the end of the deployment (Fig. 5.1). This is likely explained by the increase of ice along the deployment track, which was thickening and consolidating by the time of recovery. The decline of the winds over the deployment period explain a small part of this result, but that is mostly accounted for in the nondimensionalization. Throughout the entire event, the wave period was larger than predicted by classic scalings. This is likely due to the preferential attenuation of high frequencies by the newly formed ice, and may be enhanced by the extreme wind conditions. In these types of conditions, the waves are expected to be driving the rapid formation and growth of pancake sea ice. Additionally, waves are expected to transport ice away from the polynya, allowing for continuous production of sea ice for the duration of wind events.

Although the MLD in the Antarctic is typically much deeper than in the Arctic, the event described in Chapter 3 likely has analogies for the large, Southern Ocean waves at the ice edge that can erode into the warm circumpolar deep water below. Stokes drift effects are strongest in the Southern Ocean [*Li et al.*, 2016] and are predicted to increase under future climate scenarios [*Breivik et al.*, 2019]. As a result, wave forcing in the Southern Ocean near the ice edge accounts for a significant amount of mixed layer deepening. *D'Asaro et al.* [2014] found that wave forcing via Langmuir Turbulence increases the depth by 10-25% in the winter, when the MLD is typically around 100-150 meters. Wave activity is high and stratification is somewhat weaker during this period, and as a result, waves play a much larger role in deepening the mixed layer. During this period in particular, warmer water trapped beneath the mixed layer may stall ice growth if entrained [*Dong et al.*, 2008].

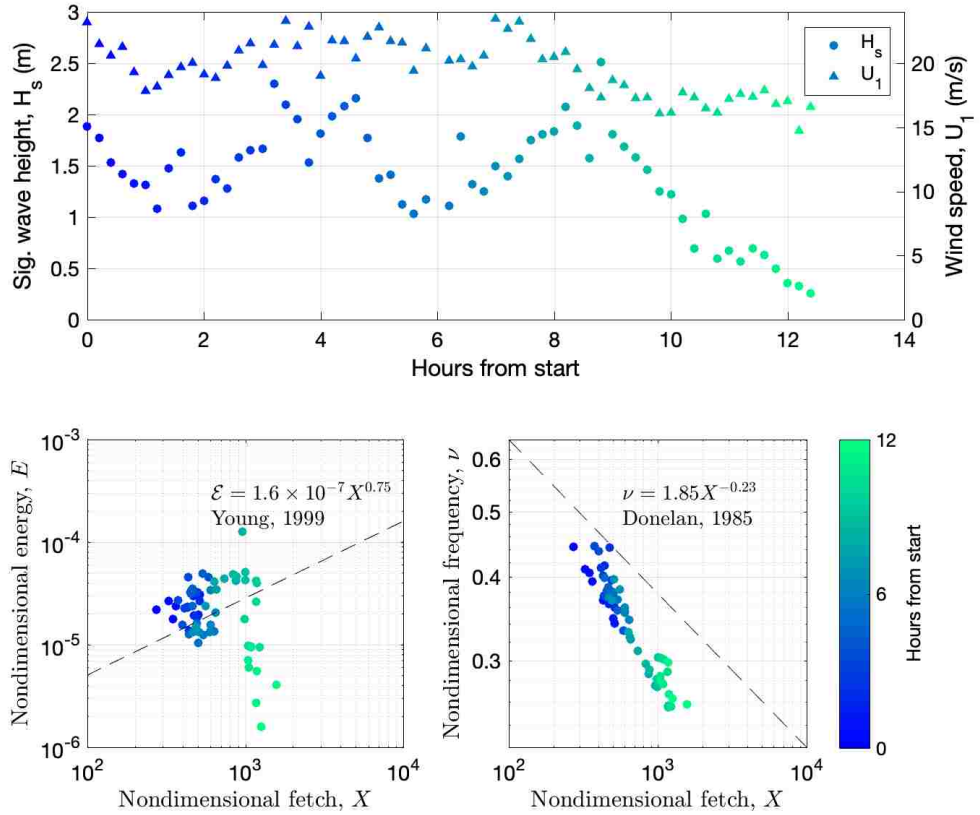

Figure 5.1: Preliminary analysis of SWIFT buoy observations during katabatic wind event in Terra Nova Bay polynya. Upper panel shows time series of significant wave height (circles) and wind speed at 1-m (triangles). Bottom plots show comparison of nondimensional fetch with nondimensional wave parameters compared to classic open water scalings [dashed lines; *Young*, 1999; *Donelan et al.*, 1985]. Colors show hours since beginning of deployment.

5.2.5 Final thoughts

Clearly, many open questions remain regarding the role of waves and mixing in autumn in Polar Oceans, and more generally about interactions at the air-ice-ocean interface. In the future, I plan to examine how heat is input through the ice and into the ocean during the summer season in the Arctic Ocean. Heat absorption throughout summer has important implications for summer ice melt, as well as determining the trajectory of autumn freeze-up. Integrating modeling with observations will allow us to make targeted observations addressing the largest needs identified to advance coupled models of the Arctic system.

BIBLIOGRAPHY

Abraham, C., N. Steiner, A. Monahan, and C. Michel, Effects of subgrid-scale snow thickness variability on radiative transfer in sea ice, *Journal of Geophysical Research: Oceans*, *120*(8), 5597–5614, 2015.

Agrawal, Y., E. Terray, M. Donelan, P. Hwang, A. Williams III, W. Drennan, K. Kahma, and S. Krtaigorodskii, Enhanced dissipation of kinetic energy beneath surface waves, *Nature*, *359*(6392), 219, 1992.

Alari, V., J. Staneva, O. Breivik, J. Bidlot, K. Mogensen, and P. Janssen, Surface wave effects on water temperature in the baltic sea: simulations with the coupled nemo-wam model, *Ocean Dynamics*, *66*, 917–930, 2016.

Alberello, A., M. Onorato, L. Bennetts, M. Vichi, C. Eayrs, K. MacHutchon, and A. Toffoli, Brief communication: Pancake ice floe size distribution during the winter expansion of the antarctic marginal ice zone, *The Cryosphere*, *13*(1), 41–48, 2019.

Anderson, D. L., Growth rate of sea ice, *Journal of Glaciology*, *3*(30), 1170–1172, 1961.

Andreas, E. L., T. W. Horst, A. Grachev, P. O. G. Persson, C. W. Fairall, P. S. Guest, and R. E. Jordan, Parameterising turbulent exchange over summer sea ice and the marginal ice zone, *Quart. J. Roy. Meteor. Soc.*, *136B*, 927–943, 2010.

Ardhuin, F., P. Sutherland, M. Doble, and P. Wadhams, Ocean waves across the arctic: Attenuation due to dissipation dominates over scattering for periods longer than 19 s, *Geophysical Research Letters*, *43*(11), 5775–5783, 2016.

Arntsen, A. E., A. J. Song, D. K. Perovich, and J. A. Richter-Menge, Observations of the

summer breakup of an Arctic sea ice cover, *Geophys. Res. Lett.*, *42*(19), 8057–8063, doi: 10.1002/2015GL065224, 2015.

Asplin, M. G., R. Galley, D. G. Barber, and S. Prinsenberg, Fracture of summer perennial sea ice by ocean swell as a result of arctic storms, *Journal of Geophysical Research: Oceans*, *117*(C6), doi:10.1029/2011JC007221, 2012.

Asplin, M. G., R. Scharien, B. Else, S. Howell, D. G. Barber, T. Papakyriakou, and S. Prinsenberg, Implications of fractured arctic perennial ice cover on thermodynamic and dynamic sea ice processes, *Journal of Geophysical Research: Oceans*, *119*(4), 2327–2343, doi:10.1002/2013JC009557, 2014.

Asplin, M. G., D. B. Fissel, T. N. Papakyriakou, and D. G. Barber, Synoptic climatology of the southern beaufort sea troposphere with comparisons to surface winds, *Atmosphere-Ocean*, *53*(2), 264–281, doi:https://doi.org/10.1080/07055900.2015.1013438, 2015.

Axell, L. B., Wind-driven internal waves and langmuir circulations in a numerical ocean model of the southern baltic sea, *Journal of Geophysical Research: Oceans*, *107*(C11), 2002.

Barry, R. G., The parameterization of surface albedo for sea ice and its snow cover, *Progress in Physical Geography*, *20*(1), 63–79, 1996.

Barthélemy, A., T. Fichefet, H. Goosse, and G. Madec, Modeling the interplay between sea ice formation and the oceanic mixed layer: Limitations of simple brine rejection parameterizations, *Ocean Modelling*, *86*, 141–152, doi:https://doi.org/10.1016/j.ocemod.2014.12.009, 2015.

Benetazzo, A., B. Francesco, B. Filippo, C. Sandro, and S. Mauro, Space-time extreme wind waves: Analysis and prediction of shape and height, *Ocean Modelling*, *113*, 201–216, 2017.

Benetazzo, A., F. Bergamasco, J. Yoo, L. Cavaleri, S.-S. Kim, L. Bertotti, F. Barbariol, and J.-S. Shim, Characterizing the signature of a spatio-temporal wind wave field, *Ocean Modelling*, *129*, 104–123, 2018a.

Benetazzo, A., F. Serafino, F. Bergamasco, G. Ludeno, F. Ardhuin, P. Sutherland, M. Sclavo, and F. Barbariol, Stereo imaging and x-band radar wave data fusion: An assessment, *Ocean Engineering*, *152*, 346–352, 2018b.

Bennetts, L. G., S. O'Farrell, and P. Uotila, Brief communication: Impacts of ocean-wave-induced breakup of Antarctic sea ice via thermodynamics in a stand-alone version of the CICE sea-ice model, *Cryosphere*, *11*(3), 1035–1040, doi:10.5194/tc-11-1035-2017, 2017.

Benschop, H., Windsnelheidsmetingen op zeestations en kuststations: herleiding waarden windsnelheid naar 10-meter niveau, *Koninklijk Nederlands Meteorologisch Instituut Technical Report*, *188*, 1996.

Bigdeli, A., T. Hara, B. Loose, and A. Nguyen, Wave attenuation and gas exchange velocity in marginal sea ice zone, *Journal of Geophysical Research: Oceans*, *123*(3), 2293–2304, 2018.

Bitz, C., and G. Roe, A mechanism for the high rate of sea ice thinning in the arctic ocean, *Journal of Climate*, *17*(18), 3623–3632, 2004.

Brainerd, K. E., and M. C. Gregg, Surface mixed and mixing layer depths, *Deep Sea Research Part I: Oceanographic Research Papers*, *42*(9), 1521–1543, 1995.

Breivik, Ø., A. Carrasco, J. Staneva, A. Behrens, A. Semedo, J.-R. Bidlot, and O. J. Aarnes, Global stokes drift climate under the rcp8. 5 scenario, *Journal of Climate*, *32*(6), 1677–1691, 2019.

Campbell, A. J., A. J. Bechle, and C. H. Wu, Observations of surface waves interacting with ice using stereo imaging, *Journal of Geophysical Research: Oceans*, *119*(6), 3266–3284, 2014.

Carmack, E., et al., Toward quantifying the increasing role of oceanic heat in sea ice loss in the new arctic, *Bulletin of the American Meteorological Society*, *96*(12), 2079–2105, doi:https://doi.org/10.1175/BAMS-D-13-00177.1, 2015.

Cheng, S., et al., Calibrating a viscoelastic sea ice model for wave propagation in the Arctic fall marginal ice zone, *Journal of Geophysical Research: Oceans*, *122*(11), 8770–8793, 2017.

Collet, J.-F. J.-F., Some Modelling Issues in the Theory of Fragmentation-Coagulation Systems, *Commun. Math. Sci.*, *2*(1), 35–54, 2004.

Collins, C., M. Doble, B. Lund, and M. Smith, Observations of surface wave dispersion in the marginal ice zone, *Journal of Geophysical Research: Oceans*, *123*(5), 3336–3354, 2018.

Collins, C. O., W. E. Rogers, A. Marchenko, and A. V. Babanin, In situ measurements of an energetic wave event in the arctic marginal ice zone, *Geophysical Research Letters*, *42*(6), 1863–1870, doi:10.1002/2015GL063063, 2015.

Collins III, C., et al., Doppler correction of wave frequency spectra measured by underway vessels, *Journal of Atmospheric and Oceanic Technology*, *34*(2), 429–436, doi:https://doi.org/10.1175/JTECH-D-16-0138.1, 2017.

Comiso, J. C., C. L. Parkinson, R. Gersten, and L. Stock, Accelerated decline in the arctic sea ice cover, *Geophysical research letters*, *35*(1), 2008.

Craig, P. D., and M. L. Banner, Modeling wave-enhanced turbulence in the ocean surface layer, *Journal of Physical Oceanography*, *24*(12), 2546–2559, 1994.

Cronin, M. F., N. A. Pelland, S. R. Emerson, and W. R. Crawford, Estimating diffusivity from the mixed layer heat and salt balances in the north pacific, *Journal of Geophysical Research: Oceans*, *120*(11), 7346–7362, doi:10.1002/2015JC011010, 2015.

Cronin, M. F., et al., Formation and erosion of the seasonal thermocline in the kuroshio

extension recirculation gyre, *Deep Sea Research Part II: Topical Studies in Oceanography*, *85*, 62–74, doi:https://doi.org/10.1016/j.dsr2.2012.07.018, 2013.

Dai, H.-J., J. C. McWilliams, and J.-H. Liang, Wave-driven mesoscale currents in a marginal ice zone, *Ocean Modelling*, 2018.

D'Asaro, E. A., Turbulence in the upper-ocean mixed layer, *Annual review of marine science*, *6*, 101–115, 2014.

D'Asaro, E. A., J. Thomson, A. Y. Shcherbina, R. R. Harcourt, M. F. Cronin, M. A. Hemer, and B. Fox-Kemper, Quantifying upper ocean turbulence driven by surface waves, *Geophysical Research Letters*, *41*, 1–6, doi:10.1002/2013GL058193, 2014.

De Carolis, G., and D. Desiderio, Dispersion and attenuation of gravity waves in ice: a two-layer viscous fluid model with experimental data validation, *Physics Letters A*, *305*(6), 399–412, 2002.

De La Rosa, S., Temporal changes of sea ice affected by waves and thermal forcing, Master's thesis, University of Bergen, 2011.

De La Rosa, S., S. Maus, and S. Kern, Thermodynamic investigation of an evolving grease to pancake ice field, *Ann. Glaciol.*, *52*(57), 206–214, 2011.

Dee, D. P., et al., The ERA-Interim reanalysis: Configuration and performance of the data assimilation system, *Quarterly Journal of the royal meteorological society*, *137*(656), 553–597, 2011.

Deng, Z., L. Xie, T. Yu, S. Shi, J. Jin, and K. Wu, Numerical study of the effects of wave-induced forcing on dynamics in ocean mixed layer, *Advances in Meteorology*, *2013*, 2013.

Doble, M. J., Simulating pancake and frazil ice growth in the Weddell Sea: A process model from freezing to consolidation, *J. Geophys. Res. Ocean.*, *114*(C9), n/a–n/a, doi:10.1029/2008JC004935, 2009.

Doble, M. J., and J.-R. Bidlot, Wave buoy measurements at the Antarctic sea ice edge compared with an enhanced ECMWF WAM: Progress towards global waves-in-ice modelling, *Ocean Modelling*, *70*, 166–173, 2013.

Doble, M. J., and P. Wadhams, Dynamical contrasts between pancake and pack ice, investigated with a drifting buoy array, *J. Geophys. Res. Ocean.*, *111*(11), 1–11, doi: 10.1029/2005JC003320, 2006.

Doble, M. J., M. D. Coon, and P. Wadhams, Pancake ice formation in the Weddell Sea, *J. Geophys. Res. Ocean.*, *108*(C7), n/a———n/a, doi:10.1029/2002JC001373, 2003.

Doble, M. J., G. De Carolis, M. H. Meylan, J.-R. Bidlot, and P. Wadhams, Relating wave attenuation to pancake ice thickness, using field measurements and model results, *Geophysical Research Letters*, *42*(11), 4473–4481, 2015.

Donelan, M. A., J. Hamilton, and W. Hui, Directional spectra of wind-generated ocean waves, *Philosophical Transactions of the Royal Society of London. Series A, Mathematical and Physical Sciences*, *315*(1534), 509–562, 1985.

Dong, S., J. Sprintall, S. T. Gille, and L. Talley, Southern ocean mixed-layer depth from argo float profiles, *Journal of Geophysical Research: Oceans*, *113*(C6), 2008.

Eicken, H., M. Lensu, M. Leppäranta, W. Tucker, A. Gow, and O. Salmela, Thickness, structure, and properties of level summer multiyear ice in the eurasian sector of the arctic ocean, *Journal of Geophysical Research: Oceans*, *100*(C11), 22,697–22,710, doi:10.1029/95JC02188, 1995.

Endoh, T., T. Matsuno, Y. Yoshikawa, and E. Tsutsumi, Estimates of the turbulent kinetic energy budget in the oceanic convective boundary layer, *Journal of oceanography*, *70*(1), 81–90, 2014.

Euskirchen, E. S., E. S. Goodstein, and H. P. Huntington, An estimated cost of lost climate regulation services caused by thawing of the arctic cryosphere, *Ecological applications*, *23*(8), 1869–1880, 2013.

Fairall, C. W., E. F. Bradley, D. P. Rogers, J. B. Edson, and G. S. Young, Bulk parameterization of air-sea fluxes for tropical ocean-global atmosphere coupled-ocean atmosphere response experiment, *Journal of Geophysical Research: Oceans*, *101*(C2), 3747–3764, 1996.

Fairall, C. W., E. F. Bradley, J. E. Hare, A. Grachev, and J. B. Edson, Bulk parametrization of air-sea fluxes: Updates and verification for the coare algorithm, *J. Climate*, *16*, 571–591, 2003.

Fer, I., A. K. Peterson, A. Randelhoff, and A. Meyer, One-dimensional evolution of the upper water column in the atlantic sector of the arctic ocean in winter, *Journal of Geophysical Research: Oceans*, 2017.

Filbet, F., and P. Laurençot, Numerical simulation of the Smoluchowski coagulation equation, *SIAM Journal on Scientific Computing*, *25*(6), 2004–2028, doi:10.1137/S1064827503429132, 2004.

Forristall, G. Z., Measurements of a saturated range in ocean wave spectra, *Journal of Geophysical Research: Oceans*, *86*(C9), 8075–8084, doi:10.1029/JC086iC09p08075, 1981.

Gallaher, S. G., T. P. Stanton, W. J. Shaw, S. T. Cole, J. M. Toole, J. P. Wilkinson, T. Maksym, and B. Hwang, Evolution of a Canada Basin ice-ocean boundary layer and mixed layer across a developing thermodynamically forced marginal ice zone, *Journal of Geophysical Research: Oceans*, *121*(8), 6223–6250, doi:10.1002/2016JC011778, 2016.

Galley, R., D. Babb, M. Ogi, B. Else, N.-X. Geilfus, O. Crabeck, D. G. Barber, and S. Rysgaard, Replacement of multiyear sea ice and changes in the open water season duration in the beaufort sea since 2004, *Journal of Geophysical Research: Oceans*, *121*(3), 1806–1823, 2016.

Geer, I. W., *Glossary of Weather and Climate with Related Oceanic and Hydrologic Terms.*, 272 pp, American Meteorological Society, 1996.

Gemmrich, J., T. Mudge, and V. Polonichko, On the energy input from wind to surface waves, *Journal of Physical Oceanography*, *24*(11), 2413–2417, 1994.

Gemmrich, J., W. E. Rogers, J. Thomson, and S. Lehner, Wave evolution in off-ice wind conditions, *Journal of Geophysical Research: Oceans*, *123*(8), 5543–5556, 2018.

Gemmrich, J. R., and D. M. Farmer, Near-surface turbulence in the presence of breaking waves, *Journal of Physical Oceanography*, *34*(5), 1067–1086, 2004.

Gent, P. R., et al., The community climate system model version 4, *Journal of Climate*, *24*(19), 4973–4991, doi:https://doi.org/10.1175/2011JCLI4083.1, 2011.

Grachev, A., E. L. Andreas, C. W. Fairall, P. S. Guest, and P. O. G. Persson, Sheba flux-profile relationships in the stable atmospheric boundary layer, *Boundary-Layer Meteor.*, *124*(3), 315–222, 2007.

Grare, L., L. Lenain, and W. K. Melville, Vertical profiles of the wave-induced airflow above ocean surface waves, *Journal of Physical Oceanography*, *48*(12), 2018.

Grotmaack, R., and M. H. Meylan, Wave forcing of small floating bodies, *Journal of waterway, port, coastal, and ocean engineering*, *132*(3), 192–198, 2006.

Guest, P., P. O. G. Persson, S. Wang, M. Jordan, Y. Yin, B. Blomquist, C. Fairall, and D. Price, Low-level baroclinic jets over the new arctic ocean, *Journal of Geophysical Research: Oceans*, 2018.

Guest, P. S., and K. L. Davidson, The aerodynamic roughness of different types of sea ice, *Journal of Geophysical Research*, *96*(C3), 4709–4721, 1991.

Hasselmann, K., Measurements of wind wave growth and swell decay during the joint north sea wave project (jonswap), *Dtsch. Hydrogr. Z.*, *8*, 95, 1973.

Herbers, T. H. C., P. F. Jessen, T. T. Janssen, D. B. Colbert, and J. H. MacMahan, Observing ocean surface waves with GPS-tracked buoys, *J. Atmos. Ocean Tech.*, *29*, 944–959, 2012a.

Herbers, T. H. C., P. F. Jessen, T. T. Janssen, D. B. Colbert, and J. H. MacMahan, Observing ocean surface waves with gps-tracked buoys, *Journal of Atmospheric and Oceanic Technology*, *29*, 944–959, doi:https://doi.org/10.1175/JTECH-D-11-00128.1, 2012b.

Herman, A., Molecular-dynamics simulation of clustering processes in sea-ice floes, *Physical Review E*, *84*(5), 056,104, 2011.

Herman, A., Numerical modeling of force and contact networks in fragmented sea ice, *Annals of Glaciology*, *54*(62), 114–120, 2013.

Herman, A., Wave-induced surge motion and collisions of sea ice floes: Finite-floe-size effects, *Journal of Geophysical Research: Oceans*, *123*(10), 7472–7494, 2018.

Horvat, C., and E. Tziperman, A prognostic model of the sea-ice floe size and thickness distribution, *Cryosphere*, *9*(6), 2119–2134, doi:10.5194/tc-9-2119-2015, 2015.

Horvat, C., and E. Tziperman, The evolution of scaling laws in the sea ice floe size distribution, *J. Geophys. Res. Ocean.*, *122*(9), 7630–7650, doi:10.1002/2016JC012573, 2017.

Hunke, E. C., W. H. Lipscomb, and A. K. Turner, Sea-ice models for climate study: retrospective and new directions, *Journal of Glaciology*, *56*(200), 1162–1172, 2010.

Hunke, E. C., W. H. Lipscomb, A. K. Turner, N. Jeffery, and S. Elliott, CICE: the Los Alamos Sea Ice Model Documentation and Software User's Manual Version 5.1 LA-CC-06-012, *Tech. rep.*, Los Alamos National Laboratory, 2015.

Hwang, B., J. Wilkinson, T. Mayksm, H. C. Graber, and A. Schweiger, Winter-to-summer transition of Arctic sea ice breakup and floe size distribution in the Beaufort Sea during 2014 ONR MIZ experiment, *Elem Sci Anth*, *In Review*, 2017.

Itseez, Open Source Computer Vision Library https://github.com/itseez/opencv, 2015.

Ivanov, V., V. Alexeev, N. V. Koldunov, I. Repina, A. B. Sandø, L. H. Smedsrud, and A. Smirnov, Arctic ocean heat impact on regional ice decay: A suggested positive feedback, *Journal of Physical Oceanography*, *46*(5), 1437–1456, doi:https://doi.org/10.1175/JPO-D-15-0144.1, 2016.

Jackson, J. M., S. E. Allen, F. McLaughlin, R. Woodgate, and E. Carmack, Changes to the near-surface waters in the canada basin, arctic ocean from 1993–2009: A basin in transition, *Journal of Geophysical Research: Oceans*, *116*(C10), doi:10.1029/2011JC007069, 2011.

Jackson, J. M., W. J. Williams, and E. C. Carmack, Winter sea-ice melt in the canada basin, arctic ocean, *Geophysical Research Letters*, *39*(3), doi:10.1029/2011GL050219, 2012.

Jackson, M., E. C. Carmack, F. A. McLaughlin, S. E. Allen, and R. G. Ingram, Identification, characterization, and change of the near-surface temperature maximum in the canada basin, 1993-2008, *Journal of Geophysical Research: Oceans*, *115*, doi:10.1029/2009JC005265, 2010.

Jeffries, M. O., J. E. Overland, and D. K. Perovich, The arctic shifts to a new normal, *Physics Today*, *66*(10), 35–40, 2013.

Jones, N., Pancake ice takes over the Arctic, doi:10.1038/news.2009.183, 2009.

Josberger, E. G., and S. Martin, A laboratory and theoretical study of the boundary layer adjacent to a vertical melting ice wall in salt water, *Journal of Fluid Mechanics*, *111*, 439–473, 1981.

Kantha, L. H., A numerical model of Arctic leads, *J. Geophys. Res. Ocean.*, *100*(C3), 4653–4672, 1995.

Kantha, L. H., and C. A. Clayson, On the effect of surface gravity waves on mixing in the oceanic mixed layer, *Ocean Modelling*, *6*(2), 101–124, 2004.

Kenyon, K. E., Stokes drift for random gravity waves, *Journal of Geophysical Research*, *74*(28), 6991–6994, 1969.

Khandekar, M., Inertial oscillations in floe motion over the beaufort sea-observations and analysis, *Atmosphere-Ocean*, *18*(1), 1–14, doi:https://doi.org/10.1080/07055900.1980.9649073, 1980.

Kohout, A., M. Williams, S. Dean, and M. Meylan, Storm-induced sea-ice breakup and the implications for ice extent, *Nature*, *509*(7502), 604, 2014.

Kohout, A. L., and M. H. Meylan, An elastic plate model for wave attenuation and ice floe breaking in the marginal ice zone, *Journal of Geophysical Research: Oceans*, *113*(C9), n/a–n/a, doi:10.1029/2007JC004434, 2008.

Kohout, A. L., M. H. Meylan, and D. R. Plew, Wave attenuation in a marginal ice zone due to the bottom roughness of ice floes, *Annals of Glaciology*, *52*(57), 118–122, 2011.

Kottmeier, C., and D. Engelbart, Generation and atmospheric heat exchange of coastal polynyas in the weddell sea, *Boundary-Layer Meteorology*, *60*(3), 207–234, 1992.

Krishfield, R., J. Toole, A. Proshutinsky, and M.-L. Timmermans, Automated ice-tethered profilers for seawater observations under pack ice in all seasons, *Journal of Atmospheric and Oceanic Technology*, *25*(11), 2091–2105, doi:https://doi.org/10.1175/2008JTECHO587.1, 2008.

Krishfield, R. A., and D. K. Perovich, Spatial and temporal variability of oceanic heat flux to the arctic ice pack, *Journal of Geophysical Research: Oceans*, *110*(C7), doi:10.1029/2004JC002293, 2005.

Kwok, R., and D. Rothrock, Decline in arctic sea ice thickness from submarine and icesat records: 1958–2008, *Geophysical Research Letters*, *36*(15), doi:10.1029/2009GL039035, 2009.

Labe, Z., and National Center for Atmospheric Research Staff , The climate data guide: Sea ice thickness data sets: Overview and comparison table, 11 Sep 2017.

Lange, M., S. Ackley, P. Wadhams, G. Dieckmann, and H. Eicken, Development of sea ice in the weddell sea, *Annals of Glaciology*, *12*, 92–96, 1989.

Lee, C. M., J. Thomson, M. I. Zone, and A. S. S. Teams, An autonomous approach to observing the seasonal ice zone in the western arctic, *Oceanography*, *30*(2), 56–68, 2017.

Leibovich, S., The form and dynamics of langmuir circulations, *Ann Rev Fluid Mech*, *15*, 391–427, 1983.

Leonard, G., H. S. H., and S. F. Ackley, Dynamic growth of a pancake ice cover, in *Proceedings of 14th International Symposium on Ice: Ice in Surface Waters*, 1998.

Li, H., R. Lubbad, et al., Laboratory study of ice floes collisions under wave action, in *The 28th International Ocean and Polar Engineering Conference*, International Society of Offshore and Polar Engineers, 2018.

Li, J., A. L. Kohout, M. J. Doble, P. Wadhams, C. Guan, and H. H. Shen, Rollover of apparent wave attenuation in ice covered seas, *Journal of Geophysical Research: Oceans*, *122*(11), 8557–8566, 2017.

Li, J., Y. Ma, Q. Liu, W. Zhang, and C. Guan, Growth of wave height with retreating ice cover in the arctic, *Cold Regions Science and Technology*, p. 102790, 2019a.

Li, Q., A. Webb, B. Fox-Kemper, A. Craig, G. Danabasoglu, W. G. Large, and M. Vertenstein, Langmuir mixing effects on global climate: Wavewatch iii in cesm, *Ocean Modelling*, *103*, 145–160, 2016.

Li, T., et al., Resolving fine-scale surface features on polar sea ice: A first assessment of uas photogrammetry without ground control, *Remote Sensing*, *11*(7), 784, 2019b.

Lohrmann, A., T. Pedersen, S. Nylund, and E. Siegel, Waves in the summer ice in the winter, in *Current, Waves and Turbulence Measurements (CWTM), 2011 IEEE/OES 10th*, pp. 150–158, IEEE, 2011.

Loose, B., W. McGillis, P. Schlosser, D. Perovich, and T. Takahashi, Effects of freezing, growth, and ice cover on gas transport processes in laboratory seawater experiments, *Geophysical Research Letters*, *36*(5), doi:10.1029/2008GL036318, 2009.

Loose, B., W. R. McGillis, D. Perovich, C. J. Zappa, and P. Schlosser, A parameter model of gas exchange for the seasonal sea ice zone, *Ocean Science*, *10*(1), 17–28, 2014.

Loose, B., R. P. Kelly, A. Bigdeli, W. Williams, R. Krishfield, M. Rutgers van der Loeff, and S. B. Moran, How well does wind speed predict air-sea gas transfer in the sea ice zone? a synthesis of radon deficit profiles in the upper water column of the a rctic o cean, *Journal of Geophysical Research: Oceans*, *122*(5), 3696–3714, 2017.

Lu, P., Z. Li, B. Cheng, and M. Leppäranta, A parameterization of the ice-ocean drag coefficient, *Journal of Geophysical Research: Oceans*, *116*(C7), 2011.

Lund, B., H. C. Graber, M. Smith, M. Doble, O. Persson, J. Thomson, and P. Wadhams, Arctic sea ice drift measured by shipboard marine radar, *Journal of Geophysical Research: Oceans*, *123*(6), doi:10.1029/2018JC013769, 2018.

Lupkes, C., V. M. Gryanik, J. Hartmann, and E. L. Andreas, A parametrization, based on sea ice morphology, of the neutral atmospheric drag coefficients for weather prediction and climate models, *J. Geophys. Res.*, *117*(D13112), 2012.

Lygre, A., and H. E. Krogstad, Maximum entropy estimation of the directional distribution in ocean wave spectra, *Journal of Physical Oceanography*, *16*(12), 2052–2060, doi:https://doi.org/10.1175/1520-0485(1986)016⟨2052:MEEOTD⟩2.0.CO;2, 1986.

Magnell, B., L. Ivanov, and E. Siegel, Measurements of ice parameters in the Beaufort sea using the Nortek AWAC acoustic Doppler current profiler, in *Proceedings of the Oceans 2010 conference*, MTS/IEEE, Seattle, WA (USA), 2010.

Martinson, D. G., and C. Wamser, Ice drift and momentum exchange in winter Antarctic pack ice, *Journal of Geophysical Research: Oceans*, *95*(C2), 1741–1755, 1990.

Matsumura, Y., and K. I. Ohshima, Lagrangian modelling of frazil ice in the ocean, *Annals of glaciology*, *56*(69), 373–382, 2015.

Maus, S., and S. De La Rosa, Salinity and solid fraction of frazil and grease ice, *Journal of Glaciology*, *58*(209), 594–612, 2012.

Maykut, G., and M. G. McPhee, Solar heating of the arctic mixed layer, *Journal of Geophysical Research: Oceans*, *100*(C12), 24,691–24,703, doi:10.1029/95JC02554, 1995.

Maykut, G. A., Energy exchange over young sea ice in the central arctic, *Journal of Geophysical Research: Oceans*, *83*(C7), 3646–3658, doi:10.1029/JC083iC07p03646, 1978.

Maykut, G. A., The surface heat and mass balance, in *The geophysics of sea ice*, pp. 395–463, Springer, 1986.

Maykut, G. A., and D. K. Perovich, The role of shortwave radiation in the summer decay of a sea ice cover, *J. Geophys. Res. Ocean.*, *92*(C7), 7032–7044, doi:10.1029/JC092iC07p07032, 1987.

McFarlane, V., M. Loewen, and F. Hicks, Measurements of the evolution of frazil ice particle size distributions, *Cold Regions Science and Technology*, *120*, 45–55, 2015.

McLaughlin, F., E. Carmack, A. Proshutinsky, R. A. Krishfield, C. Guay, M. Yamamoto-Kawai, J. M. Jackson, and B. Williams, The rapid response of the canada basin to climate forcing: From bellwether to alarm bells, *Oceanography*, *24*(3), 146–159, doi:http://www.jstor.org/stable/24861309, 2011.

McPhee, M. G., Turbulent heat flux in the upper ocean under sea ice, *Journal of Geophysical Research: Oceans*, *97*(C4), 5365–5379, doi:10.1029/92JC00239, 1992.

McPhee, M. G., and N. Untersteiner, Using sea ice to measure vertical heat flux in the ocean, *Journal of Geophysical Research: Oceans*, *87*(C3), 2071–2074, doi:10.1029/JC087iC03p02071, 1982.

McPhee, M. G., D. G. Martinson, et al., Turbulent mixing under drifting pack ice in the weddell sea, *Science-AAAS-Weekly Paper Edition-including Guide to Scientific Information*, *263*(5144), 218–220, 1994.

McWilliams, J. C., and J. M. Restrepo, The wave-driven ocean circulation, *Journal of Physical Oceanography*, *29*(10), 2523–2540, 1999.

McWilliams, J. C., and P. P. Sullivan, Vertical mixing by langmuir circulations, *Spill Science & Technology Bulletin*, *6*(3), 225–237, 2000.

Meier, W., D. Gallaher, and G. Campbell, New estimates of arctic and antarctic sea ice extent during september 1964 from recovered nimbus i satellite imagery, *The Cryosphere*, *7*(2), 699, 2013.

Meier, W. N., Losing arctic sea ice: observations of the recent decline and the long-term context, *Sea Ice*, pp. 290–303, 2017.

Meier, W. N., et al., Arctic sea ice in transformation: A review of recent observed changes and impacts on biology and human activity, *Reviews of Geophysics*, *52*(3), 185–217, doi:10.1002/2013RG000431, 2014.

Mellor, M., *Properties of snow*, United States Army Corps of Engineers, Cold Regions Research and Engineering Laboratory, 1964.

Metzger, E. J., et al., Us navy operational global ocean and arctic ice prediction systems, *Oceanography*, *27*(3), 32–43, doi:http://www.jstor.org/stable/24862187, 2014.

Meylan, M. H., L. J. Yiew, L. G. Bennetts, B. J. French, and G. A. Thomas, Surge motion of an ice floe in waves: comparison of a theoretical and an experimental model, *Annals of Glaciology*, *56*(69), 155–159, 2015.

Moon, T. A., et al., The expanding footprint of rapid arctic change, *Earth's Future*, 2019.

Morison, J., M. McPhee, T. Curtin, and C. Paulson, The oceanography of winter leads, *Journal of Geophysical Research: Oceans*, *97*(C7), 11,199–11,218, 1992.

Naumann, A., D. Notz, L. Håvik, and A. Sirevaag, Initial sea-ice growth in open water: properties of grease ice and nilas, *The Cryosphere Discussions*, *6*, 125–158, 2012.

Niioka, T., and C. Kohei, Sea ice thickness measurement from an ice breaker using a stereo imaging system consisted of a pairs of high definition video cameras, *International Archives of the Photogrammetry, Remote Sensing and Spatial Information Science, Kyoto Japan*, *38*(8), 1053–1056, 2010.

Noh, Y., H. Ok, E. Lee, T. Toyoda, and N. Hirose, Parameterization of langmuir circulation in the ocean mixed layer model using les and its application to the ogcm, *Journal of Physical Oceanography*, *46*(1), 57–78, 2016.

Ono, N., Thermal properties of sea ice. iii. on the specific heat of sea ice, *Low Temperature Science A*, *24*, 249–58, 1966.

Onstott, R., P. Gogineni, A. Gow, T. Grenfell, K. Jezek, D. Perovich, and C. Swift, Electromagnetic and physical properties of sea ice formed in the presence of wave action, *IEEE Trans. Geosci. Remote Sens.*, *36*(5), 1764–1783, doi:10.1109/36.718644, 1998.

Overeem, I., R. S. Anderson, C. W. Wobus, G. D. Clow, F. E. Urban, and N. Matell, Sea ice loss enhances wave action at the arctic coast, *Geophysical Research Letters*, *38*(17), 2011.

Parkinson, C. L., and J. C. Comiso, On the 2012 record low arctic sea ice cover: Combined

impact of preconditioning and an august storm, *Geophysical Research Letters*, *40*(7), 1356–1361, 2013.

Pellichero, V., J.-B. Sallée, C. C. Chapman, and S. M. Downes, The southern ocean meridional overturning in the sea-ice sector is driven by freshwater fluxes, *Nature communications*, *9*(1), 1789, 2018.

Peralta-Ferriz, C., and R. A. Woodgate, Seasonal and interannual variability of pan-arctic surface mixed layer properties from 1979 to 2012 from hydrographic data, and the dominance of stratification for multiyear mixed layer depth shoaling, *Progress in Oceanography*, *134*, 19–53, doi:https://doi.org/10.1016/j.pocean.2014.12.005, 2015.

Perovich, D. K., Thin and thinner: Sea ice mass balance measurements during SHEBA, *J. Geophys. Res.*, *108*(C3), 8050, doi:10.1029/2001JC001079, 2003.

Perovich, D. K., and C. Polashenski, Albedo evolution of seasonal arctic sea ice, *Geophysical Research Letters*, *39*(8), doi:10.1029/2012GL051432, 2012.

Perovich, D. K., T. C. Grenfell, J. A. Richter-Menge, B. Light, W. B. Tucker, and H. Eicken, Thin and thinner: Sea ice mass balance measurements during sheba, *Journal of Geophysical Research: Oceans*, *108*(C3), 2003.

Perovich, D. K., B. Light, H. Eicken, K. F. Jones, K. Runciman, and S. V. Nghiem, Increasing solar heating of the arctic ocean and adjacent seas, 1979–2005: Attribution and role in the ice-albedo feedback, *Geophysical Research Letters*, *34*(19), doi:10.1029/2007GL031480, 2007.

Perovich, D. K., J. A. Richter-Menge, K. F. Jones, and B. Light, Sunlight, water, and ice: Extreme arctic sea ice melt during the summer of 2007, *Geophysical Research Letters*, *35*(11), doi:10.1029/2008GL034007, 2008.

Persson, P. O. G., Onset and end of the summer melt season over sea ice: Thermal structure and surface energy perspective from SHEBA, *Clim. Dyn.*, *39*, 1349–1371, 2012a.

Persson, P. O. G., Onset and end of the summer melt season over sea ice: Thermal structure and surface energy perspective from sheba, *Clim. Dynamics*, *39*, 1349–1371, doi:https://doi.org/10.1007/s00382-011-1196-9, 2012b.

Persson, P. O. G., C. W. Fairall, E. L. Andreas, P. S. Guest, and D. K. Perovich, Measurements near the atmospheric surface flux group tower at sheba: Near-surface conditions and surface energy budget, *Journal of Geophysical Research: Oceans*, *107*(C10), SHE 21–1–SHE 21–35, doi:10.1029/2000JC000705, 8045, 2002a.

Persson, P. O. G., C. W. Fairall, E. L. Andreas, P. S. Guest, and D. K. Perovich, Measurements near the atmospheric surface flux group tower at sheba: Near-surface conditions and surface energy budget, *J. Geophys. Res.*, *107*(C10), 2002b.

Persson, P. O. G., J. E. Hare, C. W. Fairall, and W. Otto, Air-sea interaction processes in warm and cold sectors of extratropical cyclonic storms observed during fastex, *Quart. J. Roy. Meteor. Soc.*, *131*, 877–912, 2005.

Persson, P. O. G., B. Blomquist, P. Guest, S. Stammerjohn, C. Fairall, L. Rainville, B. Lund, S. Ackley, and J. Thomson, Shipboard observations of the meteorology and near-surface environment during autumn freeze-up in the Beaufort/Chukchi Seas, *Journal of Geophysical Research: Oceans*, 2018a.

Persson, P. O. G., et al., Ice begets ice: Observations of the Arctic Ocean autumn freezeup process, *J. Geophys. Res. Ocean, submitted*, 2018b.

Peters, H., M. Gregg, and J. Toole, Meridional variability of turbulence through the equatorial undercurrent, *Journal of Geophysical Research: Oceans*, *94*(C12), 18,003–18,009, 1989.

Peterson, A. K., I. Fer, M. G. McPhee, and A. Randelhoff, Turbulent heat and momentum fluxes in the upper ocean under arctic sea ice, *Journal of Geophysical Research: Oceans*, 2017.

Pickart, R. S., M. A. Spall, and J. T. Mathis, Dynamics of upwelling in the alaskan beaufort sea and associated shelf-basin fluxes, *Deep Sea Res., Part 1*, *76*(0), 35–51, 2013.

Pierson, W. J., and L. Moskowitz, A proposed spectral form for fully developed wind seas based on the similarity theory of sa kitaigorodskii, *Journal of Geophysical Research*, *69*(24), 5181–5190, doi:10.1029/JZ069i024p05181, 1964.

Plant, W. J., A relationship between wind stress and wave slope, *Journal of Geophysical Research: Oceans*, *87*(C3), 1961–1967, 1982.

Polton, J. A., D. M. Lewis, and S. E. Belcher, The role of wave-induced coriolis–stokes forcing on the wind-driven mixed layer, *Journal of Physical Oceanography*, *35*(4), 444–457, 2005.

Polyakov, I. V., A. V. Pnyushkov, R. Rember, L. Padman, E. C. Carmack, and J. M. Jackson, Winter convection transports atlantic water heat to the surface layer in the eastern arctic ocean, *Journal of Physical Oceanography*, *43*(10), 2142–2155, doi:https://doi.org/10.1175/JPO-D-12-0169.1, 2013.

Price, J. F., R. A. Weller, and R. Pinkel, Diurnal cycling: Observations and models of the upper ocean response to diurnal heating, cooling, and wind mixing, *Journal of Geophysical Research: Oceans*, *91*(C7), 8411–8427, 1986.

Rabault, J., G. Sutherland, A. Jensen, K. H. Christensen, and A. Marchenko, Experiments on wave propagation in grease ice: combined wave gauges and particle image velocimetry measurements, *Journal of Fluid Mechanics*, *864*, 876–898, 2019.

Rainville, L., C. M. Lee, and R. A. Woodgate, Impact of wind-driven mixing in the arctic ocean, *Oceanography*, *24*(3), 136–145, 2011.

Rascle, N., and F. Ardhuin, Drift and mixing under the ocean surface revisited: Stratified conditions and model-data comparison, *Journal of Geophysical Research*, *114*, 2009.

Ricker, R., S. Hendricks, L. Kaleschke, X. Tian-Kunze, J. King, and C. Haas, A weekly arctic sea-ice thickness data record from merged cryosat-2 and smos satellite data, *Cryosphere*, *11*(4), 1607–1623, 2017.

Rind, D., R. Healy, C. Parkinson, and D. Martinson, The role of sea ice in 2× co2 climate model sensitivity. part i: the total influence of sea ice thickness and extent, *Journal of Climate*, *8*(3), 449–463, 1995.

Roach, A., K. Aagaard, and F. Carsey, Coupled ice-ocean variability in the greenland sea, *Atmosphere-Ocean*, *31*(3), 319–337, doi:https://doi.org/10.1080/07055900.1993.9649474, 1993.

Roach, L., C. Horvat, S. M. Dean, and C. M. Bitz, An emergent sea ice floe size distribution in a global coupled ocean – sea ice model, *J. Geophys. Res. Ocean., in prep*, 2018a.

Roach, L. A., S. M. Dean, and J. A. Renwick, Consistent biases in Antarctic sea ice concentration simulated by climate models, *Cryosph. Discuss.*, *2017*, 1–26, doi:10.5194/tc-2017-131, 2017a.

Roach, L. A., S. F. B. Tett, M. J. Mineter, K. Yamazaki, and C. D. Rae, Automated parameter tuning applied to sea ice in a global climate model, *Clim. Dyn.*, doi:10.1007/s00382-017-3581-5, 2017b.

Roach, L. A., M. M. Smith, and S. M. Dean, Quantifying growth of pancake sea ice floes using images from drifting buoys, *Journal of Geophysical Research: Oceans*, *123*(4), 2851–2866, 2018b.

Rogers, W., P. Posey, L. Li, and R. Allard, Forecasting and hindcasting waves in and near the marginal ice zone: Wave modeling and the onr sea state field experiment, *Tech. rep.*, NAVAL RESEARCH LAB STENNIS, 2018.

Rogers, W. E., J. Thomson, H. H. Shen, M. J. Doble, P. Wadhams, and S. Cheng, Dissipation of wind waves by pancake and frazil ice in the autumn beaufort sea, *Journal of Geophysical Research: Oceans*, *121*(11), 7991–8007, doi:10.1002/2016JC012251, 2016.

Rohith, M., G. Somanath, C. Kambhamettu, and C. A. Geiger, Stereo analysis of low textured regions with application towards sea-ice reconstruction., in *IPCV*, pp. 23–29, 2009.

Rothrock, D. A., and A. S. Thorndike, Measuring the sea ice floe size distribution, *J. Geophys. Res. Ocean.*, *89*(C4), 6477–6486, doi:10.1029/JC089iC04p06477, 1984.

Rottier, P. J., Floe pair interaction event rates in the marginal ice zone, *J. Geophys. Res. Ocean.*, *97*(C6), 9391–9400, doi:10.1029/92JC00152, 1992.

Rumer, R. R., R. D. Crissman, and A. Wake, *Ice transport in great lakes*, Great Lakes Environmental Research Laboratory, National Oceanic and . . . , 1979.

Schwendeman, M., and J. Thomson, A horizon-tracking method for shipboard video stabilization and rectification, *Journal of Atmospheric and Oceanic Technology*, *32*(1), 164–176, 2015.

Schwendeman, M. S., and J. Thomson, Sharp-crested breaking surface waves observed from a ship-based stereo video system, *Journal of Physical Oceanography*, *47*(4), 775–792, 2017.

Sellers, W. D., *Heat transfer in soil*, vol. In Physical Climatology, 5th edn ed., University of Chicago Press, 1974.

Serreze, M. C., A. H. Lynch, and M. P. Clark, The arctic frontal zone as seen in the ncep–ncar reanalysis, *Journal of Climate*, *14*(7), 1550–1567, doi:https://doi.org/10.1175/1520-0442(2001)014⟨1550:TAFZAS⟩2.0.CO;2, 2001.

Shen, H. H., Modelling ocean waves in ice-covered seas, *Applied Ocean Research*, *83*, 30–36, 2019.

Shen, H. H., and S. F. Ackley, Laboratory-produced pancake ice cover in a two-dimensional wave field, *Antarctic Journal of the United States*, *30*(5), 106–108, 1995.

Shen, H. H., and S. F. A. Ackley, A one-dimensional model for wave-induced ice-floe collisions, *Ann. Glaciol.*, *15*(1), 87–95, 1991.

Shen, H. H., and V. A. Squire, Wave damping in compact pancake ice fields due to interactions between pancakes, *Antarctic Sea Ice: Physical Processes, Interactions, and Variability*, pp. 325–341, 1998.

Shen, H. H., W. D. Hibler, and M. Leppäranta, The role of floe collisions in sea ice rheology, *J. Geophys. Res. Ocean.*, *92*(C7), 7085–7096, doi:10.1029/JC092iC07p07085, 1987.

Shen, H. H., S. F. Ackley, and M. A. Hopkins, A conceptual model for pancake-ice formation in a wave field, *Ann. Glaciol.*, *33*(2), 361–367, doi:10.3189/172756401781818239, 2001.

Shen, H. H., S. F. Ackley, and Y. Yuan, Limiting diameter of pancake ice, *J. Geophys. Res. Ocean.*, *109*(C12), n/a–n/a, doi:10.1029/2003JC002123, 2004.

Simmonds, I., and K. Keay, Extraordinary september arctic sea ice reductions and their relationships with storm behavior over 1979–2008, *Geophysical Research Letters*, *36*(19), doi:10.1029/2009GL039810, 2009.

Smedsrud, L. H., and R. Skogseth, Field measurements of arctic grease ice properties and processes, *Cold Regions Science and Technology*, *44*(3), 171–183, 2006.

Smith, M., and J. Thomson, Scaling observations of surface waves in the beaufort sea, *Elementa Science of the Anthropocene*, *4*, doi:http://doi.org/10.12952/journal.elementa.000097, 2016.

Smith, M., and J. Thomson, Ocean surface turbulence in newly formed marginal ice zones, *Journal of Geophysical Research: Oceans*, 2019.

Smith, M., S. Stammerjohn, O. Persson, L. Rainville, G. Liu, W. Perrie, R. Robertson, J. Jackson, and J. Thomson, Episodic reversal of autumn ice advance caused by release of ocean heat in the beaufort sea, *Journal of Geophysical Research: Oceans*, doi:10.1002/2018JC013764, 2018a.

Smith, M., S. Stammerjohn, O. Persson, L. Rainville, G. Liu, W. Perrie, and J. Thomson, Storm-driven mixing and episodic reversal of the autumn ice advance in the Beaufort Sea, *J. Geophys. Res. Ocean, submitted*, 2018b.

Smith, M. M., Surface waves in the beaufort sea, Master's thesis, University of Washington, 2016.

Smith, S. D., Coefficients for sea surface wind stress, heat flux, and wind profiles as a function of wind speed and temperature, *Journal of Geophysical Research: Oceans*, *93*(C12), 15,467–15,472, 1988.

Smoluchowski, M. V., Zur Theorie der Zustandsgleichungen, *Annalen der Physik*, *353*(24), 1098–1102, doi:10.1002/andp.19163532407, 1916.

Spreen, G., L. Kaleschke, and G. Heygster, Sea ice remote sensing using AMSR-E 89 GHz channels, *Journal of Geophysical Research: Oceans*, *113*(C02S03), doi:10.1029/2005JC003384, 2008.

Squire, V. A., Ocean wave interactions with sea ice: A 2019 reappraisal, *Annu. Rev. Fluid Mech.*, *AA*, 1–25, 2019.

Stammerjohn, S., R. Massom, D. Rind, and D. Martinson, Regions of rapid sea ice change: An inter-hemispheric seasonal comparison, *Geophysical Research Letters*, *39*(6), doi:10.1029/2012GL050874, 2012.

Steele, M., and W. Ermold, Loitering of the retreating sea ice edge in the arctic seas, *Journal of Geophysical Research: Oceans*, *120*(12), 7699–7721, doi:10.1002/2015JC011182, 2015.

Steele, M., and J. H. Morison, Hydrography and vertical fluxes of heat and salt northeast of svalbard in autumn, *Journal of Geophysical Research: Oceans*, *98*(C6), 10,013–10,024, 1993.

Steele, M., J. H. Morison, and N. Untersteiner, The partition of air-ice-ocean momentum exchange as a function of ice concentration, floe size, and draft, *Journal of Geophysical Research: Oceans*, *94*(C9), 12,739–12,750, doi:10.1029/JC094iC09p12739, 1989.

Steele, M., J. Morison, W. Ermold, I. Rigor, M. Ortmeyer, and K. Shimada, Circulation of summer pacific halocline water in the arctic ocean, *Journal of Geophysical Research: Oceans*, *109*(C2), 2004.

Steele, M., W. Ermold, and J. Zhang, Modeling the formation and fate of the near-surface temperature maximum in the canadian basin of the arctic ocean, *Journal of Geophysical Research: Oceans*, *116*, doi:10.1029/2010JC006803, 2011.

Stopa, J. E., Wave climate in the arctic 1992-2014: seasonality and trends, *The Cryosphere*, *10*(4), 1605, doi:http://dx.doi.org/10.5194/tc-10-1605-2016, 2016.

Stroeve, J., T. Markus, L. Boisvert, J. Miller, and A. Barrett, Changes in arctic melt season and implications for sea ice loss, *Geophysical Research Letters*, *41*(4), 1216–1225, doi:10.1002/2013GL058951, 2014.

Stroeve, J. C., A. D. Crawford, and S. Stammerjohn, Using timing of ice retreat to predict timing of fall freeze-up in the arctic, *Geophysical Research Letters*, *43*(12), 6332–6340, doi:10.1002/2016GL069314, 2016.

Stroeve, J. C., J. R. Mioduszewski, A. Rennermalm, L. N. Boisvert, M. Tedesco, and D. Robinson, Investigating the local-scale influence of sea ice on greenland surface melt, *Cryosphere*, *11*(5), 2363–2381, 2017.

Sutherland, G., J. Rabault, K. H. Christensen, and A. Jensen, A two layer model for wave dissipation in sea ice, *Applied Ocean Research*, *88*, 111–118, 2019.

Sutherland, P., and W. K. Melville, Field measurements and scaling of ocean surface wave-breaking statistics, *Geophysical Research Letters*, *40*(12), 3074–3079, 2013.

Sutherland, P., and W. K. Melville, Field measurements of surface and near-surface turbulence in the presence of breaking waves, *Journal of Physical Oceanography*, *45*(4), 943–965, 2015.

Tanaka, H., S. Inaba, and K. Nakazawa, Steady-State Size Distribution for the Self-Similar Collision Cascade, *Icarus*, *123*, 450–455, doi:10.1006/icar.1996.0170, 1996.

Terray, E., M. Donelan, Y. Agrawal, W. Drennan, K. Kahma, A. Williams, P. Hwang, and S. Kitaigorodskii, Estimates of kinetic energy dissipation under breaking waves, *Journal of Physical Oceanography*, *26*(5), 792–807, 1996.

Thomson, J., Wave breaking dissipation observed with "SWIFT" drifters, *Journal of Atmospheric and Oceanic Technology*, *29*, 1866–1882, doi:10.1175/JTECH-D-12-00018.1, 2012.

Thomson, J., and W. E. Rogers, Swell and sea in the emerging Arctic Ocean, *Geophys. Res. Lett.*, *41*(9), 3136–3140, doi:10.1002/2014GL059983, 2014a.

Thomson, J., and W. E. Rogers, Swell and sea in the emerging arctic ocean, *Geophysical Research Letters*, *14*(9), 3136–3140, doi:10.1002/2014GL059983, 2014b.

Thomson, J., E. A. D'Asaro, M. F. Cronin, W. E. Rogers, R. R. Harcourt, and A. Y. Shcherbina, Waves and the equilibrium range at ocean weather station p, *Journal of Geophysical Research: Oceans*, *118*, 1–12, 2013a.

Thomson, J., M. Schwendeman, and S. Zippel, Wave-breaking turbulence in the ocean surface layer, *Journal of Physical Oceanography*, *46*, 1857–1870, doi:10.1175/JPO-D-15-0130.1, 2016a.

Thomson, J., S. Ackley, H. Shen, and W. Rogers, The balance of ice, waves, and winds in the arctic autumn, eos, 98, 2017.

Thomson, J., et al., Science plan: sea state and boundary layer physics of the emerging arctic ocean, in *Technical Report 1306*, Applied Physics Laboratory, University of Washington, 2013b.

Thomson, J., et al., Emerging trends in the sea state of the beaufort and chukchi seas, *Ocean Modelling*, *105*, 1–12, doi:https://doi.org/10.1016/j.ocemod.2016.02.009, 2016b.

Thomson, J., et al., Overview of the Arctic Sea State and Boundary Layer Physics Program, *Journal of Geophysical Research: Oceans*, doi:10.1002/2018JC013766, 2018.

Thomson et al., J., Onr sea state dri cruise report, 2015.

Thorpe, S., Langmuir circulation, *Ann Rev Fluid Mech*, *36*, 55–79, 2004.

Tietsche, S., M. Alonso-Balmaseda, P. Rosnay, H. Zuo, X. Tian-Kunze, and L. Kaleschke, Thin arctic sea ice in l-band observations and an ocean reanalysis, *Cryosphere*, *12*, 2051–2072, 2018.

Timmermans, M.-L., The impact of stored solar heat on arctic sea ice growth, *Geophysical Research Letters*, *42*(15), 6399–6406, doi:10.1002/2015GL064541, 2015.

Timmermans, M.-L., J. Toole, and R. Krishfield, Warming of the interior arctic ocean linked to sea ice losses at the basin margins, *Science advances*, *4*(8), eaat6773, 2018.

Toffoli, A., L. G. Bennetts, M. H. Meylan, C. Cavaliere, A. Alberello, J. Elsnab, and J. P. Monty, Sea ice floes dissipate the energy of steep ocean waves, *Geophysical Research Letters*, *42*(20), 8547–8554, 2015.

Toole, J. M., M.-L. Timmermans, D. K. Perovich, R. A. Krishfield, A. Proshutinsky, and J. Richter-Menge, Influences of the ocean surface mixed layer and thermohaline stratification on arctic sea ice in the central canada basin, *Journal of Geophysical Research: Oceans*, *115*(C10), 2010.

Toole, J. M., R. A. Krishfield, M.-L. Timmermans, and A. Proshutinsky, The ice-tethered profiler: Argo of the arctic, *Oceanography*, *24*(3), 126–135, doi:http://www.jstor.org/stable/24861307, 2011.

Treshnikov, A. F., The ice of the southern ocean, *Pacific Antarctic Sci., 11th Pacific Science Congress*, pp. 113–123, 1967.

Tsamados, M., D. L. Feltham, D. Schroeder, D. Flocco, S. L. Farrell, N. Kurtz, S. W. Laxon, and S. Bacon, Impact of variable atmospheric and oceanic form drag on simulations of arctic sea ice, *Journal of Physical Oceanography*, *44*(5), 1329–1353, 2014.

Turner, J., T. J. Bracegirdle, T. Phillips, G. J. Marshall, and J. Scott Hosking, An initial assessment of Antarctic sea ice extent in the CMIP5 models, *J. Clim.*, *26*(5), 1473–1484, doi:10.1175/JCLI-D-12-00068.1, 2013.

Turner, J. S., *Buoyancy effects in fluids*, Cambridge University Press, 1979.

Ullman, D. S., and D. Hebert, Processing of underway ctd data, *Journal of Atmospheric and Oceanic Technology*, *31*(4), 984–998, doi:https://doi.org/10.1175/JTECH-D-13-00200.1, 2014.

Umlauf, L., and H. Burchard, Second-order turbulence closure models for geophysical boundary layers: a review of recent work., *Cont. Shelf Res.*, *25*(7), 795–827, 2005.

Vancoppenolle, M., T. Fichefet, H. Goosse, S. Bouillon, G. Madec, and M. A. M. Maqueda, Simulating the mass balance and salinity of Arctic and Antarctic sea ice. 1. Model description and validation, *Ocean Model.*, *27*(1-2), 33–53, doi:10.1016/j.ocemod.2008.10.005, 2009.

Vihma, T., Effects of arctic sea ice decline on weather and climate: A review, *Surveys in Geophysics*, *35*(5), 1175–1214, 2014.

Voermans, J. J., A. V. Babanin, J. Thomson, M. M. Smith, and H. H. Shen, Wave attenuation by sea ice turbulence, *Geophysical Research Letters*, 2019.

Wadhams, P., Airborne laser profiling of swell in an open ice field, *Journal of Geophysical Research*, *80*(33), 4520–4528, 1975.

Wadhams, P., M. Lange, and S. F. Ackley, The ice thickness distribution across the Atlantic sector of the Antarctic Ocean in midwinter, *J. Geophys. Res. Ocean.*, *92*(C13), 14,535–14,552, doi:10.1029/JC092iC13p14535, 1987.

Wadhams, P., V. A. Squire, D. J. Goodman, A. M. Cowan, and S. C. Moore, The attenuation rates of ocean waves in the marginal ice zone, *Journal of Geophysical Research: Oceans*, *93*(C6), 6799–6818, 1988.

Wadhams, P., G. Aulicino, F. Parmiggiani, P. Persson, and B. Holt, Pancake ice thickness mapping in the beaufort sea from wave dispersion observed in sar imagery, *Journal of Geophysical Research: Oceans*, doi:10.1002/2017JC013003, 2018.

Wang, R., and H. H. Shen, Gravity waves propagating into an ice-covered ocean: A viscoelastic model, *Journal of Geophysical Research: Oceans*, *115*(C6), 2010.

Wang, X., J. R. Key, and Y. Liu, A thermodynamic model for estimating sea and lake ice thickness with optical satellite data, *Journal of Geophysical Research: Oceans*, *115*(C12), doi:10.1029/2009JC005857, 2010.

WaveWatch III Development Group, User manual and system documentation of wavewatch iii version 5.16, 2016.

Webster, M. A., I. G. Rigor, S. V. Nghiem, N. T. Kurtz, S. L. Farrell, D. K. Perovich, and M. Sturm, Interdecadal changes in snow depth on arctic sea ice, *Journal of Geophysical Research: Oceans*, *119*(8), 5395–5406, doi:10.1002/2014JC009985, 2014.

Weeks, W. F. S., and S. F. Ackley, The growth, structure, and properties of sea ice, in *The Geophysics of Sea Ice*, vol. 146, edited by N. Untersteiner, pp. 9–164, Springer, doi: 10.1002/9781444317145.ch2, 1986.

Wiles, P. J., T. P. Rippeth, J. H. Simpson, and P. J. Hendricks, A novel technique for measuring the rate of turbulent dissipation in the marine environment, *Geophysical Research Letters*, *33*(21), doi:10.1029/2006GL027050, 2006.

Williams, G. D., et al., Drones in a cold climate, *Eos*, *97*(doi:10.1029/2016EO043673), 2016.

Winsor, P., and G. Björk, Polynya activity in the arctic ocean from 1958 to 1997, *Journal of Geophysical Research: Oceans*, *105*(C4), 8789–8803, 2000.

Worby, A. P., Observing Antarctic Sea Ice: A practical guide for conducting sea ice observations from vessels operating in the Antarctic pack ice, A CD-ROM produced for the Antarctic Sea Ice processes and Climate (ASPeCt) program of the Scientific Committee for Antarctic Research (SCAR) Global Change (GLOCHANT) program, Hobart, Tasmania, Australia, 1999a.

Worby, A. P., Observing antarctic sea ice: A practical guide for conducting sea ice observations from vessels operating in the antarctic pack ice, A CD-ROM produced for the Antarctic Sea Ice processes and Climate (ASPeCt) program of the Scientific Committee for Antarctic Research (SCAR) Global Change (GLOCHANT) program, Hobart, Tasmania, Australia, 1999b.

Worby, A. P., C. A. Geiger, M. J. Paget, M. L. Van Woert, S. F. Ackley, and T. L. DeLiberty, Thickness distribution of antarctic sea ice, *Journal of Geophysical Research: Oceans*, *113*(C5), doi:10.1029/2007JC004254, 2008.

Wu, L., A. Rutgersson, and E. Sahlee, Upper-ocean mixing due to surface gravity waves, *J. Geophys. Res. Oceans*, *120*, 8210–8228, 2015.

Yang, J., The seasonal variability of the arctic ocean ekman transport and its role in the mixed layer heat and salt fluxes, *Journal of Climate*, *19*(20), 5366–5387, doi:10.1175/JCLI3892.1, 2006.

Yang, J., J. Comiso, D. Walsh, R. Krishfield, and S. Honjo, Storm-driven mixing and potential impact on the arctic ocean, *Journal of Geophysical Research: Oceans*, *109*(C4), doi:10.1029/2001JC001248, 2004.

Yelland, M. J., P. K. Taylor, I. E. Consterdine, and M. H. Smith, The use of the inertial dissipation technique for shipboard wind stress determination, *Journal of Atmospheric and Oceanic Technology*, *11*(4), 1093–1108, 1994.

Yiew, L., L. Bennetts, M. Meylan, B. French, and G. Thomas, Hydrodynamic responses of a thin floating disk to regular waves, *Ocean Modelling*, *97*, 52–64, 2016.

Yiew, L. J., L. Bennetts, M. Meylan, G. Thomas, and B. French, Wave-induced collisions of thin floating disks, *Physics of Fluids*, *29*(12), 127,102, 2017.

Young, I., *Wind Generated Ocean Waves*, *Ocean Engineering*, vol. 2, Elsevier, 1999.

Yu, Y., and D. Rothrock, Thin ice thickness from satellite thermal imagery, *Journal of Geophysical Research: Oceans*, *101*(C11), 25,753–25,766, doi:10.1029/96JC02242, 1996.

Zhang, J., A. Schweiger, M. Steele, and H. Stern, Sea ice floe size distribution in the marginal ice zone: Theory and numerical experiments, *J. Geophys. Res. Ocean.*, *120*(5), 3484–3498, doi:10.1002/2015JC010770, 2015.

Zhang, J., H. Stern, B. Hwang, A. Schweiger, M. Steele, M. Stark, and H. C. Graber, Modeling the seasonal evolution of the Arctic sea ice floe size distribution, *Elem Sci Anth*, *4*(1), 126, doi:10.12952/journal.elementa.000126, 2016.

Zhong, W., M. Steele, J. Zhang, and J. Zhao, Greater role of geostrophic currents in ekman

dynamics in the wester arctic ocean as a mechanism for beaufort gyre stabilization, *J. Geophys. Res. Oceans*, *123*, 2018.

Zippel, S. F., and J. Thomson, Air-sea interactions in the marginal ice zone, *Elementa Science of the Anthropocene*, *4*, doi:10.12952/journal.elementa.000095, 2016.

Zippel, S. F., J. Thomson, and G. Farquharson, Turbulence from breaking surface waves at a river mouth, *Journal of Physical Oceanography*, *48*(2), 435–453, doi:10.12952/journal.elementa.000095, 2018.